TRAPPED-ENERGY HIGH-FREQUENCY PIEZOELECTRIC RESONATORS

SUBMITTED BY

WONG HON TUNG

A THESIS SUBMITTED IN PARTIAL FULFILMENT OF THE REQUIREMENTS FOR THE DEGREE OF MASTER OF PHILOSOPHY IN APPLIED PHYSICS

AT

THE DEPARTMENT OF APPLIED PHYSICS

THE HONG KONG POLYTECHNIC UNIVERSITY

September 2006

CERTIFICATE OF ORIGINALITY

I hereby declare that this thesis is my own work and that, to the best of my knowledge and belief, it reproduces no material previously published or written, nor material that has been accepted for the award of any other degree or diploma, except where due acknowledgement has been made in the text.

________________________ (Signed)

WONG HON TUNG (Name of Student)

Abstract

The resonance responses of two types of AT-cut quartz resonators, 4-MHz and 27-MHz (provided by Hong Kong X'tals Ltd.), have been studied using the commercial finite element (FEM) code ANSYS. For the 4-MHz resonator with full electrode, there exist spurious modes (thickness-twist mode, flexural mode, and inharmonic thickness-shear mode) in the vicinity (± 0.2 MHz) of the fundamental thickness-shear mode resonance (f_{111}). After the use of an electrode of size smaller than the quartz plate, the spurious modes are not suppressed or shift to higher frequencies, and still affect significantly the vibration at f_{111}. The simulations also show that the vibration at f_{111} is not effectively trapped in the electroded region and spreads over the whole quartz plate, thus, the silver epoxy introduced at the ends of the quartz plate absorbs the vibration energy and the impedance at f_{111} is increased. The poor energy trapping efficiency should be due to the small difference between the cutoff frequencies in the electroded and unelectroded regions as well as the low frequency of the vibration. Due to the mass loading effect, a thicker electrode (e.g. 2 μm) can decrease the cutoff frequency in the electroded region (i.e. f_{111}) and hence improve the energy trapping efficiency.

Similar to the 4-MHz resonators, there exist spurious modes (the flexural mode and the inharmonic thickness-shear mode) in the vicinity of f_{111} for the 27-MHz resonator with full electrodes. However, all the spurious modes are suppressed or shift to higher frequencies after the use of an electrode of size smaller than the quartz plate. The simulations show that the vibration at f_{111} is pure thickness-shear mode and it is effectively trapped in the electroded region. As a result, f_{111} is dependent relatively stronger on the electrode length, and the impedance at f_{111} does not increase significantly after the introduction of the silver epoxy. The better energy trapping efficiency should be due to the high frequency of the vibration.

A new experimental method has been developed to investigate the vibration distribution of the resonators. It is based on the fact that an external load can disturb the vibration and hence change the resonance frequency as well as the impedance at resonance of a quartz plate. Good agreements between the observed and simulated vibration distributions at f_{111} are obtained for both the 4-MHz and 27-MHz resonators. The dependence of f_{111} on the electrode length has also been confirmed by experiments on the "commercial" resonators with different electrode lengths. Again, good agreements between the experimental and simulation results are obtained for both the 4-MHz and 27-MHz resonators.

A third-overtone thickness-shear resonator with resonance frequency around 58 MHz has been designed and successfully fabricated. In the new design, two sub-electrodes are added right next to each end of the main electrode of the resonator to amplify the “leaked” vibration at f_{111} from the main electrode and subsequently damped by the silver epoxy at the ends of the resonator. On the other hand, the vibration at the third-overtone thickness-shear resonance f_{311} is mainly trapped in the main-electroded region and hence is not affected significantly by the sub-electrode and the silver epoxy. As a result, the impedance at f_{111} becomes much larger than that at f_{311} and the resonator will resonate at its third-overtone thickness-shear mode.

Acknowledgments

I would like to express my appreciation to my supervisors Dr. K. W. Kwok and Prof. H. L. W. Chan for their excellent guidance and constant encouragement throughout the whole period of my research work. I would also like to thank Mr. W. O. Chu from Hong Kong X'tals Ltd. for his helpful discussions about the resonance responses of the quartz resonators and technical supports.

I would also like to thank Mr. C. H. Ho, Mr. S. W. Cheung, Mr. S. K. K. Curreem, Miss W. Y. Chung, Mr. W. F. Wong, Mr. Z. Lang, Miss X. Y. Zhou and Mr. Y. Zhou, for their friendship and valuable discussions.

I gratefully acknowledge the financial support from the Innovation and Technology Fund of the HKSAR Government and Hong Kong X'tals Ltd., and technical support provided by the Centre for Smart Materials of the Hong Kong Polytechnic University.

The last but not least, I would like to thank my parents for their understanding, constant support and encouragement.

Table of Contents

List of Figures

List of Tables

Chapter One
Introduction

1.1 Background

The direct piezoelectric effect, the production of electricity by the application of pressure, was discovered by the brothers Pierre Curie and Jacques Curie in 1880. The converse piezoelectric effect was predicted by Lippmann in 1888 and confirmed by the Curies in the same year. The first major application of piezoelectricity was in Langevin's work on submarine detection using quartz transducers to generate and detect underwater acoustic waves, started in 1917. Since then, the quartz crystal units have been an item of commerce for more than a half century. The applications for the quartz crystals have grown from their early roots in frequency standards and in amateur radio communication to present wide spectrum of applications encompassing many electronic products. The milestones in quartz technology are shown in Table 1.1 [*Vig, 2003*].

Table 1.1 Milestones in quartz technology [*Vig, 2003*].

1880	Piezoelectric effect discovered by Jacques and Pierre Curie
1905	First hydrothermal growth of quartz in a laboratory - by G. Spezia
1917	First application of piezoelectric effect, in sonar
1918	First use of piezoelectric crystal in an oscillator
1926	First quartz crystal controlled broadcast station
1927	First temperature compensated quartz cut discovered
1927	First quartz crystal clock built
1934	First practical temp. compensated cut, the AT-cut, developed
1949	Contoured, high-Q, high stability AT-cuts developed
1956	First commercially grown cultured quartz available
1956	First TCXO described
1972	Miniature quartz tuning fork developed; quartz watches available
1974	The SC-cut (and TS/TTC-cut) predicted; verified in 1976
1982	First MCXO with dual c-mode self-temperature sensing

As an electronic device, it is required that the signal given by the quartz crystal units is stable over a wide range of parameters such as temperature. In the quartz crystals, however, there are many vibration modes, i.e. signals. For instance, the quartz crystal units can vibrate in thickness-shear modes and flexural mode. Because different vibration modes have different frequency-temperature relationships, the quartz crystals may vibrate from the wanted vibration mode, i.e. fundamental thickness-shear mode, to other unwanted vibration modes at different temperatures. In other words, the signal is unstable over a wide range of temperature.

To deal with this problem, many attempts have been made in the past to suppress the unwanted modes, especially those modes which are near in frequency to the fundamental thickness-shear mode and tend undesirably to couple with it. It was found in 1940 by Bechmann that the unwanted modes could be suppressed by placing a pair of small electrodes on a quartz plate [*Bechmann, 1941*]. Later, Mortley explained this phenomenon by considering the cutoff mode of a waveguide. [*Mortley, 1956*] Shockley et al. called this phenomenon energy trapping and performed a theoretical analysis of this phenomenon independently. [*Shockley, 1963*] The conditions for the suppression of the unwanted modes have been given in this energy trapping theory. Some researchers such as Hirama [*Hirama, 1999*] also use the same approach as Shockley in their design of the trapped-energy resonators. However, those researchers have not investigated the energy trapping systematically and no efficient procedure for applying the energy trapping has been given.

Finite element method (FEM) is used to investigate the energy trapping phenomenon systematically in this project. The finite element method is a powerful computational technique for approximate solutions to a variety of real world engineering problems having complex structures. ANSYS, a commercial general purpose finite element software, is capable of performing the piezoelectric analysis and it is used to conduct the research. By studying the energy trapping systematically, an efficient procedure for the suppression of the unwanted modes can be given, which can replace the experimental procedure and make the production more effective and eventually lead to saving in cost and time.

1.2 Quartz

Quartz is a crystalline form of silicon dioxide, SiO_2. It is a hard, brittle, transparent material with a density of 2649 kg/m^3 and a melting point of 1750 ^oC. When quartz is heated to 573 ^oC, its crystalline form changes. The stable form above this transition or inversion temperature is known as 'high-quartz' or 'beta-quartz', in which the quartz exists in a hexagonal symmetry. The stable form below 573 ^oC is known as 'low-quartz' or 'alpha-quartz', in which the quartz exists in a trigonal symmetry. For resonator applications, only alpha-quartz is of interest and unless stated otherwise the term 'quartz' always refers to alpha-quartz [*Salt, 1987*].

1.2.1 Piezoelectricity

Quartz is a piezoelectric material which exhibits direct and converse piezoelectric effects. The direct piezoelectric effect discovered by the Curie brothers in 1880 is the production of the electric polarization by the application of a mechanical stress into a crystal. The magnitude of the induced charge is proportional to the applied stress. In 1881, the converse piezoelectric effect, predicted by Lippman and confirmed by the Curies, was illustrated. It is the deformation produced in the crystal by the application of the electric field. The deformation in the crystal is due to the lattice strains caused by the effect. The strain reversed when the direction of the electric field reversed. The piezoelectric effect, therefore, provides a coupling between the electrical and the mechanical properties of the crystal. For quartz resonators, the converse piezoelectric effect is used for the resonators to resonate at certain frequencies.

The converse piezoelectric effect has sometimes been confused with the electrostrictive effect, which is the deformation produced when placed in the electric field. The electrostrictive effect occurs in all dielectrics such as glass and the piezoelectric effect can be differentiated from the electrostrictive effect in two aspects. The piezoelectric strain is usually larger than the electrostrictive strain by several orders of magnitude, and the piezoelectric strain is proportional to the electric-field intensity and thus change sign with it, while the electrostrictive strain is proportional to the square of the field intensity and thus independent of its direction. The electrostrictive effect and the piezoelectric effect occur at the same time, and the electrostrictive effect may be ignored in the quartz for practical purposes.

The reversible nature of the piezoelectric effect implies that the piezoelectric crystals must be anisotropic, that is their physicals properties must depend on direction within the crystals. Therefore, the piezoelectric crystals lack a centre of symmetry. When the lattice is deformed by an applied force, the centres of gravity of the positive and negative charges in the crystal will be separated so as to produce surface charges. Figure 1.1 shows one example (from Kelvin's qualitative model) of the effect in the quartz. Each silicon atom is represented by a plus, and each oxygen atom by a minus. When a strain is applied along the Y-axis, the crystal will be elongated in this direction and there are net movements of negative charges to the left and positive charges to the right (along the X-axis), thus electric polarization is produced [*Heising, 1946*].

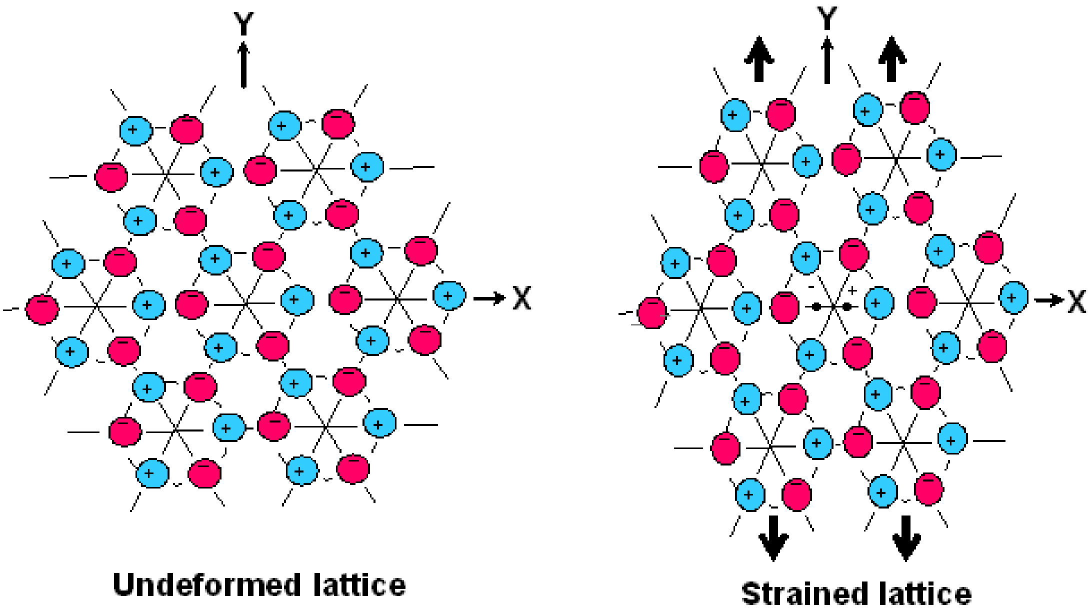

Figure 1.1 The production of the electric polarization by the application of mechanical strain [*Heising, 1946*].

1.2.2 Left and Right Quartz

The idealized quartz crystal is a hexagonal prism with six cap faces at each end as shown in Figure 1.2. The prism faces are designated as m-face and the cap faces are designated as R- and r- faces. The R-faces are called major rhomb faces, while the r-faces, minor rhomb faces. There are two naturally occurring forms in the quartz crystals, known as right quartz and left quartz. They can be differentiated by the position of s and x faces relative to the m-, R-, and r- faces. In the right quartz, the s and x faces occur at the lower right corner of the R-faces, whereas in the left quartz, they occur at the lower left corner of the R-faces. Although there are two forms of the quartz crystals, both kinds of quartz are equally useful in fabricating quartz crystal resonators [*Bottom, 1982*].

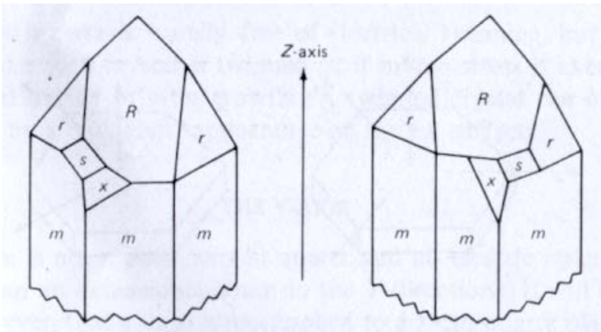

Left quartz Right quartz

Figure 1.2 The quartz crystal. In the right quartz, the s and x faces occur at the lower right corner of the R face. In the left quartz, they occur at the lower left corner [*Bottom, 1982*].

1.2.3 Crystal Axes and Axial Systems

Quartz is an anisotropic material, i.e. the values of the coefficients describing the physical properties are dependent on direction. It is therefore necessary to choose the reference directions within the quartz to specify the values of the coefficients. These directions are called the crystal axes. Different axial systems can be employed to describe the same quartz since it may be convenient for one purpose for one coordinate system, and another purpose for another system. Thus, it should be mentioned which coordinate system is employed. At least, two coordinate systems may be used to specify the quartz. They are the Bravais-Miller (B-M) coordinate system and the rectangular coordinate system, which are shown in Figure 1.3. The B-M system is used to specify the natural faces and atomic planes in the quartz, while the rectangular system is used for the purpose of computations involving the piezoelectric and mechanical properties of the quartz.

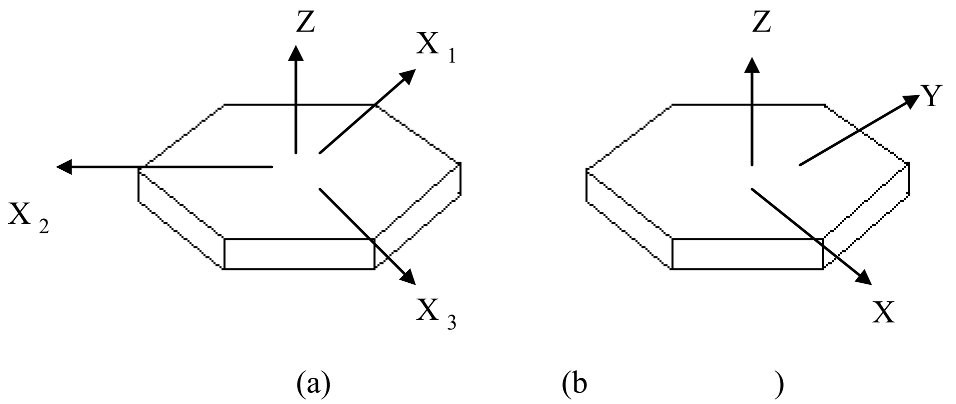

Figure 1.3 Cross-section of the quartz crystal taken perpendicular to the Z-axis, showing (a) the B-M system and (b) the rectangular system [*Bottom, 1982*].

The B-M system consists of a Z-axis (also called c-axis) and three identical X-axes (also called a_1, a_2, and a_3 axes) which make angles of 120^o with each other and lie in a plane perpendicular to the Z-axis. The B-M system is applicable to crystals which have trigonal symmetry such as quartz.

The rectangular system includes three mutually perpendicular axes: x, y, and z axes. The Z-axis in the rectangular system is the same as that in the B-M system, the X-axis in the rectangular system is one of the three X-axes in the B-M system, and the Y-axis is perpendicular to both the Z- and X- axes. The rectangular system is applicable to crystals which have cubic symmetry such as sodium chloride.

The Z-axis in the quartz is an axis of threefold symmetry, i.e. all physical properties repeat as the quartz is rotated about the Z-axis each 120^o. When a beam of plane-polarized light is transmitted along the Z-axis, the plane of polarization is rotated. The sense of the rotation provides another means to distinguish between the left and right quartz. In the right quartz, the plane of polarization is rotated clockwise as seen by an observer looking towards the source of light. In the left quartz, the plane of polarization is rotated anti-clockwise [*Frondel, 1962*].

The X-axes in the quartz are parallel to a line bisecting the angles between the adjacent prism faces. The X-axis is a polar axis since electric polarization **P** occurs in this direction. The positive X-direction is chosen to be the direction in which a positive charge is produced by a positive strain, which is defined to be the extension resulting from a tension. By this definition, that end of the X-axis is positive where a negative charge is developed by a compression.

The Y-axis of the rectangular system is neither an axis of threefold symmetry nor a polar axis in the quartz. It is just an axis which is perpendicular to the X- and Z- axis.

As there are left and right quartz in nature, it is necessary to consider the hand of the quartz in setting up the coordinate system. The values of the coefficients of all the physical properties and the mathematical relationships between the left and right quartzes become identical if a right-hand coordinate system is used for the right quartz and a left-hand coordinate system is used for the left quartz. As a result, the following conventions have been recommended for the quartz.

1. The right-hand coordinate system is used to describe the physical properties of the right quartz and the left-hand coordinate system for the left quartz.
2. In the right-hand coordinate system, a positive rotation is one which appears anticlockwise when observed from the positive end of the axis of rotation.

1.2.4 Cut of Quartz

In real applications, the quartz crystal is first cut into a number of small pieces of quartz plates. There are many different kinds of crystal cut, e.g. X-cut, Y-cut, and AT-cut. For the X-cut, the normal to the quartz plate is parallel to the X-axis. For the Y-cut, the normal to the quartz plate is parallel to the Y-axis. For the AT-cut, it belongs to the Y-cut family. It is formed by rotating the Y-cut quartz plate with an angle of 35.25^{o} about the X-axis in clockwise direction. And a new rectangular coordinate system is defined for the AT-cut quartz plate as X_1, X_2, and X_3 as shown in Figure 1.4.

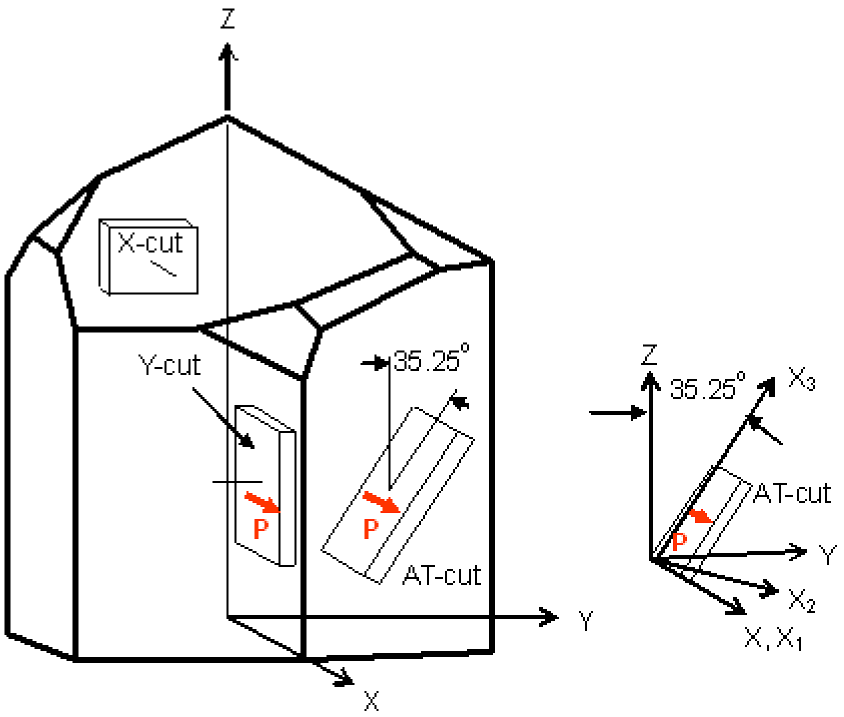

Figure 1.4 The rectangular system in the quartz crystal and various crystal cuts.

The first quartz resonators used the X-cut quartz plate. The disadvantage of the X-cut quartz plate is that the resonance frequency decreases 20 Hz/MHz for each degree rise in temperature. The Y-cut quartz plate has certain advantages over the X-cut quartz plate. The thickness of the Y-cut quartz plate is only about two-third that of the X-cut quartz plate of the same frequency. It also has fewer unwanted modes of vibration and is less affected by air damping. The most important advantage is that it can be clamped for mounting. However, there is a disadvantage for the Y-cut quartz plate. The resonance frequency of the Y-cut increases 100 Hz/MHz for each degree rise in temperature [*Ballato, 1977*].

It is found that the resonance frequency of the AT-cut quartz plate remains constant at certain temperatures. Because of the frequency-temperature stability over a reasonably wide temperature range, the AT-cut quartz plate is now the most commonly used type of crystal cut. The AT-cut quartz resonators excite in the thickness-shear mode of vibration and are commonly manufactured in the frequency range from about 1 MHz to 200 MHz and above.

1.2.5 Key Properties of Quartz Resonators

A piezoelectric resonator is a piece of piezoelectric material precisely dimensioned and oriented with respect to the crystallographic axes of the material and equipped with one or more pairs of conducting electrodes. Many different substances have been investigated as possible candidates for piezoelectric resonators, but for many years, quartz resonators have been preferred in satisfying needs for precise frequency control and selection. Compared to other resonators, for example piezoelectric resonators based on ceramics or other single crystals, the quartz resonator has a unique combination of properties. The material properties of the quartz are extremely stable and highly repeatable from one specimen to another. The acoustic loss or internal friction of the quartz is particularly low, leading directly to one of the key properties of the quartz resonators, its extremely high Q factor. The intrinsic Q of the quartz is 10^7 at 1 MHz. The Q factors of mounted resonators typically range from tens of thousands to several hundreds of thousands, orders of magnitude better than the best LC circuits.

The second key property of the quartz resonators is its stability with respect to temperature variation. With different shapes and orientations of the crystal blanks, many different modes of vibrations can be used and it is possible to control the frequency-temperature characteristics of the resonator to within close limits by an appropriate choice. The most commonly used type of the quartz resonator is the AT-cut which has a frequency-temperature stability over a reasonably wide temperature range required by modern communication systems [*Salt, 1987*].

The unique ability for the quartz resonators to control the resonance frequency is its high Q factor and low electromechanical coupling coefficient κ.

The Q of any resonance systems is defined as [*ANSI/IEEE Std 100-1984, 1984*]

$$Q = 2\pi \frac{Energy \quad stored \quad per \quad cycle}{Energy \quad dissipated \quad per \quad cycle} \tag{1.1}$$

The value of the electromechanical coupling coefficient, κ, is defined as

$$\kappa = \sqrt{\frac{Energy \quad stored \quad elastically}{Energy \quad stored \quad electrically}} \tag{1.2}$$

The value of κ^2 for the AT-cut quartz is less than 1 percent. This means that the electric driving system is very loosely coupled to the mechanical system and thus the former has very little influence over the latter. But, because of the high Q, even such a small effect is sufficient to excite and maintain vibrations in the quartz resonator, which is what makes it an effective transducer for controlling a frequency.

1.2.6 Applications of Quartz Crystal Units

The unique ability for the quartz crystals to maintain a stable resonance frequency makes it a natural choice as the isochronous element in time-keeping devices. The development of suitable electronic components to use with the vibrating quartz now makes quartz clocks and watches practical and it appears that the torsional pendulum which has been the basis of the watch industry for over three centuries has now been superseded by the quartz piezoid.

The temperature-frequency dependence of a specially designed quartz piezoid is used in a thermometer of great convenience and accuracy. The quartz thermometer is capable of providing almost instantaneous digital temperature information from remote locations [*Bottom, 1982*].

The applications of the quartz crystals in many different areas are shown in Table 1.2 [*Vig, 1993, 2003*].

Table 1.2 The applications of the quartz crystal [*Vig, 1993, 2003*].

Military & Aerospace	**Industrial**	**Consumer**
Communications	Communications	Watches & clocks
Navigation	Telecommunications	Cellular & cordless phones, pagers
IFF	Mobile/cellular/portable radio, telephone & pager	Radio & hi-fi equipment
Radar	Aviation	Color TV
Sensors	Marine	Cable TV systems
Guidance systems	Navigation	Home computers
Fuzes	Instrumentation	VCR & video camera
Electronic warfare	Computers	CB & amateur radio
Sonobouys	Digital systems	Toys & games
Research & Metrology	CRT displays	Pacemakers
Atomic clocks	Disk drives	Other medical devices
Instruments	Modems	**Automotive**
Astronomy & geodesy	Tagging/identification	Engine control, stereo, clock
Space tracking	Utilities	Trip computer, GPS
Celestial navigation	Sensors	

1.3 Energy Trapping

Quartz resonators are capable of many vibration modes, such as thickness-shear modes and flexural modes. In general, only one of the vibration modes is desired, it is the fundamental thickness-shear mode. Others are unwanted modes called spurious modes. To suppress the spurious modes, especially those modes which are near in frequency to the fundamental thickness-shear and have the undesired tendency to couple with it, energy trapping is used.

The concept of the energy trapping was first introduced by Mortley in 1946 in his paper "A waveguide theory of piezoelectric resonance" [*Mortley, 1946*]. Shockley et al. called this phenomenon energy trapping and performed a theoretical analysis of this phenomenon independently [*Shockley, 1963, 1967*]. The theory of the energy trapping by these authors was devised to explain Guttwein's observation that excessive electrode thickness introduced spurious modes [*Guttwein, 1963*].

The physical picture of the energy trapping is as follows. The general quartz resonator is shown in Figure 1.5.

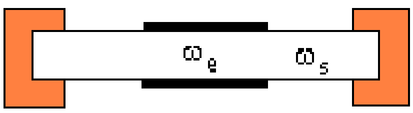

Figure 1.5 The general quartz resonator.

It consists of a piece of quartz plate with lossy conductive epoxy added at the ends of the quartz plate. Electrodes of finite thickness are applied on the quartz plate, and there exist two separate cutoff frequencies ω_e and ω_s for the electroded and unelectroded regions, respectively. Below ω_e and ω_s, no acoustic wave can propagate in these two regions and standing wave resonances cannot occur. Owing to the mass loading of the electrodes, ω_e is lower than ω_s. For the AT-cut quartz, the cutoff frequencies ω_e and ω_s are the frequencies of the fundamental thickness-shear modes in the regions concerned. The higher inharmonic thickness-shear modes below the electrodes will occur at frequencies higher than ω_e. The inharmonic thickness-shear modes with frequencies between ω_e and ω_s can propagate freely only in the electroded region but not in the unelectroded region. In the unelectroded region, the vibration energy tails off exponentially with distance away from the electrodes. This exponential decay is not associated with energy loss but acts to trap the vibration energy under the electrodes only. This effect is similar to the exponential attenuation of microwaves in waveguides beyond cutoff or that of electromagnetic waves undergoing total internal reflection passing from a medium of higher refractive index to a lower. For frequencies higher than ω_s, the wave can propagate freely in both the electroded and unelectroded regions. Thus, the vibration energy generated in the electroded region will propagate away and will be absorbed by the lossy conductive epoxy at the ends of the quartz plate. Therefore, only the vibration energy stored in the vibration modes with frequencies between ω_e and ω_s will get trapped. So to achieve the goal of suppressing the spurious modes, it is desired that the energy trapping only occur for the fundamental thickness-shear mode, while the vibration energy of the spurious modes will propagate freely to the unelectroded region and is absorbed by the lossy conductive epoxy at the ends of the quartz plate [*Bahadur, 1982*].

The mathematical treatment of the energy trapping theory by Shockley et al. is given below [*Shockley, 1963, 1967*]. In this theory, an isotropic body is considered. An idealized two-dimensional quartz plate with thickness b in the X_2 direction and of infinite extent in the lateral X_3 direction vibrating in a thickness-twist mode, as shown in Figure 1.6. The dimension of the quartz plate is assumed to be infinite in the X_1 direction, which is perpendicular to the X_2 and X_3 directions.

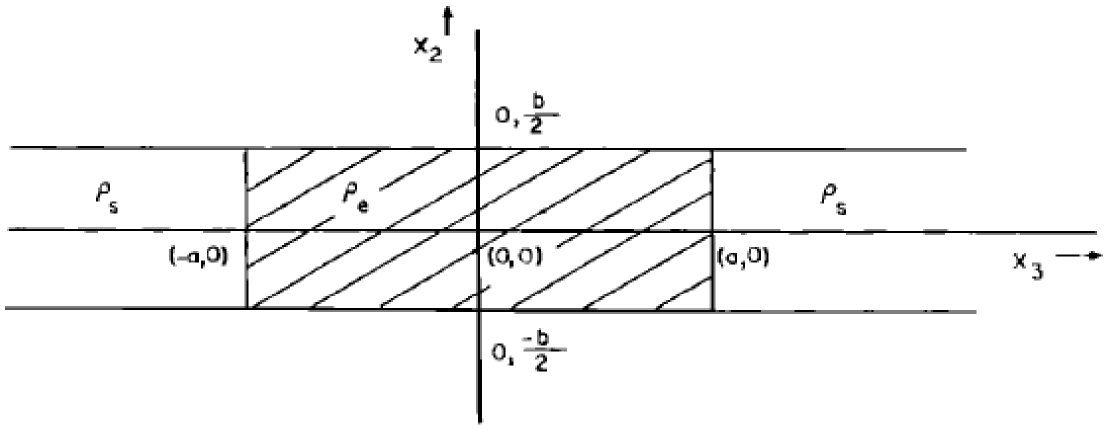

Figure 1.6 Plate with trapped-energy structure [*Shockley, 1967*].

For the quartz plate with two regions of different sound velocities, the densities are assumed to be ρ_e and ρ_s for the electroded ($-a < X_3 < a$) and unelectroded ($X_3 < -a$ and $X_3 > a$) regions, respectively. With $\rho_s < \rho_e$, the sound velocities in the electroded and unelectroded regions are

$$v_e = (\mu/\rho_e)^{1/2} \text{ and } v_s = (\mu/\rho_s)^{1/2} \tag{1.3}$$

where μ is the elastic constant. In this theory, the piezoelectric effect is neglected and only the trapping of mechanical energy is considered.

Solutions of the wave equation for particle displacement u in the X_1 direction for thickness-twist modes propagating in the X_3 directions are of the form as follows, since the displacement is assumed to be uniform in the X_1 direction.

$$u = U \sin \eta X_2 \, e^{i(\zeta X_3 - \omega t)} \tag{1.4}$$

where U is the amplitude, η is the wave vector for wave propagation along the thickness X_2 direction, ζ is the wave vector for wave propagation along the X_3 direction, ω is the angular frequency, and t is the time.

To satisfy the zero-stress boundary condition at the major faces ($\partial u/\partial X_2 = 0$ at $X_2 = \pm b/2$), the displacement u can have nonvanishing solutions only for

$$\eta = p\pi/b \tag{1.5}$$

where p = 1, 3, 5, … is the order of the harmonic overtone, e.g., fundamental, 3rd harmonic, 5th harmonic, etc.

In the unelectroded region, u must satisfy the wave equation

$$\nabla^2 u = (1/v_s)^2\, \partial^2 u/\partial t^2 \qquad (1.6)$$

Substitution of eq. (1.4) into the wave equation gives the expression relating the propagation constants

$$\eta^2 + \zeta^2 = (\omega/v_s)^2 \qquad (1.7)$$

and with eq. (1.5), the dispersion equation is

$$\zeta = [(\omega/v_s)^2 - (p\pi/b)^2]^{1/2} \qquad (1.8)$$

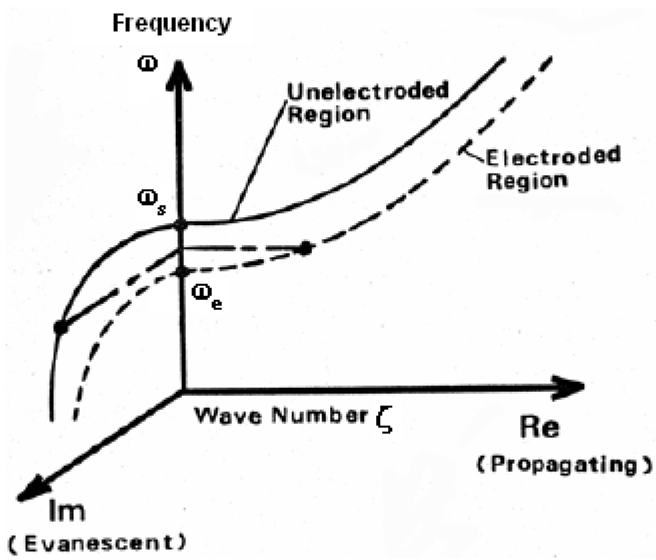

Figure 1.7 Dispersion curve of the thickness-twist mode of propagation [*Onoe, 2005*].

The dispersion curve of the thickness-twist mode of propagation is shown in Figure 1.7. Stress waves can propagate freely for all real values of ζ, i.e. $(p\pi/b) < (\omega/v_s)$, but reduce to nonpropagating vibrations which decay exponentially with distance for imaginary values of ζ, i.e. $(p\pi/b) > (\omega/v_s)$. When $(p\pi/b) > (\omega/v_s)$, then the frequency ω is less than

$$\omega_s = \pi p v_s/b \qquad (1.9)$$

The angular frequency $\omega_s = \pi p v_s/b$, below which ζ becomes imaginary and thus wave can not propagate freely, is called the cutoff frequency, and is the thickness-shear resonance frequency for plane waves in the X_2 direction. When $\omega < \omega_s$, ζ is imaginary and is rewritten as $i\gamma$.

The electroded cutoff frequency ω_e is lower than the unelectroded cutoff frequency ω_s because of the mass loading of the electrode. The cutoff frequencies for the fundamental mode propagation in the electroded and unelectroded regions respectively are given by $\omega_e = \pi v_e/b$ and $\omega_s = \pi v_s/b$. The cutoff frequencies for the p^{th} harmonic mode are given in turn by $p\omega_e$ and $p\omega_s$. For $\omega_e < \omega < \omega_s$, the waves can propagate freely in the electroded region but decay exponentially in the unelectroded region, and at certain frequencies, standing waves are formed, i.e. resonances occur. These resonance frequencies can be determined by the application of the boundary conditions at the edges of the electrode $X_3 = \pm a$ which will be discussed below.

The trapped energy vibration for the structure of Figure 1.6 can be formed as shown in Figure 1.8 by combining the standing wave in the electroded region with the attenuated wave in the unelectroded region.

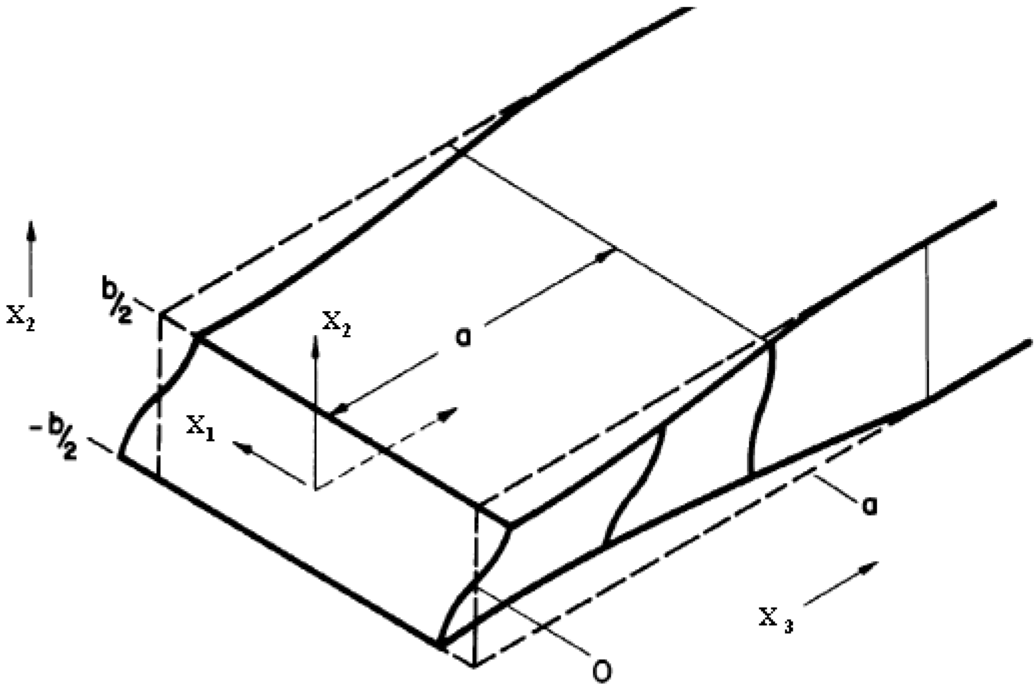

Figure 1.8 Thickness twist mode for stored energy vibration [*Shockley, 1963*].

Substitution of eq. (1.5) into eq. (1.4) and with the ζ replaced by $i\gamma$ in the unelectroded region, the solutions of the wave equation in the electroded and unelectroded regions are

$$u = E\cos(-\omega t)\sin(p\pi X_2/b)\cos(\zeta X_3) \quad \text{for } -a < X_3 < a \qquad (1.10)$$

$$u = S\cos(-\omega t)\sin(p\pi X_2/b)\, e^{-\gamma X_3} \quad \text{for } X_3 < -a \text{ and } X_3 > a \qquad (1.11)$$

where E and S are the amplitudes in the electroded and unelectroded regions, respectively.

The boundary conditions at $X_3 = \pm a$ are continuity of displacement

$$E \cos(\zeta a) = S e^{-\gamma a} \tag{1.12}$$

and continuity of shear stress $\partial u/\partial X_3$ across $X_3 = \pm a$

$$-E\zeta \sin(\zeta a) = -S\gamma e^{-\gamma a} \tag{1.13}$$

As a result, nonvanishing standing wave solutions (at resonance) can occur only at specific frequencies between ω_e and ω_s which satisfy the following equation.

$$\tan \zeta_e a = \gamma_s/\zeta_e \tag{1.14}$$

where

$$\zeta_e = (\pi/b) [(\omega/\omega_e)^2 - p^2]^{1/2} \tag{1.15}$$

$$\gamma_s = -i\zeta_s = (\pi/b) [p^2 - (\omega/\omega_s)^2]^{1/2} \tag{1.16}$$

Then by straightforward manipulations, a useful expression relating the resonance frequencies ω_{te} with the resonator parameters a/b and $\Omega_o = \omega_e/\omega_s$ can be obtained. And the mode series for each harmonic (p = 1, 3, 5, etc.) can be presented graphically with the vertical axis as

$$\psi = (\Omega_{te} - p\Omega_o)/p(1 - \Omega_o) \qquad (1.17)$$

where normalized eigenfrequencies $\Omega_{te} = \omega_{te}/\omega_s$ and the horizontal axis as

$$p\,(a/b)\,[(1 - \Omega_o)/\Omega_o]^{1/2} \qquad (1.18)$$

which is the resonator parameter. In this way, the mode series for each harmonic coincides and the complete solution can be presented graphically in the simple fashion as shown in Figure 1.9.

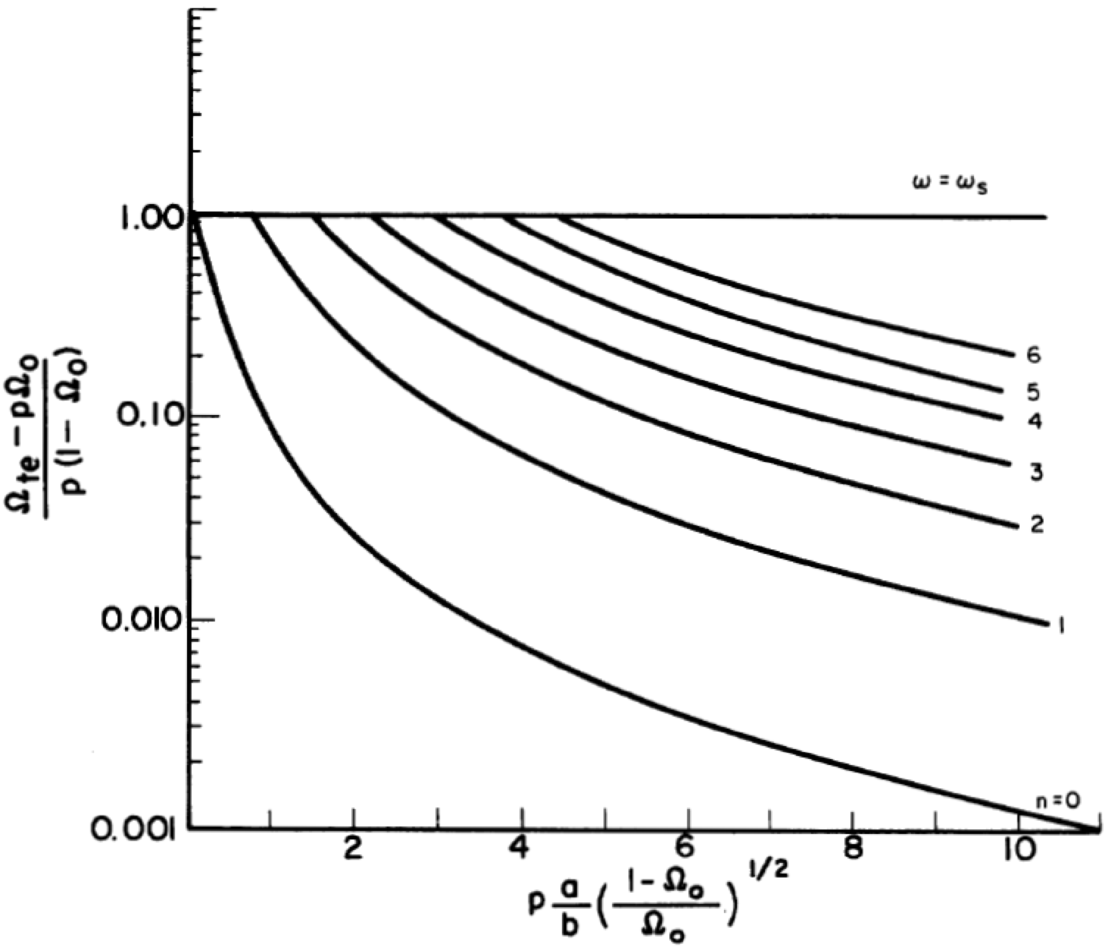

Figure 1.9 Normalized eigenfrequencies Ω_{te} for harmonic (p) and inharmonic (n) series as a function of resonator parameters [*Shockley, 1967*].

In Figure 1.9, the values n = 0, 1, 2, etc. give the inharmonic mode series for each value of p. Figure 1.9 can be used to find the criteria for the suppression of a portion or all of each inharmonic overtones series. To suppress the inharmonic modes, the corresponding resonance frequency ω_{te} should be higher than ω_s so that the vibration energy of the inharmonic modes can propagate freely to the unelectroded region and absorbed by the lossy conductive epoxy at the ends of the resonator. Therefore, for the suppression of the inharmonic series of n = 1, the resonator parameter p (a/b) $[(1 - \Omega_o)/\Omega_o]^{1/2}$ should be set below 1 for the resonance frequency ω_{te} higher than ω_s. Some researchers such as Nakamura et al. [*Nakamura, 1990*] and Iwata et al. [*Iwata, 2001*] also used the same technique to suppress the inharmonic modes in the design of the trapped energy resonators.

The effect found by Curran and Koneval in 1965 [*Curran, 1965*] agrees with Figure 1.9. They found that with the reduction of the electrode length a, the whole inharmonic overtone series moves up in frequency toward the cutoff frequency of the unelectroded region ω_s. Also, as the frequency of each inharmonic overtone approaches ω_s, it decreases in amplitude and finally vanishes. The progressive decrease in amplitude is due to greater leakage of the waves in the unelectroded region as ω_s is approached, which implies that there is a degree of trapping the vibration energy under the electrode. The degree of trapping the vibration energy is considered below for the fundamental mode.

In the above cases, the quartz plates are of infinite extent in the X_3 direction. However, in reality, all quartz plates are finite. Therefore, a finite quartz plate is considered here. For the fundamental resonance frequencies $\omega_{te\,1}$ and $\omega_{te\,2}$ which satisfy $\omega_e < \omega_{te\,1} < \omega_{te\,2} < \omega_s$, the standing waves are set up under the electrode with the exponentially decaying waves in the unelectroded region. The vibration displacement profiles are shown in Figure 1.10.

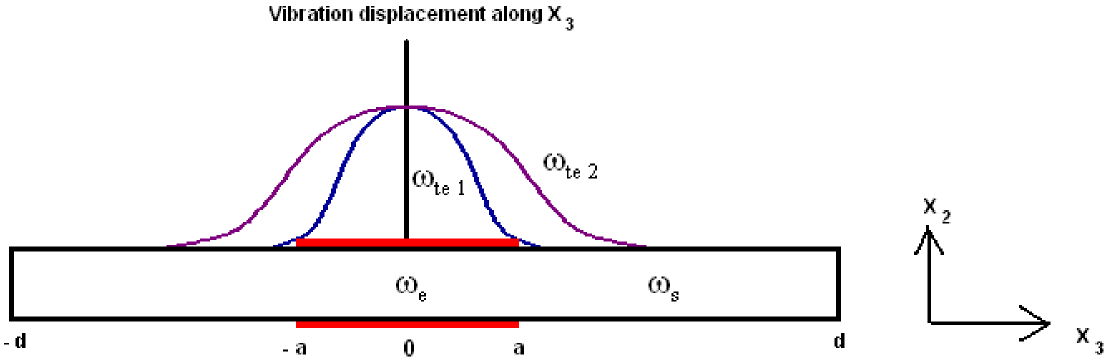

Figure 1.10 The vibration displacements along X_3 of the two trapped energy modes.

The resonance mode of $\omega_{te\,1}$ is trapped more effectively under the electrode. To describe the ability of trapping the vibration energy under the electrode, energy trapping efficiency is introduced.

From the solution of the wave equation in the electroded region, eq. (1.10), the term relating to the X_3 direction $\cos(\zeta X_3)$ has the form shown in Figure 1.11 (a). When ζX_3 is $\pi/2$, $\cos(\zeta X_3)$, i.e. the relative displacement, is 0, which means that the vibration energy is completely trapped under the electrode. The energy trapping efficiency τ is defined as follows [*Hirama, 2000*]

$$\tau = \zeta a / (\pi/2) \qquad (1.19)$$

where ζa is the phase shift at the electroded region in the fundamental mode. $\pi/2$ is the phase shift when the vibration energy is completely trapped under the electrode.

With the definition of the energy trapping efficiency τ, the degree of trapping the vibration energy can be quantified. For a normalized resonance frequency $\psi = (\Omega_{te} - \Omega_o)/(1 - \Omega_o)$, the corresponding energy trapping efficiency τ can be identified from Figure 1.11 (b) for both the finite and infinite plate.

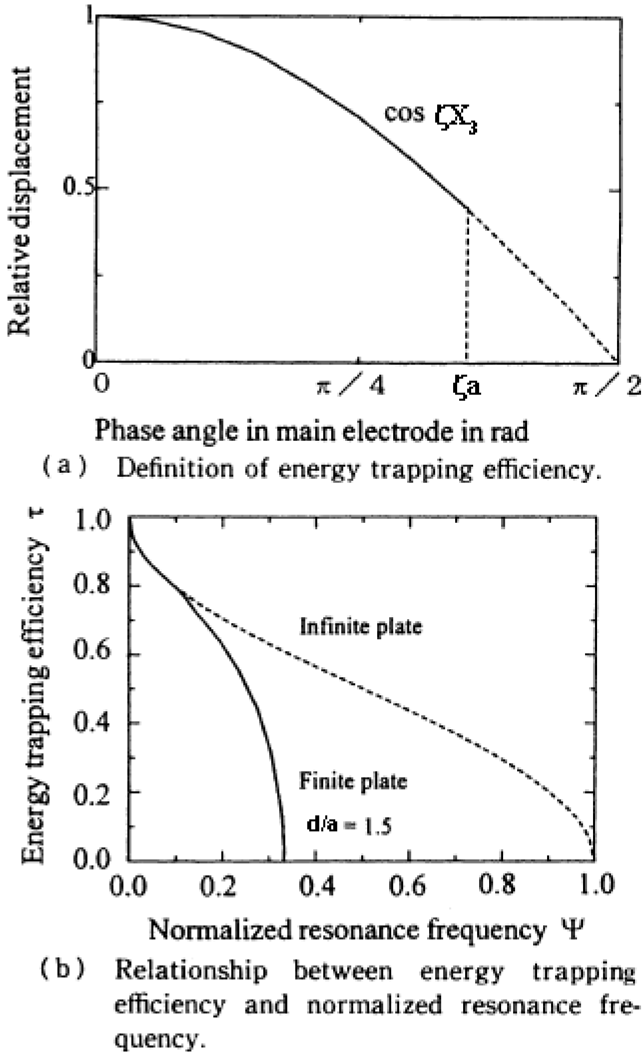

Figure 1.11 (a) Definition of the energy trapping efficiency. (b) Relationship between the energy trapping efficiency and the normalized resonance frequency. [*Hirama, 2000*]

The energy trapping efficiency τ is a very important parameter in designing the third overtone resonators, i.e. resonates at the third harmonic mode with the suppression of the fundamental mode. The design of the third overtone resonators will be discussed later.

In the theory of the energy trapping by Shockley et al., isotropic elasticity is assumed, piezoelectric effects is neglected, the thickness-twist mode of vibration is considered and infinite dimension in the X_3 direction is assumed.

To consider finite plates, an additional boundary condition at the edges of the plates ($X_3 = \pm$ d) should be considered. As shown in Figure 1.10, the stress $\partial u/\partial X_3$ at $X_3 = \pm$ d is set to zero. Then, an equation resembles that of eq. (1.14) can be obtained and the resonance frequencies trapped under the electrode of the finite plate can be determined [*Onoe, 1965*].

The AT-cut quart crystal is anisotropic and piezoelectric, also the principal vibration mode is the fundamental thickness-shear mode. Modifications to include these important refinements have been done by Mindlin and Gazis [*Mindlin, 1962*]. Following procedures similar to those by Shockley, i.e. substituting the displacement equation into the appropriate wave equations, the dispersion equations for the thickness-twist mode and the thickness-shear mode can be obtained [*Hirama, 1999*]. It is found that the cutoff frequencies of the thickness-twist mode and the thickness-shear mode are the same, below which wave propagation cannot occur.

1.4 ANSYS

1.4.1 Finite Element Method (FEM)

ANSYS Multiphysics (commonly known as ANSYS) is a general-purpose finite element analysis (FEA) software package for numerically solving a wide variety of engineering problems. The FEM is a computer-based procedure that is used to analyse structures and continua. It is a versatile numerical method that is widely applied to solve problems covering almost the whole spectrum of engineering analysis. Applications include static, dynamic, thermal, electromagnetic, and piezoelectric, etc. Advances in computer hardware have made it easier and very efficient to use the FEA software for the solutions of complex engineering problems on personal computers [*Spyrakos, 1996*]. The advantage of the FEM is its versatility. The structure analysed may have arbitrary shape, arbitrary supports and arbitrary loads [*Cook, 1994*]. For instance, silver epoxy of arbitrary shape added at the ends of the quartz plate as shown in Figure 1.12. However, there is also a drawback. The FEM simulation must give a result, even if an inappropriate algorithm has been chosen [*Adams, 1999*]. Therefore, the FEM users should have a basic understanding of the problem so that errors in the FEM results can be detected.

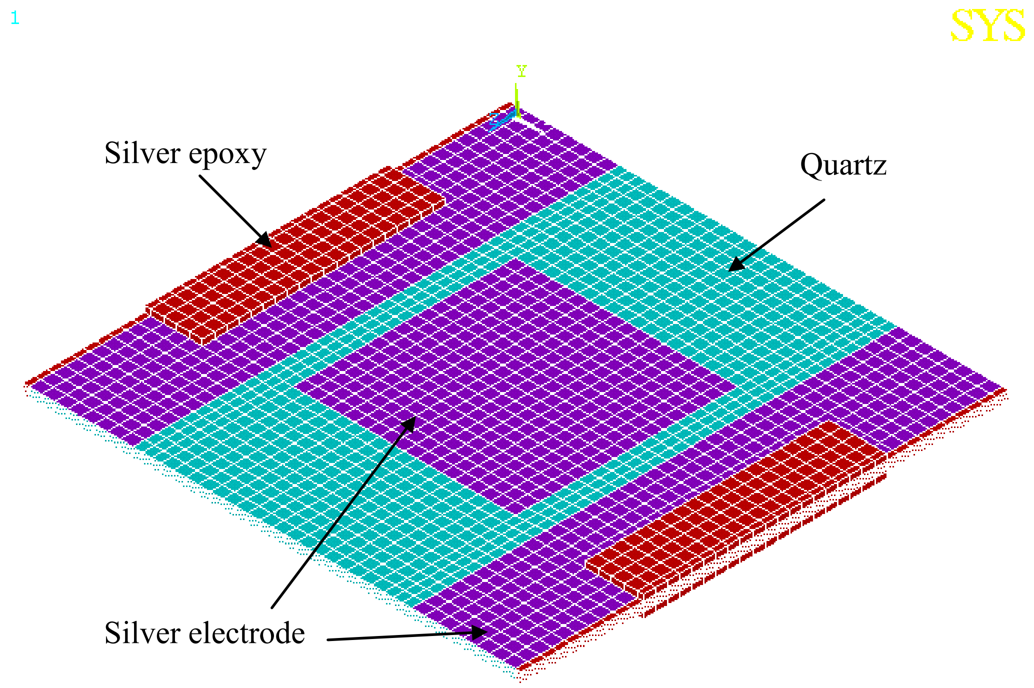

Figure 1.12 Silver epoxy of arbitrary shape added at the ends of the quartz plate.

In the FEM, an object is discretized into a number of linked simple geometric regions called finite elements or meshes. The material properties and the governing relationships are considered over these elements and expressed in terms of the unknown values at the element corners called nodes. An assembly process, considering the loading and constraints, results in a set of equations. Solution of these equations gives us the approximate behaviour of the object [*Chandrupatla, 1997*].

The solutions obtained with the FEM are only approximate. Nevertheless, the accuracy of the solutions can be improved by refining the element in the model using more elements and nodes.

A simple example is given to illustrate the underlying concept of the FEM [*Felippa, 2006*]. The example is to find the perimeter L of a circle of diameter d. Since $L = \pi d$, this is equivalent to obtaining a numerical value for π.

A circle of radius r and diameter $d = 2r$ is shown in Figure 1.13(a). The circle is replaced by a regular inscribed polygon of n sides, where $n = 8$ in Figure 1.13(b). This step is the finite element discretization, with the polygon sides as elements and vertices as nodes. The nodes are labelled with integers 1…8. A typical element is extracted, with nodes 4 and 5, as shown in Figure 1.13(c). Upon the finite element discretization, a generic element is defined, independent of the original circle, by the element connected by two nodes i and j as shown in Figure 1.13 (d). The relevant element property, the element length $L_{ij} = 2r \sin(\pi/n)$, is computed. Since all elements have the same length, the polygon perimeter is $L_n = n L_{ij}$, whence the approximation to π is $\pi_n = L_n/d = n \sin(\pi/n)$. This step is the assembly of the element equations and solution.

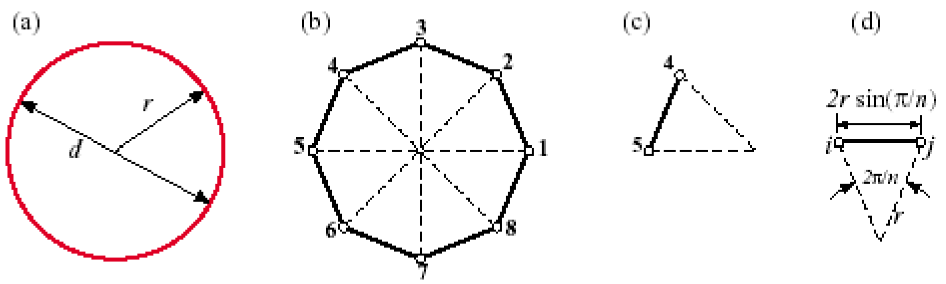

Figure 1.13 The “find π” problem treated with FEM concepts: (a) continuum object, (b) a discrete approximation by inscribed regular polygons, (c) disconnected element, (d) generic element [*Felippa, 2006*].

Table 1.3 Rectification of circle by inscribed polygons ("Archimedes FEM") [*Felippa, 2006*].

n	$\pi_n = n\sin(\pi/n)$	Extrapolated by Wynn-ϵ	Exact π to 16 places
1	0.000000000000000		
2	2.000000000000000		
4	2.828427124746190	3.414213562373096	
8	3.061467458920718		
16	3.121445152258052	3.141418327933211	
32	3.136548490545939		
64	3.140331156954753	3.141592658918053	
128	3.141277250932773		
256	3.141513801144301	3.141592653589786	3.141592653589793

Values of π_n obtained for n = 1, 2, 4, … 256 are listed in the second column of Table 1.3 . When the sides of the regular polygon n increases, the value of π_n approaches to the exact π value. This means that the accuracy of the solutions is improved by refining the element in the model using more elements and nodes.

1.4.2 Piezoelectric Analysis

A coupled-field analysis is an analysis that takes into account the interaction (coupling) between two or more disciplines (fields) of engineering. A piezoelectric analysis, for example, handles the interaction between the structural and electric fields: it solves for the voltage distribution due to applied displacements, or vice versa. Other examples of coupled-field analysis are thermal-stress analysis, thermal-electric analysis, and fluid-structure analysis [*ANSYS*].

In this project, quartz, a kind of piezoelectric materials, is concerned. To take into account the piezoelectric effect, a 3-D 20-nodes brick coupled-field element SOLID-226 is employed in defining the element type.

The coupling between the mechanical and the electrical quantities in the quartz is described by the constitutive equations as follows

$$\{T\} = [c]^E\{S\} - [e]\{E\} \tag{1.20}$$

$$\{D\} = [e]^T\{S\} + [\varepsilon]^S\{E\} \tag{1.21}$$

where $\{T\}$ is the stress vector, $\{D\}$ is the electric displacement vector, $\{S\}$ is the strain vector, $\{E\}$ is the electric field vector, $[c]^E$ is the elastic stiffness matrix at constant electric field, $[e]$ is the piezoelectric stress matrix, $[e]^T$ is the transpose of the piezoelectric stress matrix, $[\varepsilon]^S$ is the dielectric matrix at constant strain.

In the piezoelectric analysis, with the application of the variational principle and finite-element discretization, the coupled finite element matrix equations are derived [*Allik, 1970*]

$$[M]\{\ddot{u}\} + [C]\{\dot{u}\} + [K]\{u\} + [K^Z]\{V\} = \{F\} \tag{1.22}$$

$$[K^Z]^T\{u\} + [K^d]\{V\} = \{L\} \tag{1.23}$$

where $[M]$ is the structural mass matrix, $[C]$ is the structural damping matrix, $[K]$ is the structural stiffness matrix, $[K^Z]$ is the piezoelectric coupling matrix, $[K^Z]^T$ is the transpose of the piezoelectric coupling matrix, $[K^d]$ is the dielectric coefficient matrix, $\{\ddot{u}\}$ is the nodal acceleration vector, $\{\dot{u}\}$ is the nodal velocity vector, $\{u\}$ is the nodal displacement vector, $\{V\}$ is the electric potential vector, $\{F\}$ is the applied load vector, and $\{L\}$ is the electrical load vector.

[M] is related to the ρ, [C] is related to the damping factor, [K] is related to the $[c]^E$, $[K^Z]$ is related to the [e], and $[K^d]$ is related to the $[\varepsilon]^S$. The formulation can be found from the paper of Allik [*Allik, 1970*].

The coupled finite element matrix equations allow the finite elements to take into account both the direct and converse piezoelectric effects at the same time in one model. With the input of the mass density ρ, $[c]^E$, $[e]$, $[\varepsilon]^S$ of the quartz into ANSYS, the piezoelectric analysis can be performed.

1.4.3 Harmonic Analysis

For the step of obtaining solution, the analysis type has to be defined. Harmonic analysis is used in this project to simulate the impedance spectra and the vibration profiles of the quartz resonators.

The harmonic analysis is a technique to determine the steady-state response of a linear structure to applied loads that vary sinusoidally (*harmonically*) with time.

The idea is to calculate the structure's response at several frequencies and obtain a graph of some response quantity versus frequency. "Peak" responses are then identified on the graph and stresses reviewed at those peak frequencies. In this project, the load applied is electric potential and the response interested is electrical impedance of the quartz resonators.

This analysis technique calculates only the steady-state, forced vibrations of a structure. The transient vibrations, which occur at the beginning of the excitation, are not accounted for in a harmonic response analysis as shown in Figure 1.14.

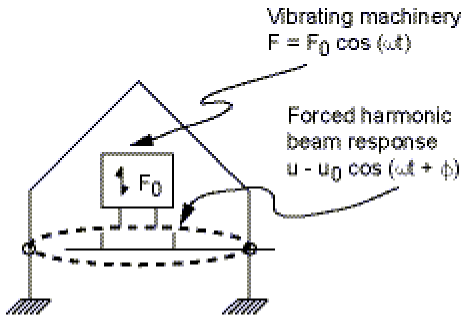

(a) F_o is known; while u_o and Φ are unknown.

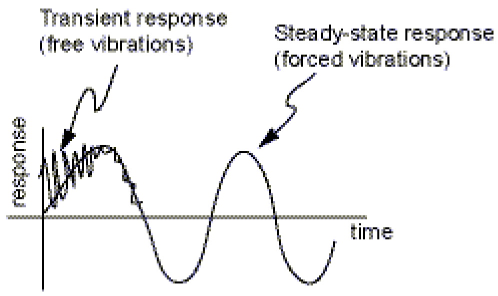

(b) Transient and steady-state dynamic response of the structural system.

Figure 1.14 Harmonic response systems [*ANSYS*].

In the harmonic analysis, the loads and displacements in the structure vary sinusoidally at the same frequency, however, not necessarily in phase. The sinusoidal loads, i.e. the electric potential, are specified through the parameters amplitude, phase angle, and forcing frequency range. Amplitude is the peak value of the load, and phase angle is the time lag between multiple loads that are out of phase with each other. On the complex plane, it is the angle measured from the real axis. Forcing frequency range is the frequency range of the harmonic load (in cycles/time) [*Madenci, 2006*]. Then, the above coupled finite element matrix equations are solved for the induced charge, i.e. the electrical impedance.

1.5 Scope of Work

The main objective of the present project is to develop a systematic and efficient procedure for applying the energy trapping technique to improve and optimize the performance of high frequency resonators (4 MHz – 70 MHz).

In Chapter 2, because the finite element method is used to simulate the resonance responses of the resonators and to study the energy trapping phenomenon caused by various electrode configurations, the details of using ANSYS, a commercial finite-element software, will be described. To have a basic idea of using ANSYS, the organization of ANSYS is introduced. The steps of analysis in ANSYS are introduced, and from these steps, the simulation considerations using ANSYS will be discussed.

In Chapter 3, the resonance responses of the fundamental thickness-shear AT-cut quartz resonators will be simulated using the finite element method (ANSYS). The effect of using different electrode lengths on the impedance spectra and the vibration modes will be simulated and compared with experimental results. The effect of the silver epoxy on the resonance responses will be studied.

In Chapter 4, third overtone thickness-shear resonators will be designed based on the previous studies on the energy trapping phenomenon. The effect of the silver epoxy on suppressing the fundamental thickness-shear mode will be explored. The third overtone resonators will be fabricated and characterized.

In Chapter 5, the conclusions and suggestions for future work are presented.

Chapter Two

Study of the Resonance Responses of the Fundamental Thickness-shear AT-cut Quartz Resonators

As mentioned in Chapter 1, there are many vibration modes in the AT-cut quartz crystal such as thickness-shear modes and flexural modes. For the vibration modes, only one of them is desired, it is usually the fundamental thickness-shear mode. Other modes are unwanted modes called spurious modes. And to suppress the spurious modes, energy trapping technique is used.

Two types of AT-cut quartz resonators, 4-MHz and 27-MHz (provided by Hong Kong X'tals Ltd.), are used to study the energy trapping phenomenon. The resonance responses of these two resonators will be simulated using ANSYS (the general purpose finite element software).

First, it is necessary to input the material properties into ANSYS. The material properties for the AT-cut quartz, silver, and silver epoxy are given as follows.

The material properties for the AT-cut quartz are [*Tiersten, 1969*]:

$$c^E = \begin{pmatrix} 86.7 & -8.25 & 27.2 & -3.66 & 0 & 0 \\ -8.25 & 130 & -7.42 & 5.70 & 0 & 0 \\ 27.2 & -7.42 & 103 & 9.92 & 0 & 0 \\ -3.66 & 5.70 & 9.92 & 38.6 & 0 & 0 \\ 0 & 0 & 0 & 0 & 68.8 & 2.53 \\ 0 & 0 & 0 & 0 & 2.53 & 29.0 \end{pmatrix} \times 10^9 \, N/m^2$$

$$e = \begin{pmatrix} 0.171 & -0.152 & -0.0187 & 0.067 & 0 & 0 \\ 0 & 0 & 0 & 0 & 0.108 & -0.095 \\ 0 & 0 & 0 & 0 & -0.0761 & 0.067 \end{pmatrix} C/m^2$$

$$\frac{\varepsilon^S}{\varepsilon_0} = \begin{pmatrix} 4.35 & 0 & 0 \\ 0 & 4.44 & 0.14 \\ 0 & 0.14 & 4.54 \end{pmatrix}$$

$$\rho = 2649 \text{ kg/m}^3$$

The material properties for the silver are:

$$\text{Young's modulus} = 7.241 \times 10^{10} \text{ N/m}^2$$

$$\text{Poisson's ratio} = 0.37$$

$$\rho = 10500 \text{ kg/m}^3$$

The material properties for the silver epoxy are:

$$\text{Young's modulus} = 5 \times 10^{9} \text{ N/m}^2$$

$$\text{Poisson's ratio} = 0.4$$

$$\rho = 3000 \text{ kg/m}^3$$

Also, damping factor is input for the silver epoxy. The value of the damping factor varies from cases to cases.

It should be noted that the surfaces of the commercial 4-MHz AT-cut quartz resonators are made into lenses shapes by a process called contouring, while in this study, model with simple flat quartz plate is used for the simulations. For the 27-MHz AT-cut quartz resonators, the commercial product and the model are of flat plates.

The dimensions of the 4-MHz and 27-MHz AT-cut quartz plates are as follows, with reference to Figure 2.1.

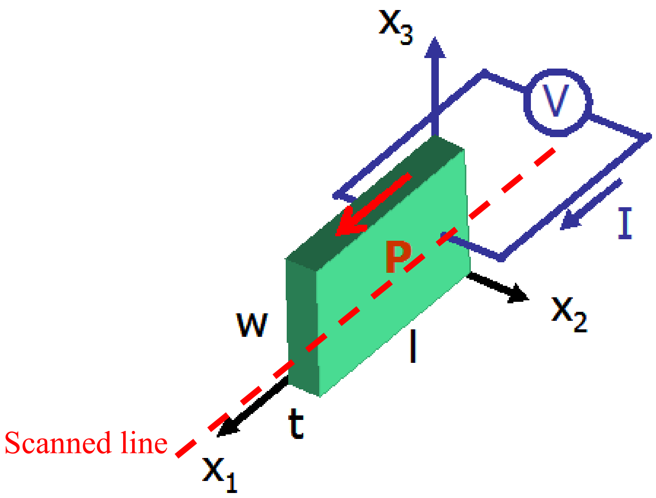

4 MHz

l = 8 mm, w = 2.2 mm, t = 0.415 mm

27 MHz

l = 5 mm, w = 2.51 mm, t = 0.06025 mm

Figure 2.1 An AT-cut quartz resonator of simple geometry.

2.1 Verification

As mentioned in Chapter 1, the technique of using the FEA software (ANSYS) must be verified first. It is because the FEA software must give results, it is, therefore, unwise to assume that all the results given by the FEA software are accurate. In this section, the FEA software will be used to simulate the impedance spectrum for a simplified case, i.e. an AT-cut quartz resonator with only the thickness-shear vibration; and the results will be compared with those derived from a simplified model so as to verify the technique and understanding in using the FEA software.

In this section, the impedance spectrum of the 4-MHz quartz resonator is simulated with the following assumptions. There is no electrode applied to the top and bottom surfaces of the AT-cut quartz resonator, although electric field is applied in the X_2 direction. There are no electrical and mechanical losses of the quartz resonator. Also, there is no clamping to the quartz resonator.

To take into account only the thickness-shear vibration in the X_1–X_2 plane in ANSYS, all the material parameters, except c_{66}^{E}, e_{26}, ε_{22}^{S} and ρ, are assumed to be zero. This corresponds to the case with the following constitutive equations [*Ikeda, 1990*].

$$T_6 = c_{66}^{E} S_6 - e_{26}E_2 \quad (2.1)$$

$$D_2 = \varepsilon_{22}^{S} E_2 + e_{26}S_6 \quad (2.2)$$

where, E_2 is the electric field in the X_2 direction, S_6 is the shear strain in the X_1-X_2 plane, T_6 is the shear stress about the X_3 axis, D_2 is the electric displacement in the X_2 direction. That is, with the application of the electric field in the X_2 direction, only the thickness-shear vibration in the X_1–X_2 plane is present in the quartz resonator.

With the above assumptions, the impedance spectrum for the (4-MHz) resonator at the fundamental thickness-shear mode is simulated and shown in Figure 2.2. The corresponding vibration mode shapes at f_{111} and f_{131} in the X_1–X_2 plane at the center of the quartz plate (i.e. at X_3 = 1.1 mm in Figure 2.1) are shown in Figures 2.3 and 2.4, respectively.

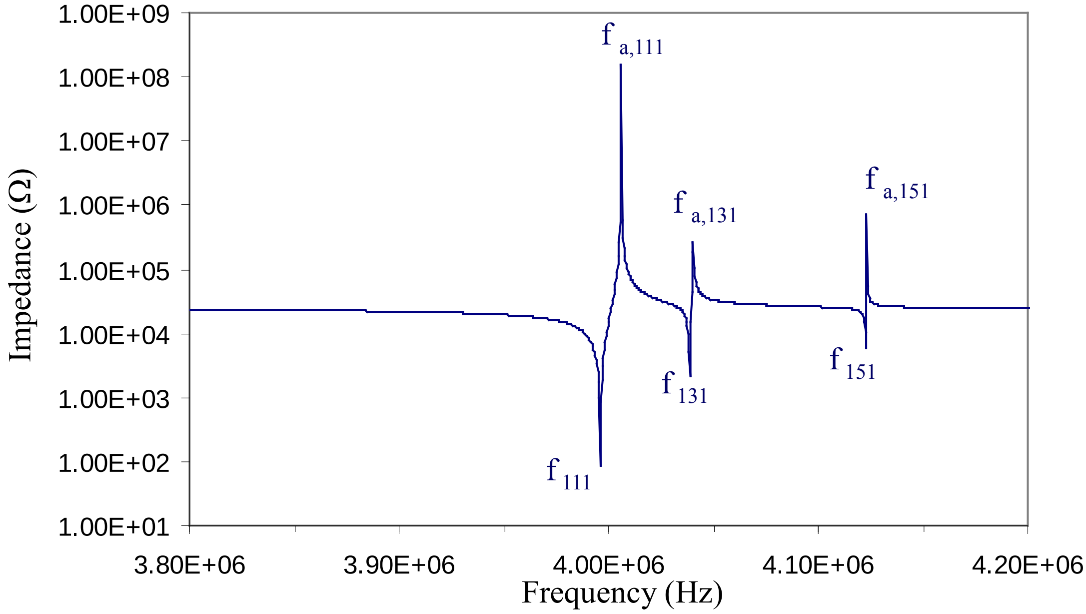

Figure 2.2 The simulated impedance spectrum for the (4-MHz) AT-cut quartz resonator at the thickness-shear resonance modes.

Figure 2.3 The simulated vibration mode shape at f_{111} in the X_1–X_2 plane at the center of the quartz plate (X_3 = 1.1 mm).

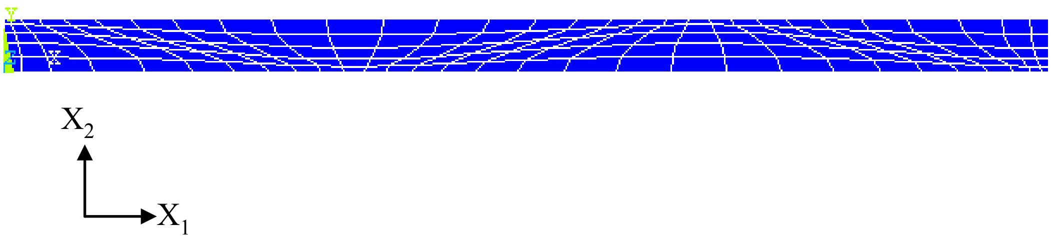

Figure 2.4 The simulated vibration mode shape at f_{131} in the X_1–X_2 plane at the center of the quartz plate (X_3 = 1.1 mm).

As shown in Figure 2.2, there are several resonance peaks in the simulated impedance spectrum. The vibration (pattern) corresponding to each resonance peak can be examined in ANSYS and thus the corresponding modes can be identified. The resonance peak at f_{111} is associated with the fundamental thickness-shear vibration mode (Fig. 2.3) which is the wanted mode for resonator applications, while the resonance peaks at f_{131} and f_{151} are associated with the inharmonic thickness-shear vibration modes (Fig. 2.4) which are the unwanted mode, usually called the spurious modes. Accordingly, f_{111} and $f_{a,111}$ are the resonance frequency and anti-resonance frequencies of the fundamental thickness-shear vibration mode, respectively; f_{131} and $f_{a,131}$ are the resonance and anti-resonance frequencies of the third-inharmonic thickness-shear vibration mode, while f_{151} and $f_{a,151}$ are for fifth-inharmonic thickness-shear vibration mode.

As shown in Figure 2.3, the fundamental thickness-shear vibration is quite "pure". As only the thickness-shear vibration is taken into account for the simulation (refer to Eqs. 2.1 and 2.2), the other mode of vibrations does not exist and coupled to the thickness-shear vibration, thus giving a "pure" and uniform vibration mode shape.

The difference between the mode shapes at f_{111} and f_{131} is the number of half-wavelengths along the X_1 direction. As shown in Figure 2.3, there are one half-wavelength along the X_2 direction and one half-wavelength along the X_1 direction for the mode shape at f_{111}. For the mode shape at f_{131}, there are one half-wavelength along the X_2 direction and three half-wavelengths along the X_1

direction.

It has been shown that, by neglecting all other resonance modes, the anti-resonance frequency of the thickness-shear vibration modes in a rectangular plate of thickness t, length l and width w is given as [*Bottom, 1982*]:

$$f_{a,nmp} = \frac{v}{2}\sqrt{\left(\frac{n}{t}\right)^2 + \left(\frac{m}{l}\right)^2 + \left(\frac{p}{w}\right)^2} \qquad ; n, m, p = 1, 3, 5, \ldots \qquad (2.3)$$

where ν ($v = \sqrt{c_{66}^D/\rho}$) is the velocity of the thickness-shear wave in the plate along the X_2 direction. For AT-cut quartz, ν = 3323 m/s. Since only the thickness-shear vibration in the X_1–X_2 plane is considered, the vibration is uniform in the X_3 direction. This implies that the thickness-shear resonance modes are independent of the width dimension, i.e. w becomes infinity for Eq. 2.3. Accordingly, the anti-resonance frequencies for the fundamental and inharmonic thickness-shear modes are calculated as follows:

$$f_{a,111} = 4.008 \text{ MHz}$$

$$f_{a,131} = 4.051 \text{ MHz}$$

$$f_{a,151} = 4.135 \text{ MHz}$$

It can be seen that the calculated anti-resonance frequencies (using Eq. 2.3) agree with those observed from the simulated impedance spectrum (Fig. 2.2). Therefore, the technique of using ANSYS has been verified and further simulation studies using ANSYS can be carried out.

2.2 Simulations of Resonance Responses

2.2.1 4-MHz Resonators

2.2.1.1 Resonators with Full Electrodes

Hereafter, the full set of the material parameters of the AT-cut quartz is used for the simulations. First, a full electrode of thickness 0.6 μm (i.e. the width and length of the electrode are the same as those of the quartz plate) is added to the quartz plate (Fig. 2.1). Again, no electrical and mechanical losses of the quartz plate and no clamping to the quartz plate are assumed for the simulations. With the above assumptions, the impedance spectrum for the resonator has been simulated and shown in Figure 2.5. The vibration mode shape at f_{111} in the X_1–X_2 plane at the center of the quartz plate (i.e. at X_3 = 1.1 mm) is shown in Figure 2.6, while the simulated vibration displacements U_1 (the displacement in X_1 direction) and U_2 (the displacement in X_2 direction) at f_{111} along the scanned line (a line along X_1 direction at the center and top surface of the quartz plate as shown in Fig. 2.1) are shown in Figures 2.7a and 2.7b, respectively.

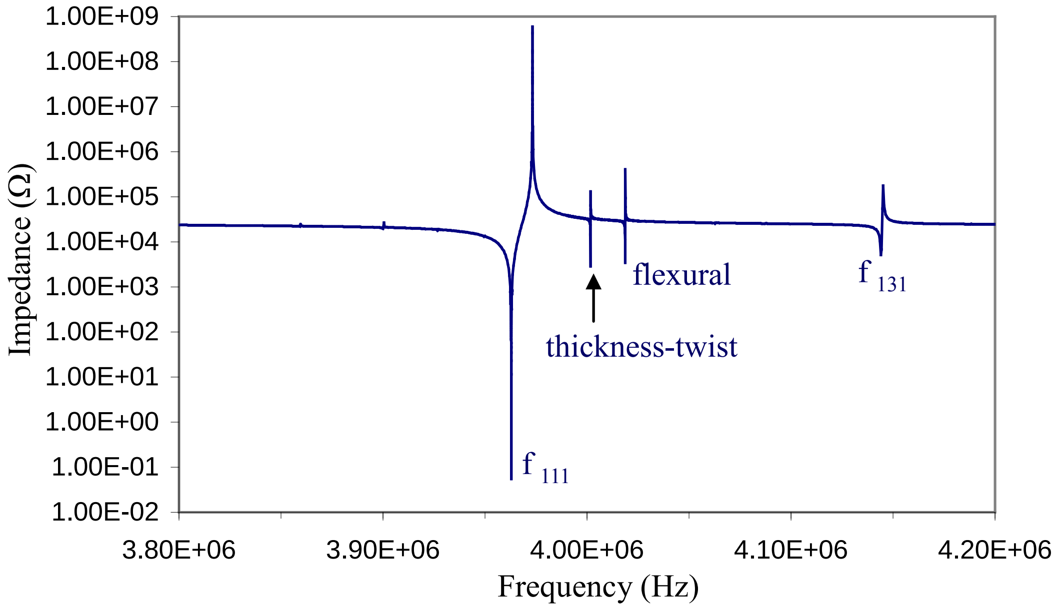

Figure 2.5 The simulated impedance spectrum for the quartz resonator with full electrode of thickness 0.6 μm.

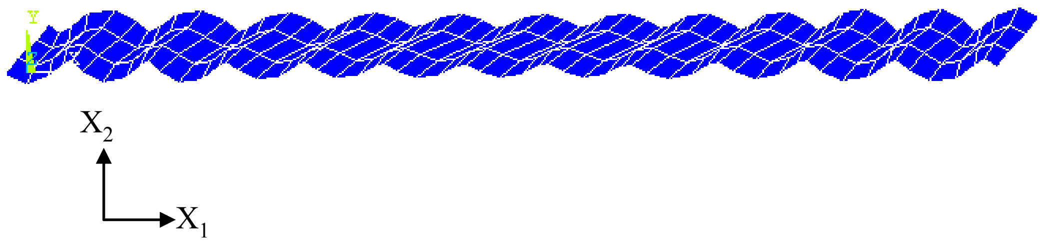

Figure 2.6 The simulated vibration mode shape at f_{111} in the X_1–X_2 plane at the center of the quartz resonator (X_3 = 1.1 mm) with full electrode of thickness 0.6 μm.

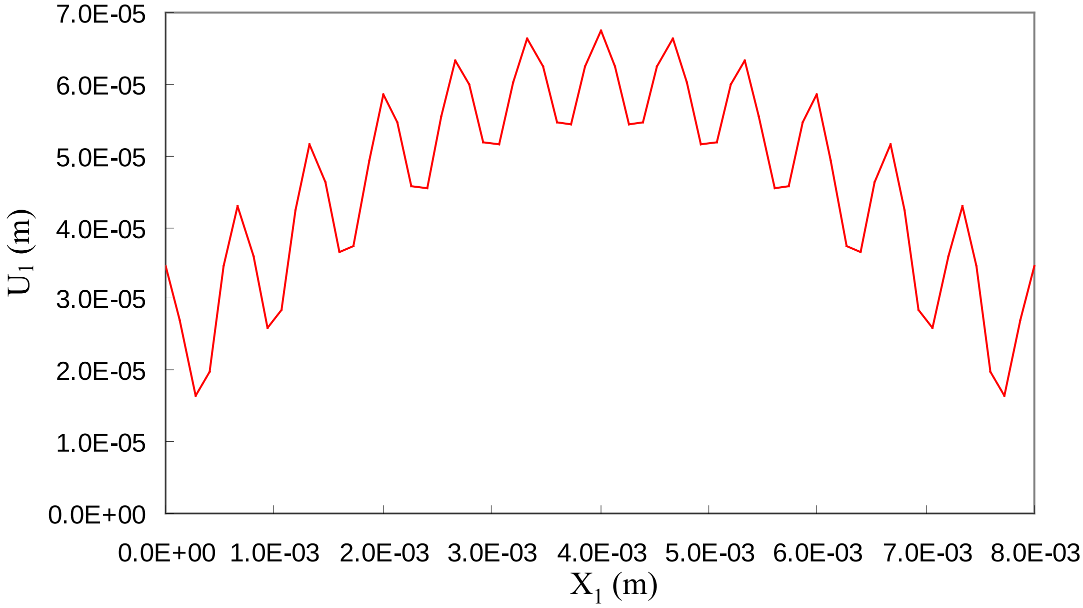

(a)

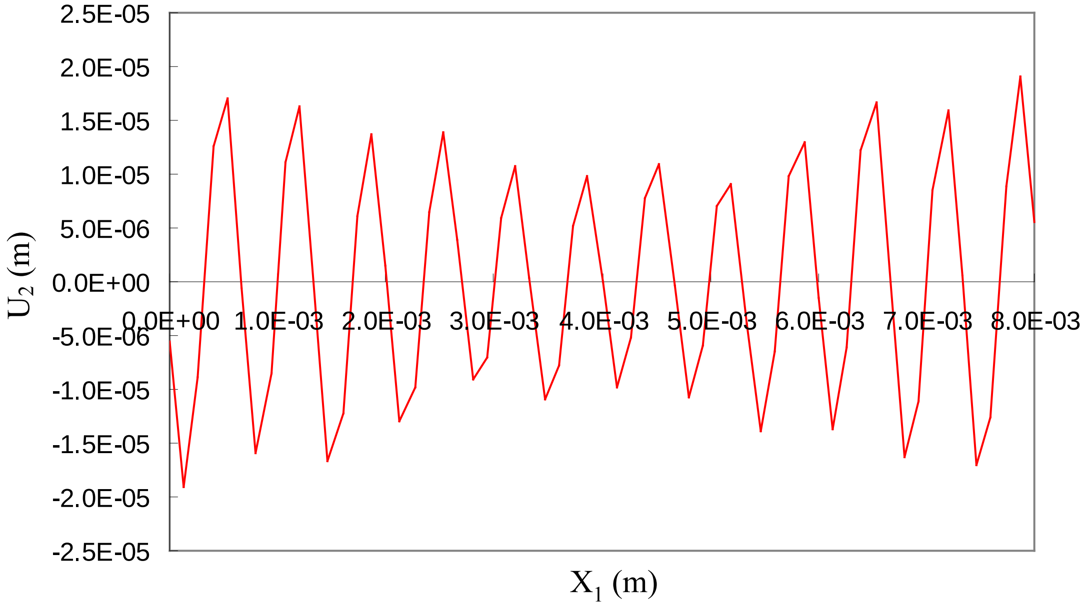

(b)

Figure 2.7 (a) The simulated vibration displacements U_1 in the X_1 direction at f_{111} along the scanned line for the quartz resonator with full electrode of thickness 0.6 μm. (b) The simulated vibration displacements U_2 in the X_2 direction at f_{111} along the scanned line for the quartz resonator with full electrode of thickness 0.6 μm.

As shown in Figure 2.5, there exist resonant peaks associated with the fundamental thickness-shear mode (f_{111}) as well as the spurious modes, such as thickness-twist mode, flexural mode, and inharmonic thickness-shear mode (f_{131}). As it is assumed that there are no electrical and mechanical losses for the quartz plate, the impedance at f_{111} is very small. In fact, if a finer resolution in frequency is used for the simulation, the impedance at f_{111} should become even smaller and close to zero. As the thickness-twist and the flexural modes are close to the fundamental thickness-shear mode, strong coupling occurs, giving a non-uniform vibration mode shape (Fig. 2.6) and non-"pure" thickness-shear mode vibration at f_{111} (Fig. 2.7a). Because of the coupling from the flexural mode vibration (where the dominant vibration displacement is in X_2 direction), the simulated vibration displacement U_2 in X_2 direction (Fig. 2.7b) is comparable to U_1 in X_1 direction (Fig. 2.7a) at f_{111} along the scanned line, and giving non-"pure" thickness-shear mode vibration at f_{111} (ripples in the vibration displacement U_1 as shown in Figure 2.7a). Besides, unlike the case in which only the thickness-shear mode vibration is considered (Fig. 2.3), the vibration spread over the quartz plate such that the one half-wavelength condition along the X_1 (i.e. length) direction for the fundamental resonance is not held. The corresponding wavelength is larger than twice of the length of the quartz plate. In other words, the "effective" length for the fundamental resonance is larger than the real one. This is part of the reasons for the smaller f_{111} value observed from the simulated impedance spectrum (~ 3.963 MHz) as compared to the value calculated from Eq. 2.3 (4.008 MHz). The more important reason for the decrease in f_{111} is the loading effect due to the full electrodes.

2.2.1.2 Resonators with Small Electrodes

Effects of Electrode Length

To suppress the spurious modes and then obtain a "pure" thickness-shear mode vibration, the energy trapping technique is used. It is done by using electrodes of smaller size than the quartz plate. The electrode configuration for the 4-MHz quartz resonators is shown in Figure 2.8.

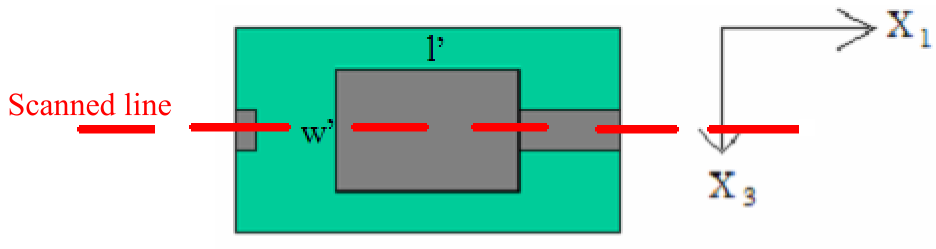

The dimensions of the electrode are:

l' = 5.4 mm, w' = 1.6 mm, t' = 0.6 μm

Figure 2.8 The electrode configuration for the 4-MHz quartz resonators.

t' is the thickness of the electrode in the X_2 direction, which is normal to both X_1 and X_3 direction. The dimensions of the quartz plate are the same as the one shown in Figure 2.1. The silver electrode is located at the centre of the quartz plate. Again, no electrical and mechanical losses of the quartz plate, and no clamping to the quartz plate are assumed for the simulations in this section. The simulated impedance spectrum for the resonator is shown in Figure 2.9. The vibration mode shape at f_{111} in the X_1–X_2 plane at the center of the quartz plate (i.e. at X_3 = 1.1 mm) is shown in Figure 2.10, while the simulated vibration displacements U_1 (the displacement in X_1 direction) at f_{111} along the scanned line (a line along X_1 direction at the center and top surface of the quartz plate as shown in Fig. 2.8) is shown in Figure 2.11.

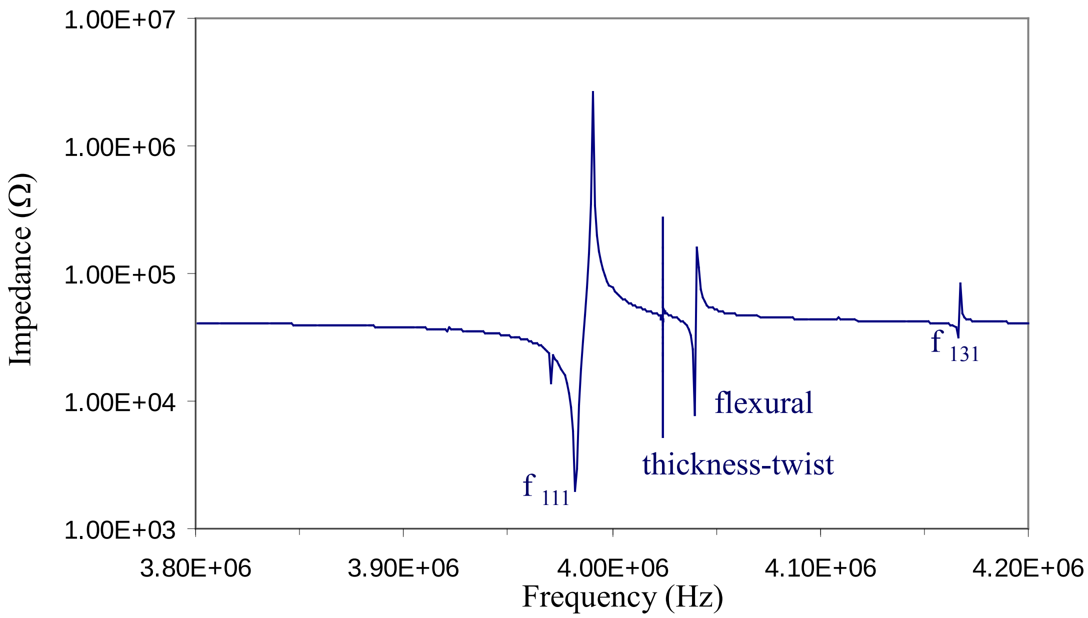

Figure 2.9 The simulated impedance spectrum for the quartz resonator with an electrode of length 5.4 mm, width 1.6 mm and thickness 0.6 μm.

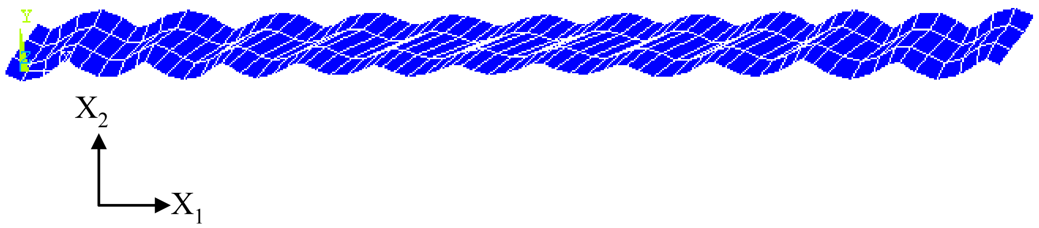

Figure 2.10 The simulated vibration mode shape at f_{111} in the X_1–X_2 plane at the center of the quartz resonator (X_3 = 1.1 mm) with an electrode of length 5.4 mm, width 1.6 mm and thickness 0.6 μm.

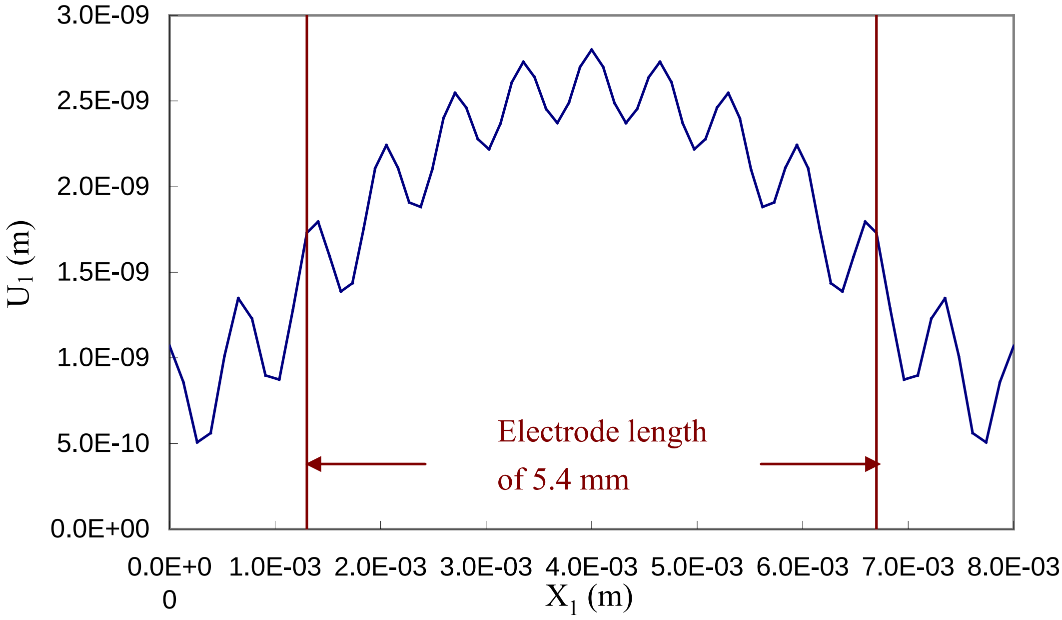

Figure 2.11 The simulated vibration displacement U_1 in the X_1 direction at f_{111} along the scanned line for the quartz resonator with an electrode of length 5.4 mm, width 1.6 mm and thickness 0.6 µm. The two vertical lines at X_1 = 1.3 mm and X_1 = 6.7 mm indicate the position of the electrode.

As shown in Figure 2.9, the spurious modes (such as the thickness-twist mode, the flexural mode and the inharmonic thickness-shear mode) still exist next to the fundamental thickness-shear resonance mode (f_{111}) for the resonator with a "small" electrode. As a result of coupling, the vibration mode shape at f_{111} is not uniform (Fig. 2.10), and the vibration is not "pure" thickness-shear mode and spread over the quartz plate (Fig. 2.11). However, as compared to the resonator with full electrodes (Fig. 2.7a), the spreading of the vibration is slightly decreased (i.e. a smaller "effective" quartz length), and thus giving a slightly higher f_{111} value (Fig. 2.9). It can be seen that, as the "small" electrodes can not effectively trap the vibration under the electrode, the resonance frequencies, including those for the fundamental and inharmonic modes, depend only slightly on the length of the electrode.

Similar simulation results have also been observed for the vibration along a scanned line in the width direction (i.e. a scanned line normal to the one shown in Fig. 2.8). That is, the vibration also spreads to the side edges of the quartz plate, and the resonance frequencies depend only slightly on the width of the electrode.

On the basis of the above simulations, it can be seen that the introduction of an unelectroded region (i.e. a electrode smaller than the quartz plate) does not ensure an effective trapping of the wanted vibration. According to the energy trapping theory (Chapter 1), because of the mass loading effect, the cutoff frequency in the electroded region (which is the resonance frequency of the fundamental thickness-shear mode) is smaller than that in the unelectroded region; so the thickness-shear vibration cannot propagate freely in the unelectroded region. Instead, the vibration will decay exponentially with distance away from the electrodes. However, by simply considering the cutoff frequency, there is no way to predict the effectiveness of the energy trapping, as shown in the above simulations. Hence, the energy trapping efficiency, which is related to how fast the vibration decays from the electrodes, should be considered. Clearly, it should depend on the difference of the cutoff frequencies in the electroded and unelectroded regions as well as the frequency of the vibration (i.e. the wavelength as compared to the distance).

Effects of Electrode thickness

In this section, the effect of the electrode thickness on the resonance responses is studied. The impedance spectrum for the resonators with electrode of different thicknesses is simulated. As there are factors other than the electrode thickness, e.g. energy trapping efficiency, affecting the resonance frequency, resonators with full electrodes are first examined. In general, similar resonance responses have been observed for resonators with different electrode thickness (Fig. 2.5). However, due to the mass loading effect, the resonance frequency decreases with increasing thickness. The decrease is found to be about 7 kHz/0.1μm.

Next, the effect of the electrode thickness (i.e. the difference of the cutoff frequencies in the electroded and unelectroded regions) on the energy trapping efficiency is examined. Resonators with electrode of thickness 0.3 μm, 0.6 μm and 2 μm are studied. For all cases, the electrode has a width of 1.6 mm and a length of 5.4 mm (Fig. 2.8). The simulated vibration displacement (normalized) U_1 at f_{111} along the scanned line (Fig. 2.8) for the resonators are compared in Figure 2.12. It can be seen that the vibration is trapped more effectively in the electroded region with an increase of the electrode thickness. As the electrode thickness increases, the cutoff frequency in the electroded region decreases, i.e. the difference from the cutoff frequency in the unelectroded region increases. According to the energy trapping theory, this will increase the imaginary value of the wave vector ζ (Eq. 1.8) and hence the vibration will decay faster from the electrodes. In other words, the vibration will be more trapped in the electroded region, or the energy trapping efficiency increases. As shown in Figure 2.12, electrode of thickness 2 μm or above should be used for the 4-MHz resonators in order to trap the wanted mode vibration. However, because of the technical difficulties in the deposition of thick electrodes and cost saving, such a thick electrode will not be used in the production. For the commercial products, the thickness of the electrodes is 0.6 μm.

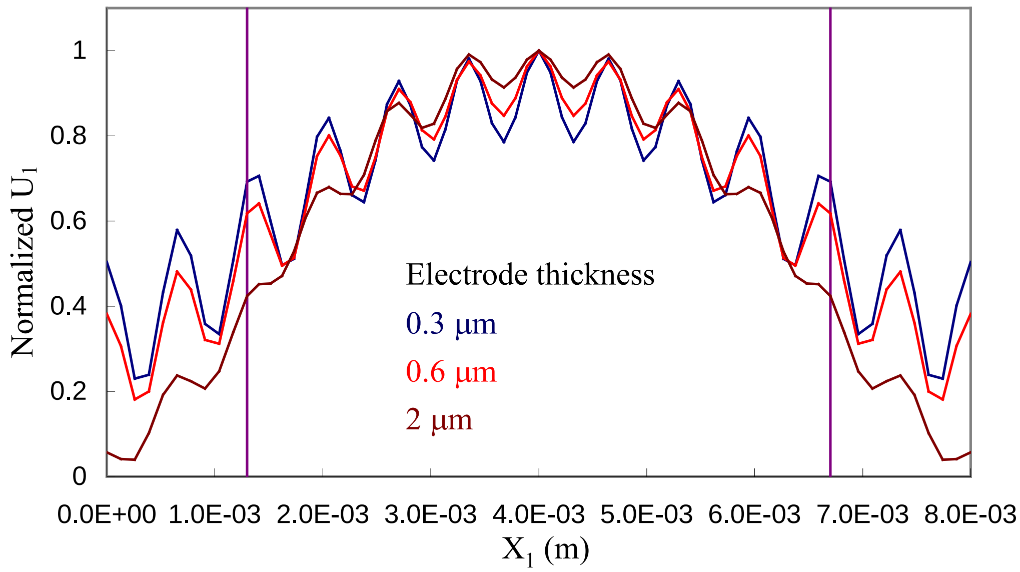

Figure 2.12 The simulated vibration displacement (normalized) U_1 at f_{111} along the scanned line for the quartz resonator with an electrode of length 5.4 mm, width 1.6 mm and various electrode thicknesses. The two vertical lines at X_1 = 1.3 mm and X_1 = 6.7 mm indicate the position of the electrode.

Effects of Silver Epoxy

In this section, the effect of silver epoxy on the resonance responses is studied. For the commercial resonators (4 MHz), the quartz plate is held at two ends by the silver epoxy. Correspondingly, silver epoxy is added to the resonator model as shown in Figure 2.13 for the simulation. The end of the quartz plate is embedded in the silver epoxy of which the length l'' is 0.5 mm, the width w'' is 2.2 mm and the thickness is 0.415 mm. The lossy characteristics of the silver epoxy is modelled by a damping factor of 1×10^{-8} in ANSYS. The damping factor is determined by simulating impedance spectra with different damping factors, and compared the simulated impedance at resonance with the measured one. The damping factor is determined when the simulated and measured impedance at resonance are comparable with each other. The dimensions for the resonator and electrodes are the same as those for Figure 2.8. The simulated impedance spectrum for the resonator is shown in Figure 2.14, in which the simulated impedance spectrum for the resonator without silver epoxy (i.e. Fig. 2.9) is also plotted for comparison. The corresponding simulated vibration displacements (normalized) U_1 (the displacement in X_1 direction) at f_{111} along the scanned line for the resonator with and without (Fig. 2.12) silver epoxy are shown in Figure 2.15.

Figure 2.13 The configuration for the 4-MHz quartz resonator with the silver epoxy.

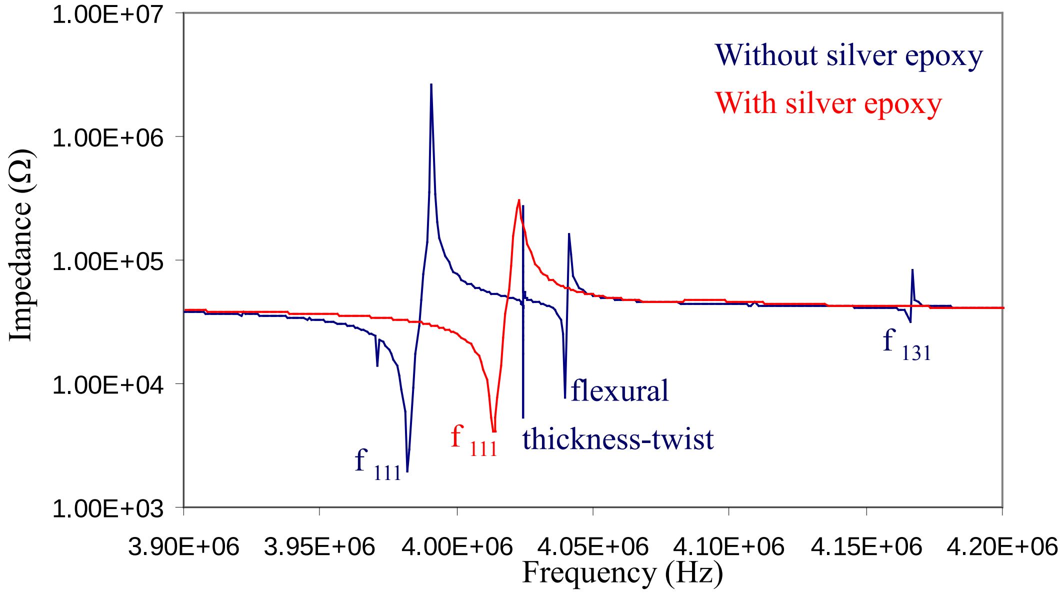

Figure 2.14 The simulated impedance spectrum for the quartz resonator with an electrode of length 5.4 mm, width 1.6 mm and thickness 0.6 μm and with silver epoxy with damping factor of 1×10^{-8}. The simulated impedance spectrum for the resonator without silver epoxy is also plotted for comparison.

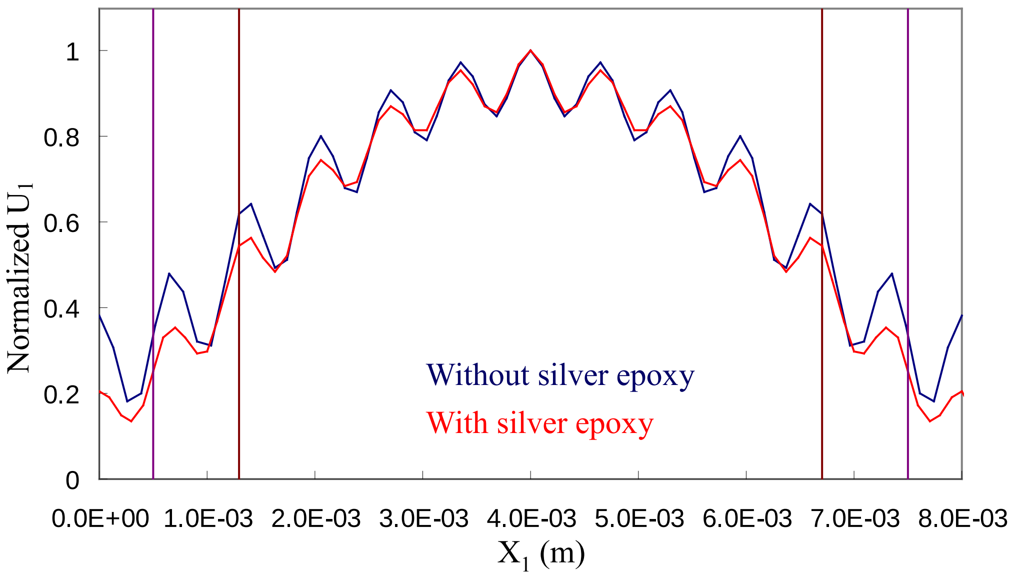

Figure 2.15 The simulated vibration displacement (normalized) U_1 in the X_1 direction at f_{111} along the scanned line for the quartz resonator with an electrode of length 5.4 mm, width 1.6 mm and thickness 0.6 μm and with silver epoxy with damping factor of 1×10^{-8}. The simulated vibration displacement (normalized) U_1 in the X_1 direction at f_{111} along the scanned line for the quartz resonator without silver epoxy is also plotted for comparison. The two vertical brown lines at X_1 = 1.3 mm and X_1 = 6.7 mm indicate the position of the electrode, while the two vertical purple lines at X_1 = 0.5 mm and X_1 = 7.5 mm indicate the position of the silver epoxy.

As shown in Figure 2.14, after the introduction of the lossy silver epoxy, all the spurious modes adjacent to the fundamental thickness-shear mode disappear (or move to higher frequencies). Besides, the impedance at f_{111} increases to a high value of about 4000 Ω. It should be noted that, as mentioned before, as there is no mechanical loss assumed for the quartz plate, the impedance at f_{111} for the resonator without silver epoxy is very small and close to zero if the frequency step used in the simulation is sufficiently small. However, for the resonator with silver epoxy, the impedance at f_{111} is not small and does not change significantly even when the frequency step is further decreased. So, it is not artificial and is able to show the effect of the silver epoxy which is discussed below.

As shown in the previous section, the thickness-shear mode vibration is not effectively trapped under the electroded region and spread to the ends of the resonators. For the other vibration modes, their frequency is higher than the cutoff frequency in the unelectroded region. So, they can propagate freely in the quartz plate. As the silver epoxy is a lossy material, it will absorb the energy of vibration at the ends of the quartz plate. In other words, the corresponding vibration modes are damped by the silver epoxy. Indeed, the damping is dependent on the spreading of the vibration to the ends of the quartz plate. As there is only the fundamental thickness-shear mode vibration having an imaginary wave vector, the damping for it should be minimal. Therefore, while all the spurious modes disappear (or move to higher frequencies), the thickness-shear resonance mode still exist. However, as a certain amount of the vibration energy is absorbed by the silver epoxy, the vibration displacement decreases and hence the impedance at f_{111} increases. As shown in Figure 2.15, the spreading of the vibration for the resonator with silver epoxy is decreased (i.e. a smaller "effective" quartz length), thus f_{111} increases.

2.2.2 27-MHz Resonator

2.2.2.1 Resonators with Full Electrodes

In this section, the resonance responses of a 27-MHz resonator are studied. Similar to the cases for 4-MHz resonators, the effects of electrode length and thickness are examined. Based on the results, the energy trapping phenomenon is discussed.

First, the resonance responses of a 27-MHz resonator with full electrodes are studied. The dimensions of the quartz plate are the same as the one shown in Figure 2.1. The thickness of the electrode is 0.2 μm (which is the thickness for the commercial resonators). Again, no electrical and mechanical losses of the quartz plate and no clamping to the quartz plate are assumed for the simulations. With the above assumptions, the impedance spectrum for the resonator has been simulated and shown in Figure 2.16. The simulated vibration displacements U_1 (the displacement in X_1 direction) at f_{111} along the scanned line (a line along X_1 direction at the center and top surface of the quartz plate as shown in Fig. 2.1) is shown in Figure 2.17.

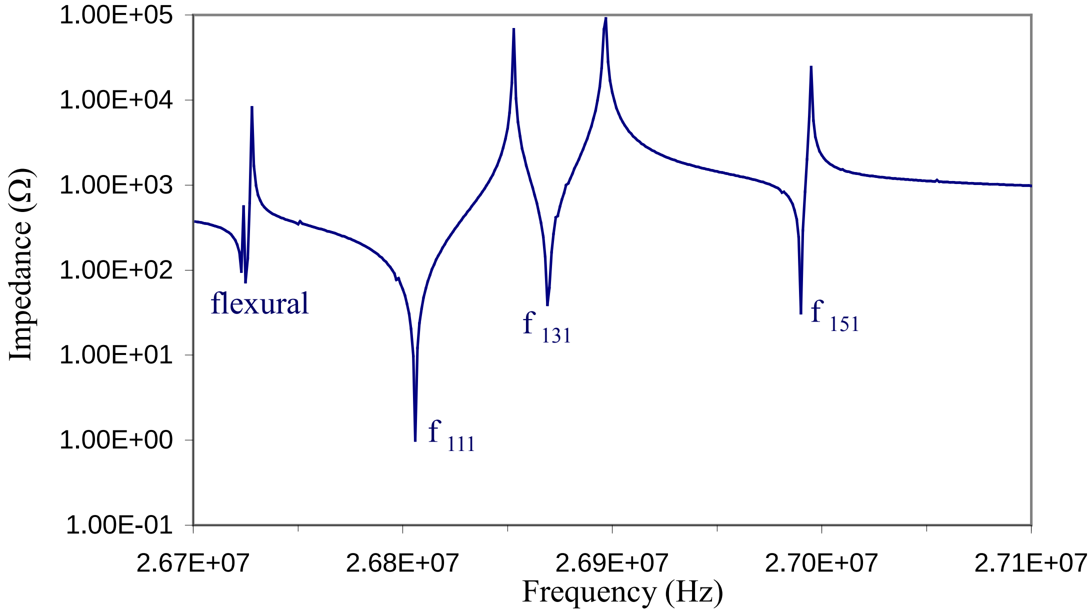

Figure 2.16 The simulated impedance spectrum for the quartz resonator with full electrode of thickness 0.2 μm.

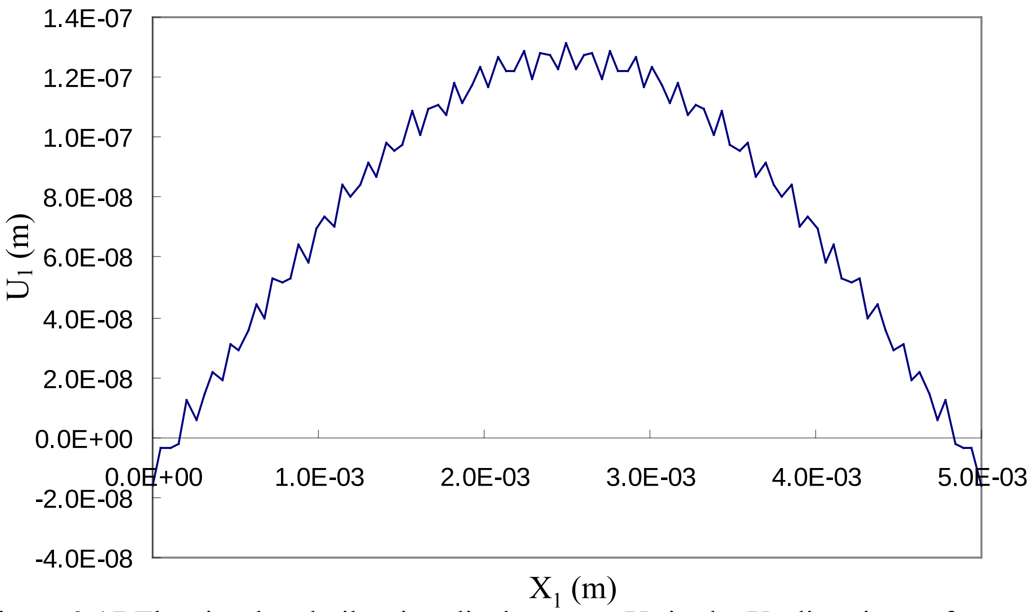

Figure 2.17 The simulated vibration displacement U_1 in the X_1 direction at f_{111} along the scanned line for the quartz resonator with full electrode of thickness 0.2 μm.

Similar to the 4-MHz resonator, the fundamental thickness-shear mode as well as the spurious modes, such as the flexural mode and the inharmonic thickness-shear modes, exist close to each others for the 27-MHz resonator with full electrodes (Fig. 2.16). Because of strong mode coupling by the flexural mode, the vibration at f_{111} is not "pure" thickness-shear mode (Fig. 2.17).

2.2.2.2 Resonators with Small Electrodes

Effects of Electrode Length

In this section, the effects of a "small" electrode on the resonance responses for the 27-MHz resonator are studied. The electrode configuration is shown in Figure 2.18.

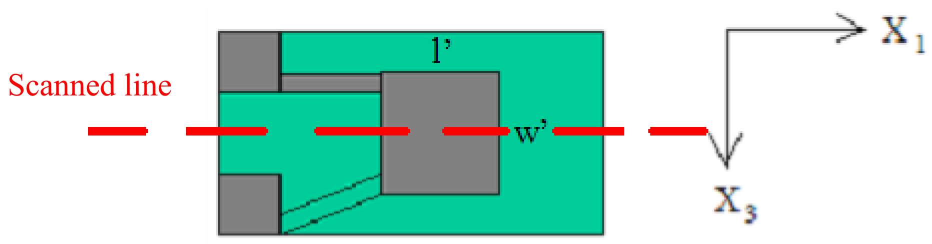

The dimensions of the electrode are:

l' = 2 mm, w' = 1.2 mm, t' = 0.2 μm

Figure 2.18 The electrode configuration for the 27-MHz quartz resonators.

The dimensions of the quartz plate are the same as the one shown in Figure 2.1. The silver electrode is located at the centre of the quartz plate. Again, no electrical and mechanical losses of the quartz plate, and no clamping to the quartz plate are assumed for the simulations in this section. The simulated impedance spectrum for the resonator is shown in Figure 2.19. The simulated vibration displacements U_1 (the displacement in X_1 direction) at f_{111} and f_{131} along the scanned line (a line along X_1 direction at the center and top surface of the quartz plate as shown in Fig. 2.18) is shown in Figures 2.20 and 2.21, respectively.

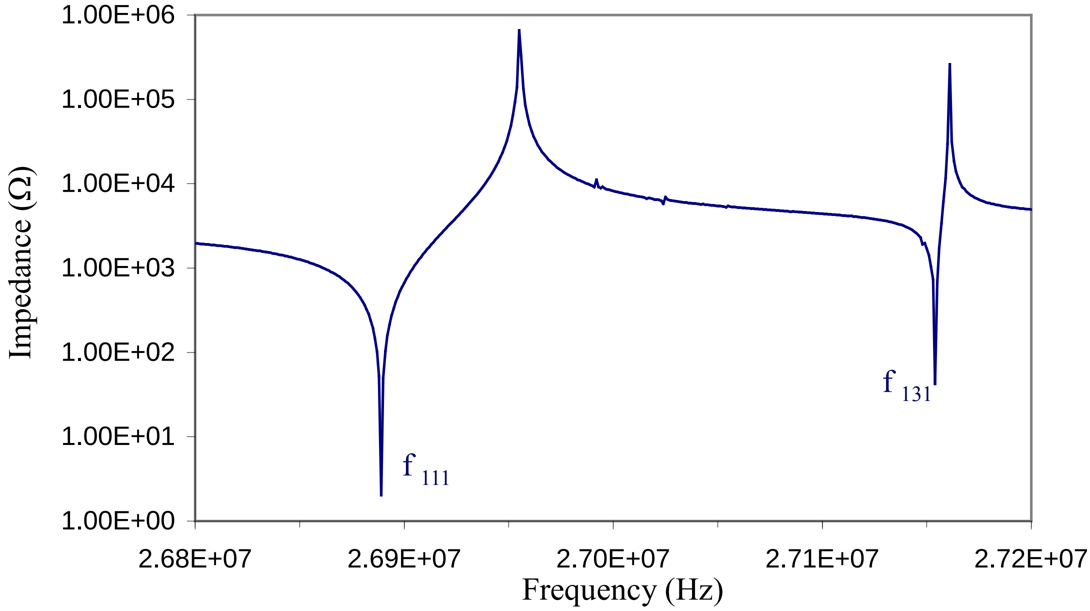

Figure 2.19 The simulated impedance spectrum for the quartz resonator with an electrode of length 2 mm, width 1.2 mm and thickness 0.2 μm.

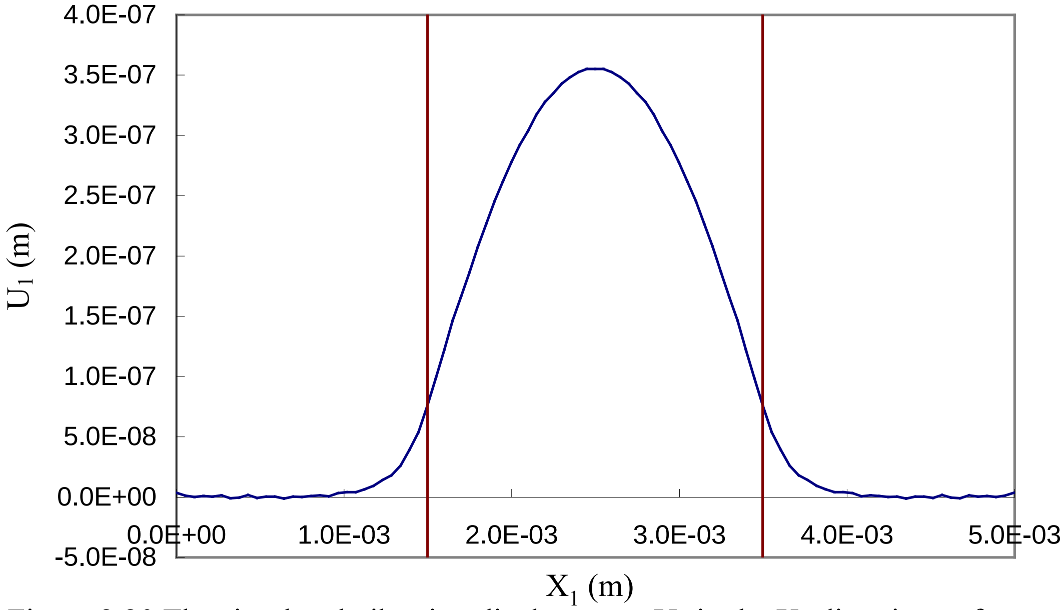

Figure 2.20 The simulated vibration displacement U_1 in the X_1 direction at f_{111} along the scanned line for the quartz resonator with an electrode of length 2 mm, width 1.2 mm and thickness 0.2 μm. The two vertical lines at X_1 = 1.5 mm and X_1 = 3.5 mm indicate the position of the electrode.

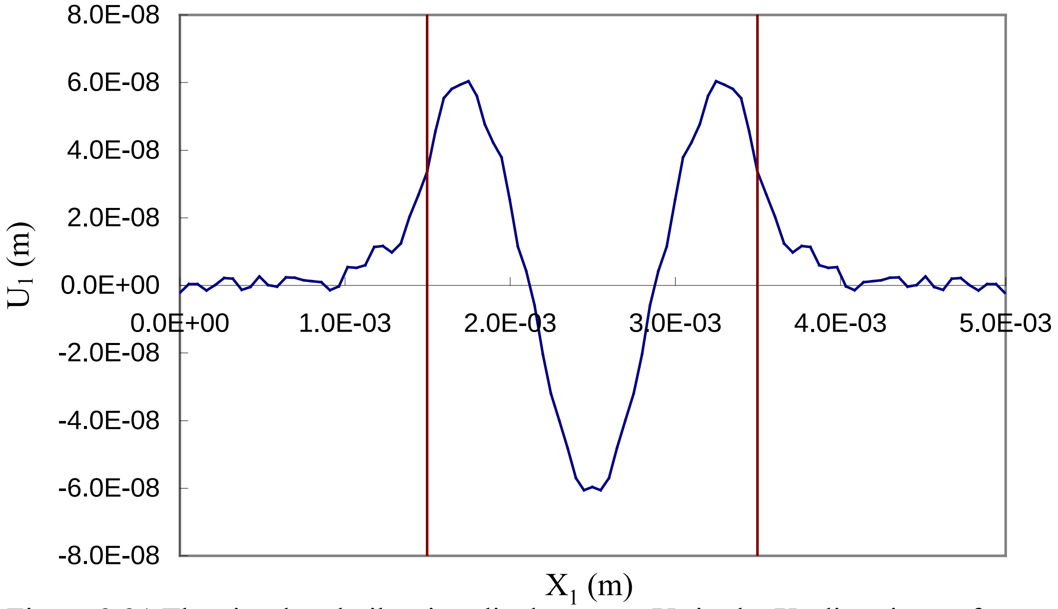

Figure 2.21 The simulated vibration displacement U_1 in the X_1 direction at f_{131} along the scanned line for the quartz resonator with an electrode of length 2 mm, width 1.2 mm and thickness 0.2 μm. The two vertical lines at X_1 = 1.5 mm and X_1 = 3.5 mm indicate the position of the electrode.

As shown in Figure 2.19, after the use of a "small" electrode, the fundamental and inharmonic thickness-shear mode resonances shift to higher frequencies and the flexural mode resonance adjacent to them disappears (or moves to higher frequencies). This should be caused by the effective trapping of the vibration in the electroded region as shown in Figures. 2.20 and 2.21. As the vibration is trapped in the electroded region, the corresponding "effective" length for the resonances becomes smaller as compared to the case for the resonator with full electrodes; and hence, the resonance frequency increases. This also implies that, unlike the cases for the 4-MHz resonators, the resonance frequencies should depend more strongly on the electrode length, which will be discussed in more details in the following section. The high energy trapping efficiency should be due to the large difference in the cutoff frequencies in the electroded and unelectroded regions as well as the high frequency of the vibration (~ 27 MHz).

As the cutoff frequency in the unelectroded region is larger than that in the electroded region (which is the fundamental thickness-shear mode resonance frequency), the flexural mode vibration shown in Figure 2.16 cannot propagate freely in the unelectroded region, and hence the corresponding resonance does not exist. It should be noted there may exist flexural mode resonances at higher frequencies corresponding to the vibration in the electroded region.

As discussed in the cases for the 4-MHz resonators, since there is no mechanical loss assumed for the quartz plate, the corresponding resonance peak is very sharp, and the impedance at f_{111} will decrease if the frequency step used in the simulation decreases. In fact, if the frequency step is sufficiently small, the impedance at f_{111} should be close to zero. This indicates that there is no physical meaning in considering the value for the case where no energy loss is considered.

Similar simulation results have also been observed for the vibration along a scanned line in the width direction (i.e. a scanned line normal to the one shown in Fig. 2.18). That is, the vibration is trapped in the electroded region, without spreading to the side edges of the quartz plate, and the resonance frequencies should depend more strongly on the width of the electrode as compared to the cases for the 4-MHz resonators.

Effects of Silver Epoxy

In this section, the effect of silver epoxy on the resonance responses is studied. For the commercial resonators (27 MHz), the quartz plate is held at two corners by the silver epoxy. Correspondingly, silver epoxy is added to the resonator model as shown in Figure 2.22 for the simulation. The two corners at the same end of the quartz plate are embedded in the silver epoxy of which the length l" is 0.8 mm, the width w" is 0.772 mm and the thickness is 0.06025 mm. The lossy characteristics of the silver epoxy is modelled by a damping factor of 1×10^{-7} in ANSYS. As mentioned before, the damping factor is determined by simulating impedance spectra with different damping factors, and compared the simulated impedance at resonance with the measured one. As the type of silver epoxy used in the 27-MHz resonator is different from that used in the 4-MHz resonator, the damping factor for the simulation of 27-MHz resonator (1×10^{-7}) is different from that used in the simulation of 4-MHz resonator (1×10^{-8}). The dimensions for the resonator and electrodes are the same as those for Figure 2.18. The impedance spectrum for the resonator has been simulated and compared with that for the resonator without silver epoxy (i.e. Fig. 2.18).

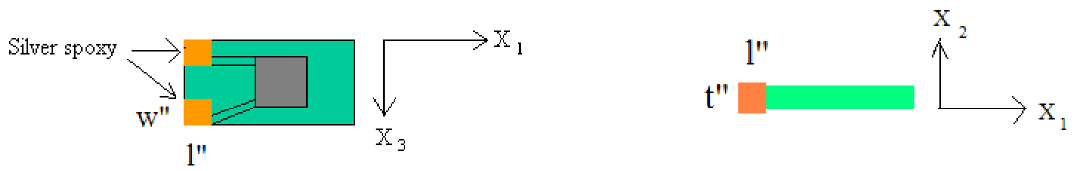

Figure 2.22 The configuration for the 27-MHz quartz resonator with the silver epoxy.

As shown in the previous section, the vibration is effectively trapped in the electroded region, the vibration in the unelectroded region, in particular at the ends of the quartz plate, is very small (Fig. 2.20). So, after the introduction of the lossy silver epoxy at the two corners, there is insignificant absorption of the vibration energy. Therefore, similar to the case for the resonator without silver epoxy, the simulated resonance peak associated with the fundamental thickness-shear mode is very sharp, and the corresponding impedance at f_{111} is close to zero if the frequency step used in the simulation is sufficiently small.

Although the vibration for the 27-MHz resonators is effectively trapped in the electroded region and hence there is insignificant energy absorption, it should be noted that if the silver epoxy is deposited on an area at which there is considerable vibration, the impedance at resonance will still increase because of the energy absorption. Figure 2.23 shows the simulated vibration displacements U_1 (the displacement in X_1 direction) at f_{111} along the scanned line (a line along X_1 direction at the center and top surface of the quartz plate) of the 27-MHz resonator with a "large" silver epoxy deposited at the two corners as shown in Figure 2.25. The simulated U_1 for the resonator with a "small" silver epoxy as shown in Figure 2.22 is also plotted in Figure 2.23 for comparison. It is clearly seen that as the silver epoxy is deposited in the region where the vibration is not small, the vibration is significantly damped, giving a high impedance at f_{111} about 90 Ω observed in the simulated impedance spectrum (Fig. 2.24). So it is of importance to determine the dimension and position of the silver epoxy to be deposited on the resonators so that the vibration will not be absorbed.

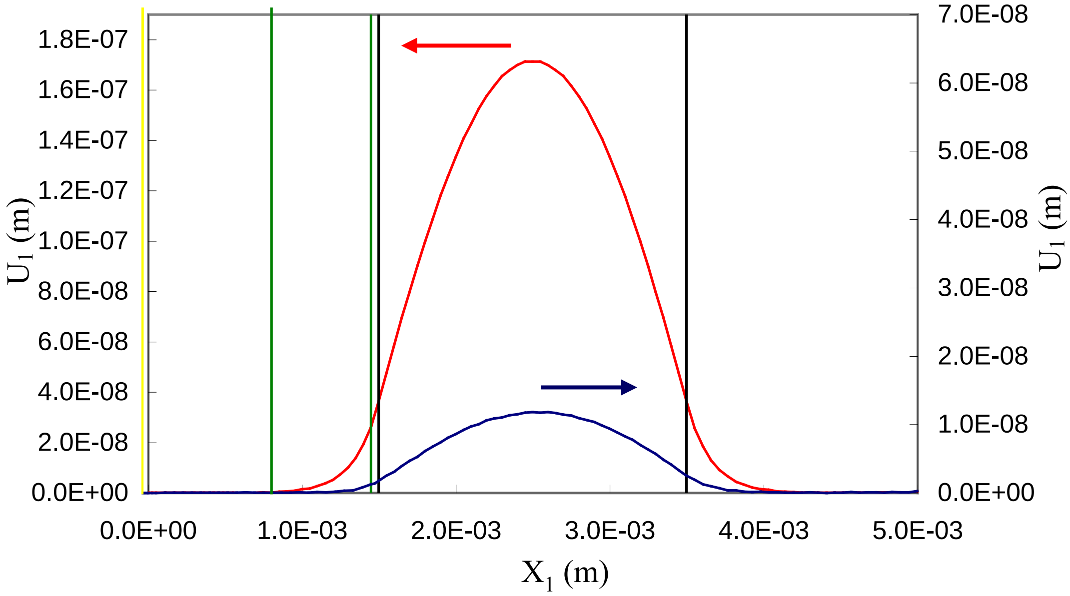

Figure 2.23 The simulated vibration displacement U_1 in the X_1 direction at f_{111} along the scanned line for the quartz resonators with different silver epoxies. The distribution in blue colour is for the resonator with a "large" silver epoxy, while that in red colour is for the resonator with a "small" silver epoxy. The two vertical black lines at X_1 = 1.5 mm and X_1 = 3.5 mm indicate the position of the electrode, while the vertical green lines at X_1 = 1.448 mm and X_1 = 0.8 mm indicate the position of the silver epoxy for the resonators.

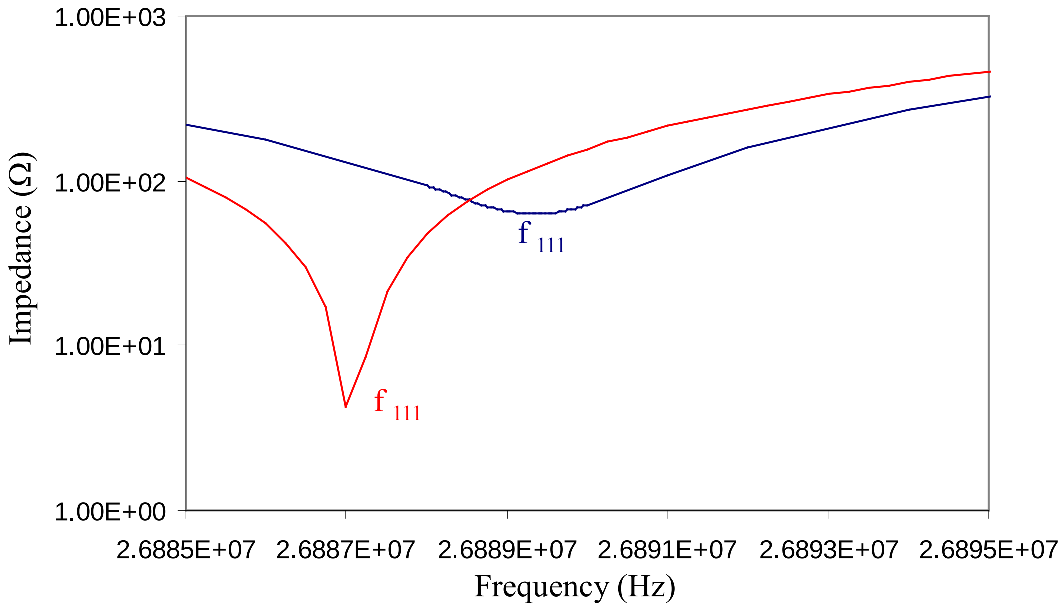

Figure 2.24 The simulated impedance spectrum around f_{111} for the quartz resonator with different silver epoxies. The simulated impedance spectrum in blue colour is for the resonator with a "large" silver epoxy, while that in red colour is for the resonator with a "small" silver epoxy.

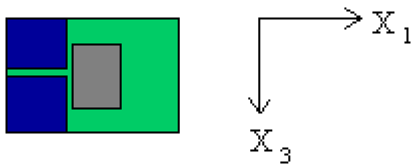

Figure 2.25 The configuration for the 27-MHz resonator with a "large" silver epoxy: l” = 1.448 mm and w” = 1.155 mm.

2.3 Experimental Observations of Resonance Responses

The simulation results in 2.2 have shown that there is a large difference in energy trapping efficiency between the 4-MHz and 27-MHz resonators. For the 4-MHz resonator, the vibration cannot be effectively trapped in the electroded region and spread over the whole quartz plate. As a result, the resonance frequencies depend only slightly on the length of the electrode, and the impedance at resonance increases because of the energy absorption by the silver epoxy which is deposited for holding of the quartz plate and electrically contact with peripheral electronics. Unlike the 4-MHz resonator, the vibration in the 27-MHz resonator is effectively trapped in the electroded region, and hence the resonance frequencies depend more strongly on the length of the electrode and the impedance at resonance remains small as there is insignificant energy absorption by the silver epoxy. In this section, both 4-MHz and 27-MHz resonators with electrodes of different lengths have been fabricated and their resonance responses, including the impedance spectrum and the vibration distribution, have been measured and compared with the simulation results.

2.3.1 Vibration Distribution

It has been observed that the impedance spectrum of a quartz resonator is very sensitive to the load applied on it. Figure 2.26 compares the impedance spectrum near the fundamental thickness-shear mode resonance f_{111} of the 4-MHz resonator with and without a load applied at the center of it. The illustrative distributions of the vibration displacement U_1 (the displacement in X_1 direction) at f_{111} for the 4-MHz resonator with and without a load applied at the centre are shown in Figure 2.27. It can be seen in Figure 2.27 that, subjected to the fixed load of 40 g, the "effective" vibration length is decreased, and thus f_{111} increases (Fig. 2.26). Also, subjected to the fixed load of 40 g, the magnitude of the resonance (the difference between the minimum and maximum impedances) decreases (Fig. 2.26). It is suggested that the load disturbs the vibration displacements of the quartz plate and hence the corresponding change of impedance and resonance frequency. Accordingly, the change is dependent on the vibration displacement at which the load is applied as well as the magnitude of the load. If the load is applied to a point where the vibration displacement is large, the disturbance induced (as compared to the original displacement) will be serious and hence the change will be significant.

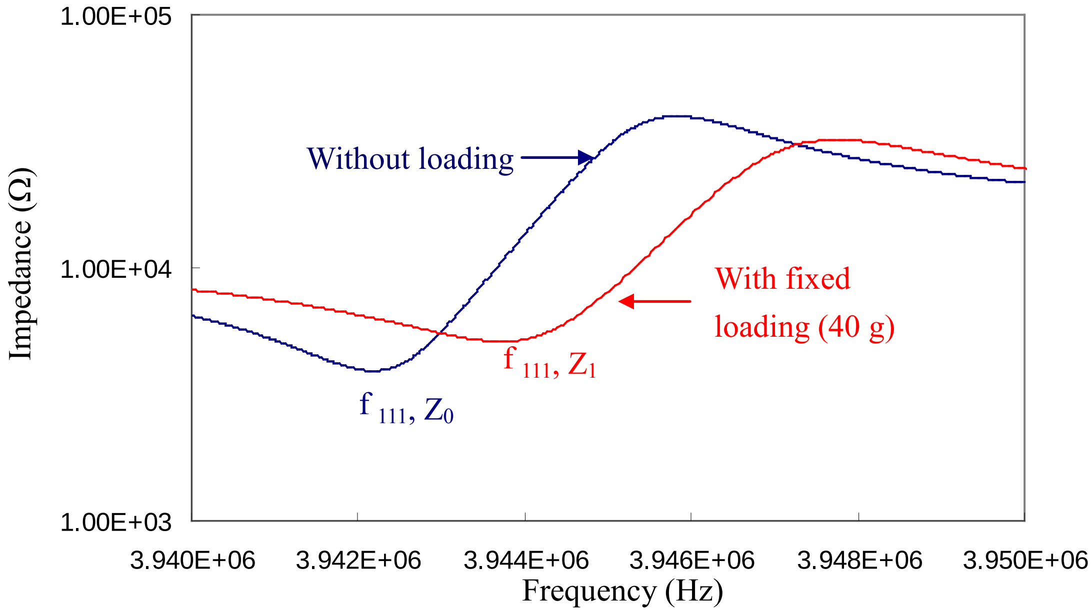

Figure 2.26 The impedance spectrum near the fundamental thickness-shear mode resonance of the 4-MHz resonator with and without a load applied at the center of it.

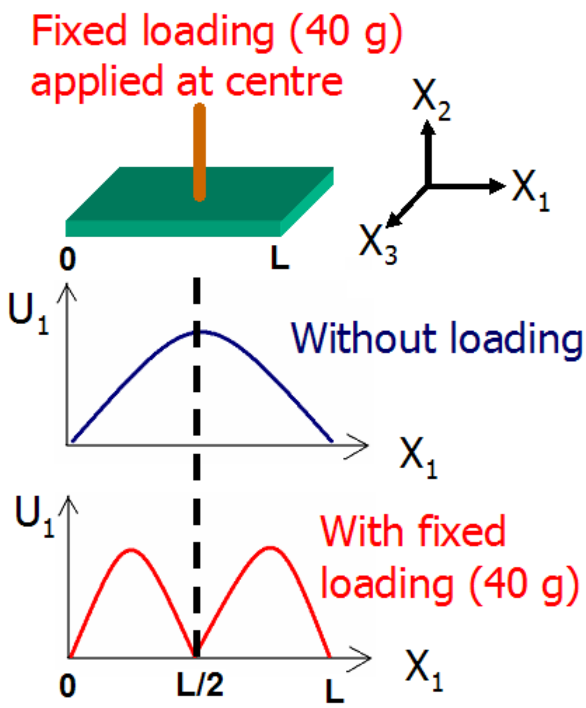

Figure 2.27 A fixed load of 40 g applied at the centre of the 4-MHz resonator. And the illustrative distributions of the vibration displacement U_1 in the X_1 direction at f_{111} for the 4-MHz resonator with and without a load applied at the centre of it.

Based on the idea, the vibration distribution of the resonators has been measured. The experimental setup for the measurement is shown in Figures 2.28 and 2.29, while a principle schematic diagram of the measurement is shown in Figure 2.30. The impedance spectrum near the fundamental thickness-shear mode resonance of the resonator is first measured using an impedance analyzer (Agilent 4294A), and from which the impedance at minimum (i.e. at resonance frequency) is determined (named as Z_o) (Fig. 2.26). Then a fixed load of 40 g (through a probe) is applied at a point on the scanned line (refer to Figs. 2.8 and 2.18) of the resonator and the impedance at minimum (i.e. at the new resonance frequency) is determined (named as Z_1) (Fig. 2.26). The change in impedance at minimum due to the loading is calculated as (Z_1 - Z_o), which is related to the original vibration displacement at the point where the load is applied. The procedure is repeated by applying the fixed load (40 g) at different points along the scanned line, and a distribution in vibration displacement is then obtained. Similar principle has been applied by Cumpson et al. [*Cumpson, 1990*] in measuring the vibration displacement of a quartz plate. In their work, a few drops of ink were deposited on the quartz surface to disturb the vibration.

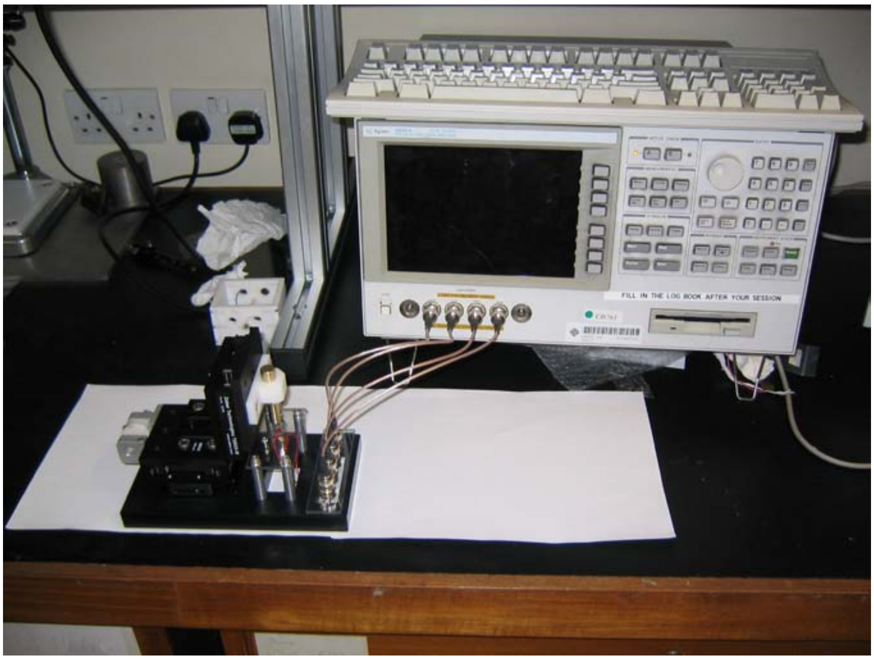

Figure 2.28 Experimental setup for the measurement of the vibration displacement of quartz resonators.

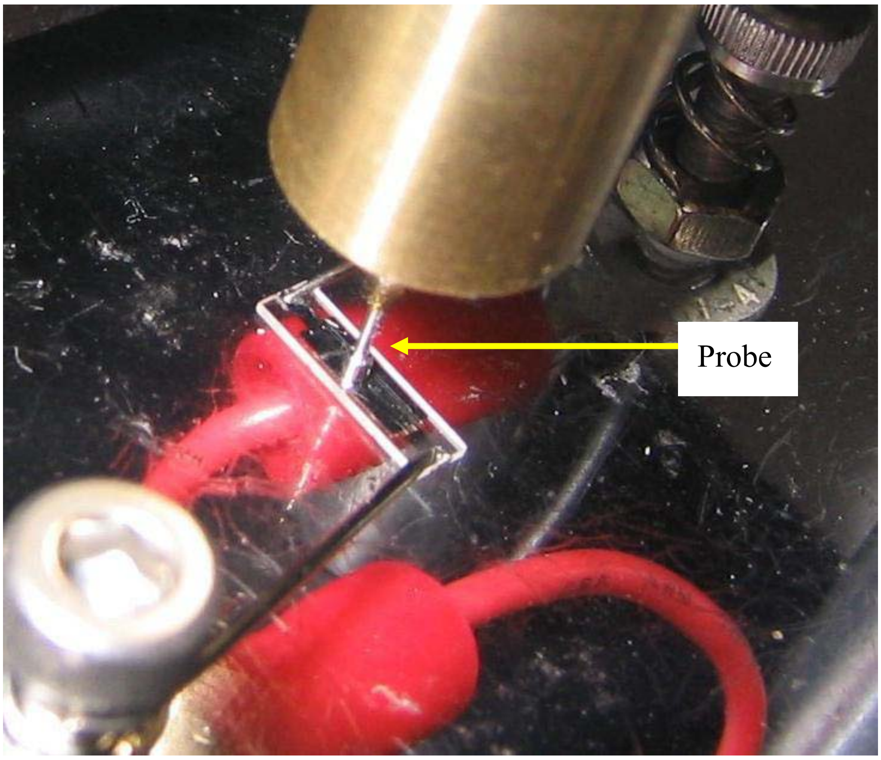

Figure 2.29 The probe used to apply a load on the quartz resonators.

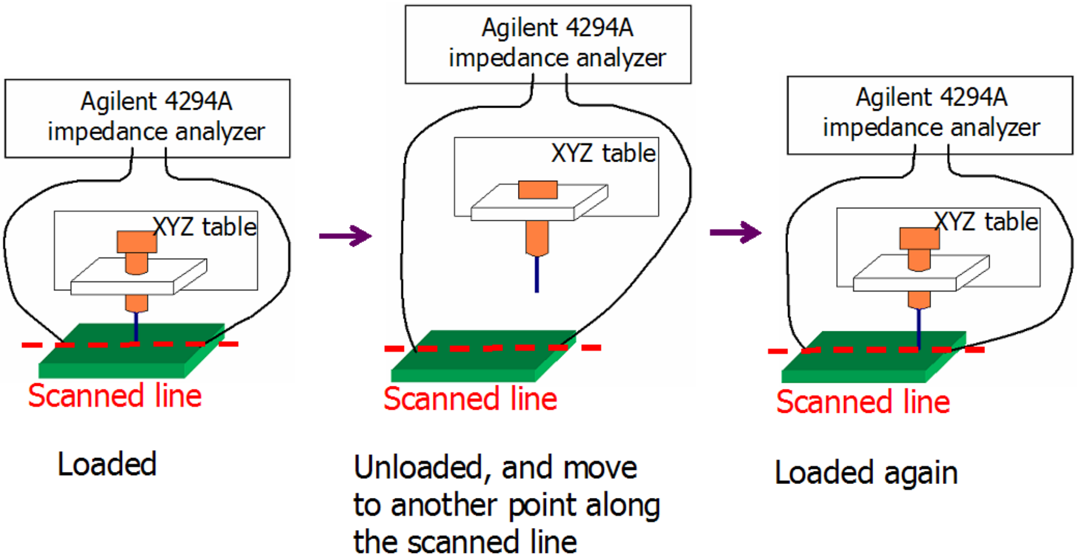

Figure 2.30 A principle schematic diagram of the measurement.

Following the procedures described above, the (normalized) distribution of vibration displacement (along the scanned line) for the 4-MHz resonator (Fig. 2.8) and 27-MHz resonator (Fig. 2.18) have been measured and shown in Figures 2.31 and 2.32, respectively. The simulation results for both the resonators are also shown in the figures for comparison. It can be seen that the experimental results agree very well with the simulation results for both cases. As it is very difficult to align the samples so as to have the measurements along a line perfectly parallel to the length of the electrode, there exists a small discrepancy between the experimental and simulated results, in particular for the 4-MHz resonator. Nevertheless, the good agreement suggests that the finite element analysis is a helpful tool in predicting the resonance responses of a resonator.

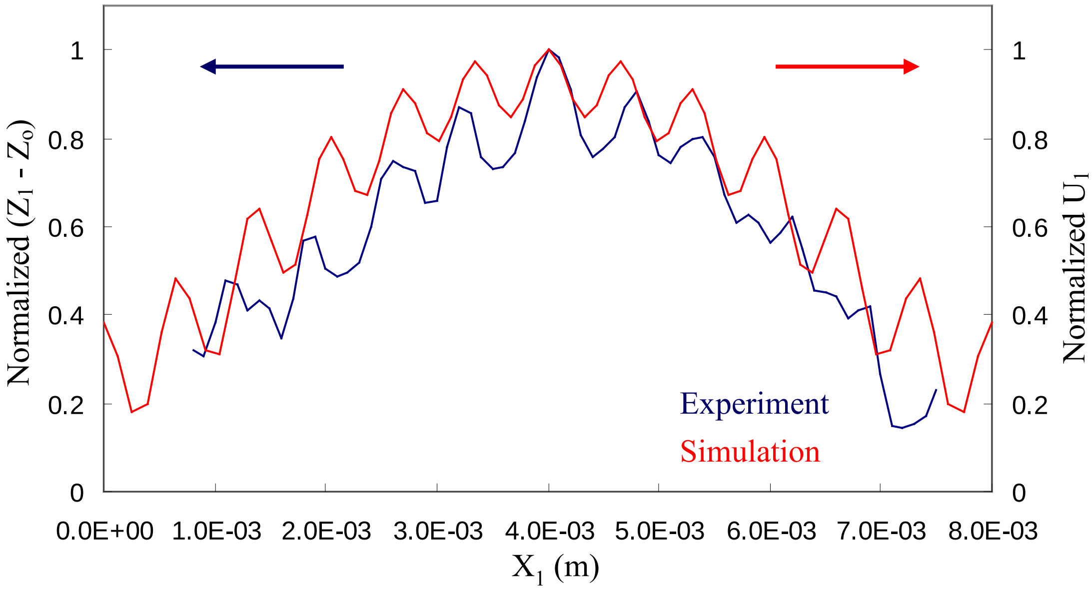

Figure 2.31 Normalized distribution of vibration displacement for the 4-MHz resonator.

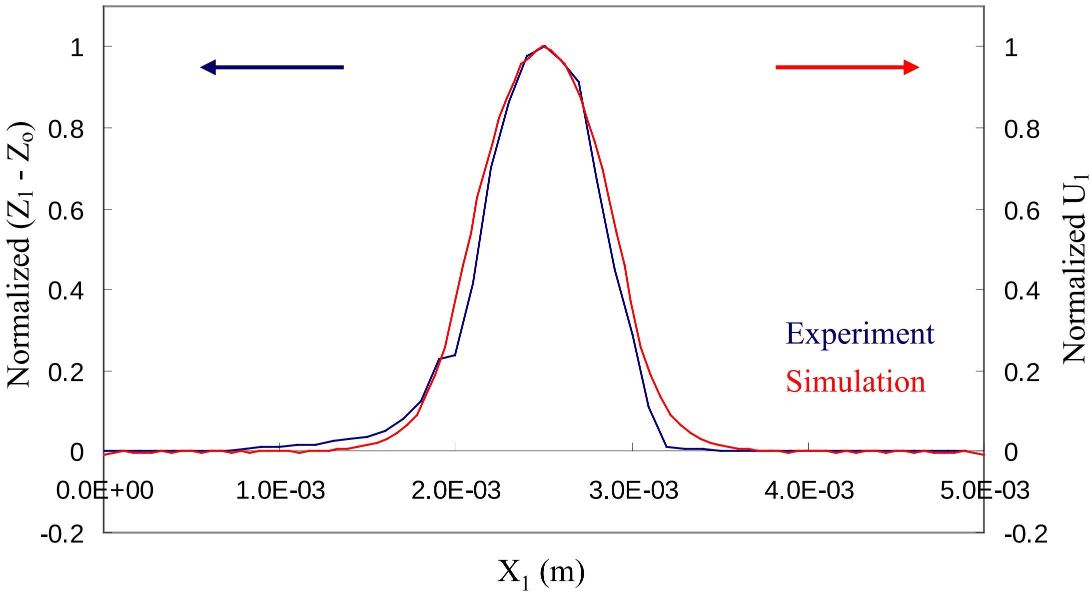

Figure 2.32 Normalized distribution of vibration displacement for the 27-MHz resonator.

Next, the dependence of the resonance frequency on the electrode length for both the 4-MHz and 27-MHz resonators are examined experimentally and compared with the simulation results. For both cases, resonators with electrode of different lengths have been fabricated and their resonance frequency for the fundamental thickness-shear mode has been determined using an impedance analyzer (Agilent 4294 A). Besides the electrode length, all the dimensions and configuration of the quartz plates and electrodes are the same as those shown in Figures 2.8 and 2.18, respectively. It should be noted all the resonators are well packaged as a commercial product, so there are silver epoxies holding the quartz plate and electrically connecting them to the experimental setup. However, as the deposition process is not precisely controlled, the dimensions of the silver epoxies are not the same as those used for the simulation.

The observed and simulated f_{111} (normalized) for the 4-MHz and 27-MHz resonators are compared in Figures 2.33 and 2.34, respectively. It can be seen that good agreement between the experimental and simulation results is obtained for both the resonators. This further confirms that for the 4-MHz resonators, due to the ineffective trapping of the vibration in the electroded region, the resonance frequency has only a weak dependence on the electrode length. On the other hand, due to the effective trapping of the vibration in the electroded region for the 27-MHz resonator, there exists a relatively strong dependence of the resonance frequency on the electrode length. Besides, the good agreement also suggests that the finite element analysis is a helpful tool in predicting and understanding the resonance responses of a resonator.

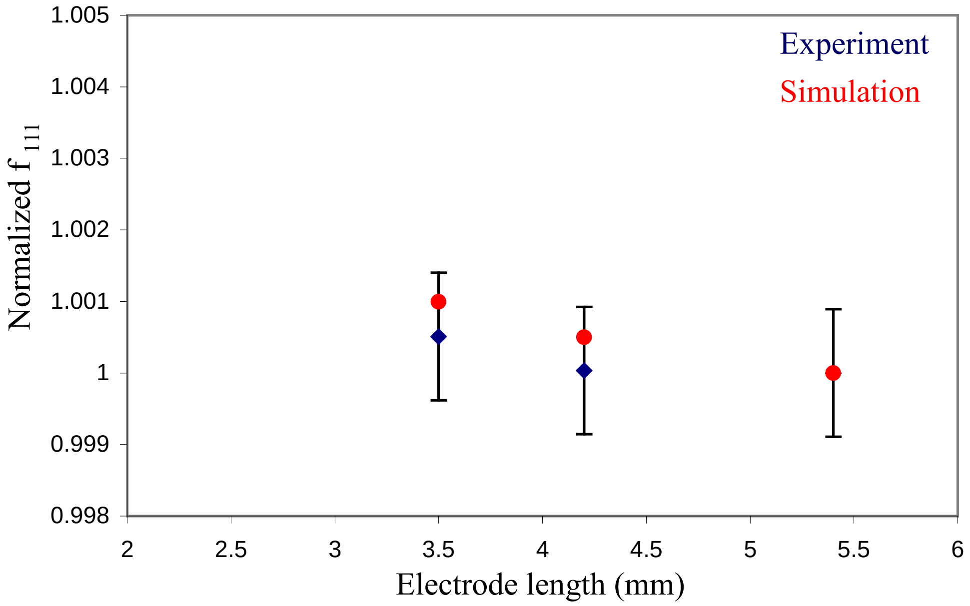

Figure 2.33 Comparison of the experimental and simulated f_{111} (normalized) for the 4-MHz resonator with different electrode lengths.

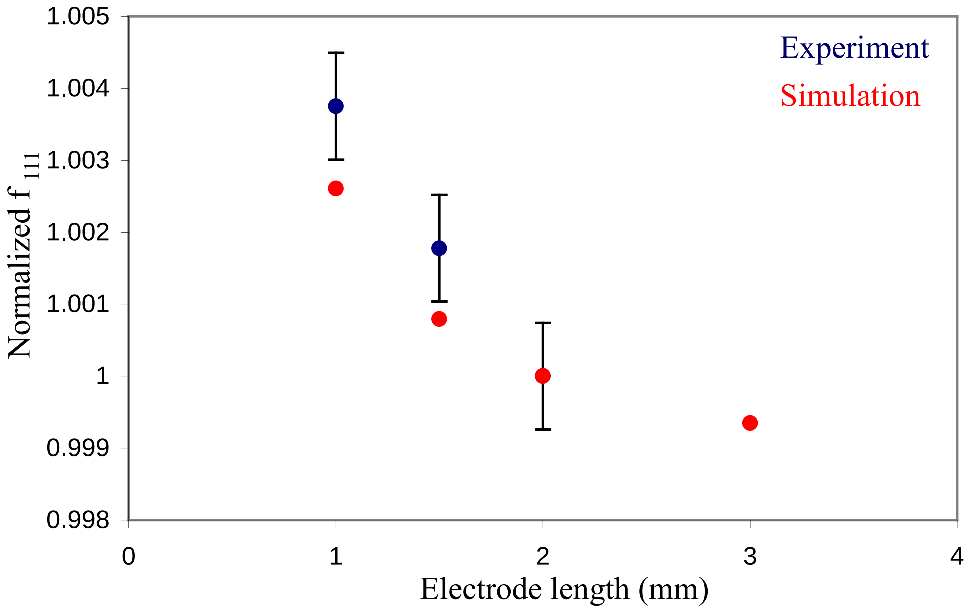

Figure 2.34 Comparison of the experimental and simulated f_{111} (normalized) for the 27-MHz resonator with different electrode lengths.

Chapter Three
Design, Fabrication, and Characterization of Third-overtone Resonators

3.1 Idea of Third-overtone Resonators

In Chapter 2, the resonance responses of the fundamental thickness-shear mode resonators are studied. On the basis of these results, third-overtone thickness-shear resonators are designed and fabricated. The third-overtone resonators are designed in the present work since they are thicker (about three times) than the fundamental-mode resonators with similar operating frequency. This will make the fabrication easier and the yield strength higher.

The third-overtone resonator is the resonator with the impedance at its third-overtone resonance frequency much smaller than that at its fundamental resonance frequency. So, in operation, the third-overtone resonance will be excited instead of the fundamental resonance, without the use of additional peripheral electronics. This can be done by suppressing the fundamental thickness-shear mode vibration.

It is known in the energy trapping theory that the energy trapping efficiency increases with the order of the harmonic overtones [*Hirama, 2000*]. That is, the energy trapping efficiency for the third-overtone thickness-shear mode is higher than that for the fundamental thickness-shear mode. This phenomenon can also be demonstrated by the FEM simulation. The resonator with the electrode of smaller size than the quartz plate as shown in Figure 3.1 is considered. The dimensions of the quartz plate and the main electrodes are

Quartz plate: l = 5 mm, w = 2.51 mm, t = 0.085 mm

Main electrode: l' = 1.83 mm, w' = 1.83 mm, t' = 0.2 μm

where l and l' are the dimensions along the X_1 direction, w and w' are the dimensions along the X_3 direction, and t and t' are the dimensions along the X_2 direction.

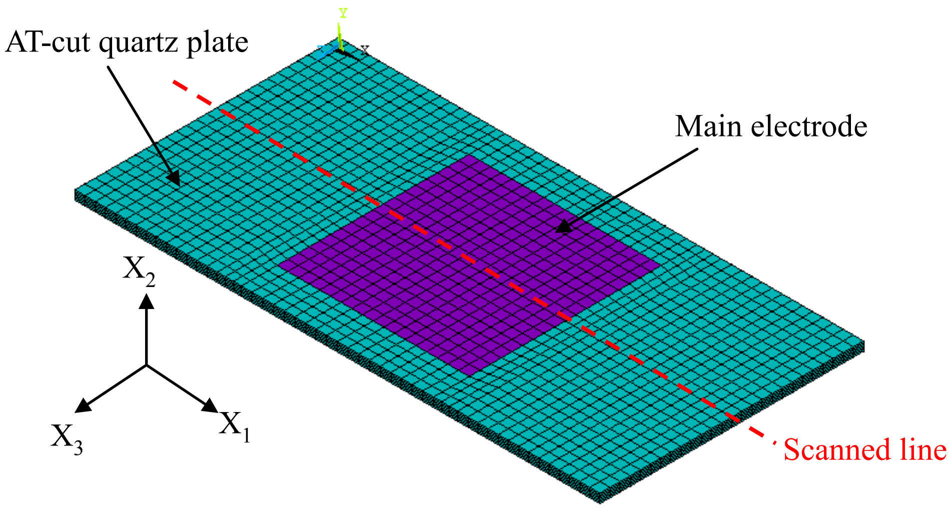

Figure 3.1 The resonator with the electrode at the centre of the quartz plate.

The vibration displacements for the fundamental and third-overtone thickness-shear modes of the resonator are simulated with the assumptions that there are no electrical and mechanical losses and no clamping to the quartz plate. The simulated vibration displacements U_1 (the displacement in the X_1 direction) along the scanned line (a line along the X_1 direction at the centre and top surface of the quartz plate as shown in Fig. 3.1) are shown in Figure 3.2.

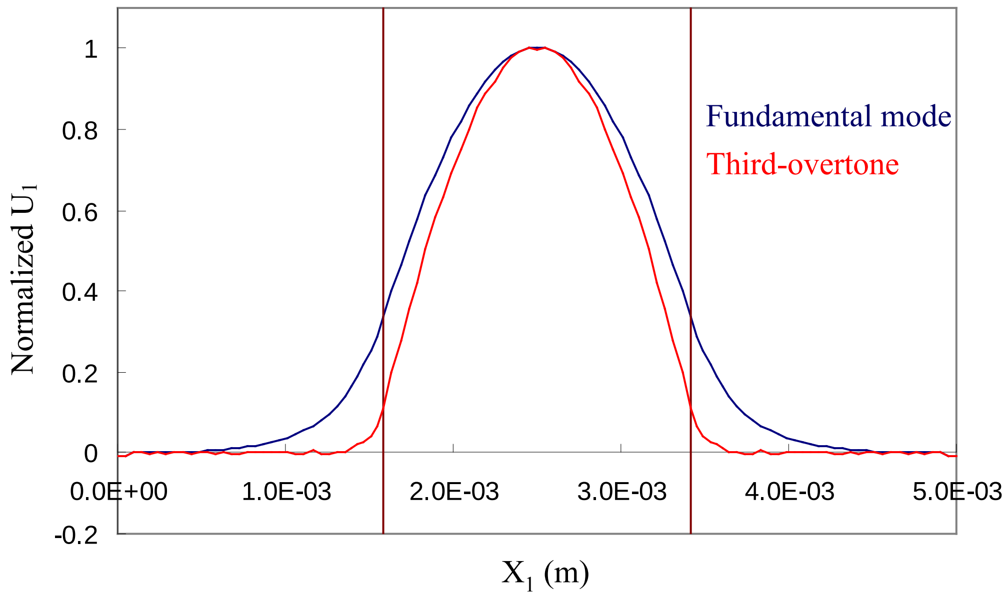

Figure 3.2 The simulated vibration displacements U_1 at the top surface of the AT-cut quartz plate (along the scanned line) for the fundamental and third-overtone thickness-shear modes. The two vertical lines at X_1 = 1.585 mm and X_1 = 3.415 mm indicate the position of the electrode.

Figure 3.2 shows that the vibration for the third-overtone thickness-shear mode is more effectively trapped in the electroded region than that for the fundamental thickness-shear mode. In other words, the energy trapping efficiency for the third-overtone thickness-shear mode is higher than that for the fundamental thickness-shear mode.

It has been shown in Chapter 2 that the impedance at resonance will increase if the vibration energy is absorbed by the silver epoxy deposited at the ends of the quartz plate; in other words, the corresponding vibration mode is suppressed. Therefore, it is believed that if silver epoxy is applied to a region in which the vibration for the fundamental thickness-shear mode is large while that for the third-overtone is negligibly small, only the vibration energy for the fundamental mode will be absorbed and the corresponding impedance at resonance will increase. As a result, the fundamental thickness-shear vibration mode is suppressed while there is no significant effect on the third-overtone mode. However, for a resonator with normal electrode configuration (as the one shown in Fig. 3.1), the difference in energy trapping efficiency is not large enough (as shown in Fig. 3.2) to ensure that there is only suppression of the fundamental mode vibration and no effect on the third-overtone mode. So it is necessary to develop methods for increasing the fundamental-mode vibration in the "unelectroded" region (or the region at which silver epoxy will be applied) while maintaining the third-overtone vibration as small as possible. This can be done by the introduction of sub-electrodes at the ends of the resonator as shown in Figure 3.3.

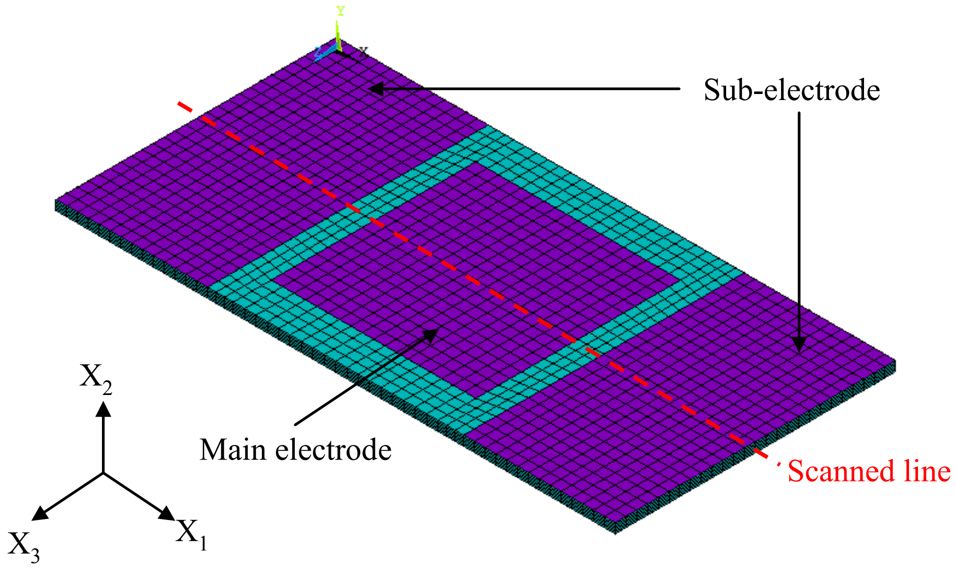

Figure 3.3 The third-overtone thickness-shear resonator with sub-electrodes at the ends of the resonator.

The dimensions of the quartz plate and the main electrode are the same as those of the resonator shown in Figure 3.1. The dimensions of the sub-electrodes are:

$$l'' = 1.355 \text{ mm}, w'' = 2.51 \text{ mm}, t'' = 0.2 \ \mu\text{m}$$

where l" is the dimension along the X_1 direction, w" is the dimension along the X_3 direction, and t" is the dimension along the X_2 direction. For the ease of the connection with the peripheral electronics, the electric potential applied to one side of the sub-electrode is the same as that of the top main electrode, while the electric potential applied to the other side of the sub-electrode is the same as that of the bottom main electrode as shown in Figure 3.4.

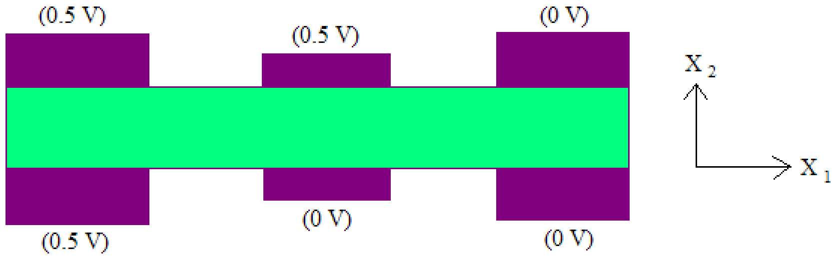

Figure 3.4 Cross-section of the third-overtone resonator. The thickness of the main and sub- electrodes are exaggerated.

The FEM simulation is performed with the assumptions that there are no electrical and mechanical losses and no clamping to the quartz plate. Figure 3.5a compares the simulated vibration displacements U_1 (the displacement in the X_1 direction) at the fundamental thickness-shear mode resonance for the resonators with and without the sub-electrodes (i.e. the resonators shown in Figs. 3.3 and 3.1, respectively) along the scanned line (refer to Figs. 3.1 and Fig. 3.3), while Figure 3.5b shows the simulated vibration displacement U_2 (the displacement in the X_2 direction) at the fundamental thickness-shear mode resonance for the resonator with the sub-electrodes (i.e. the resonator shown in Fig. 3.3) along the scanned line (refer to Fig. 3.3).

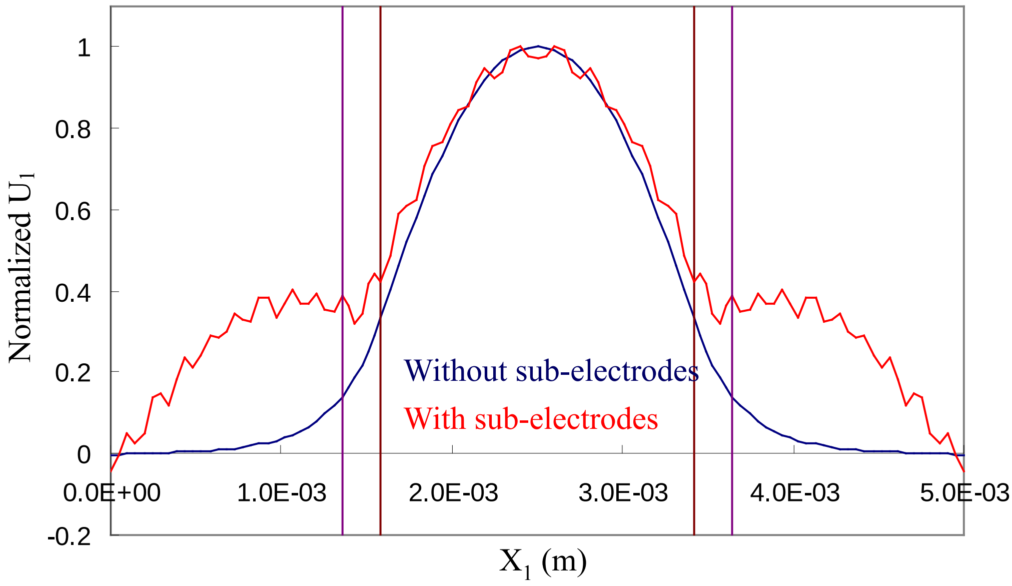

(a)

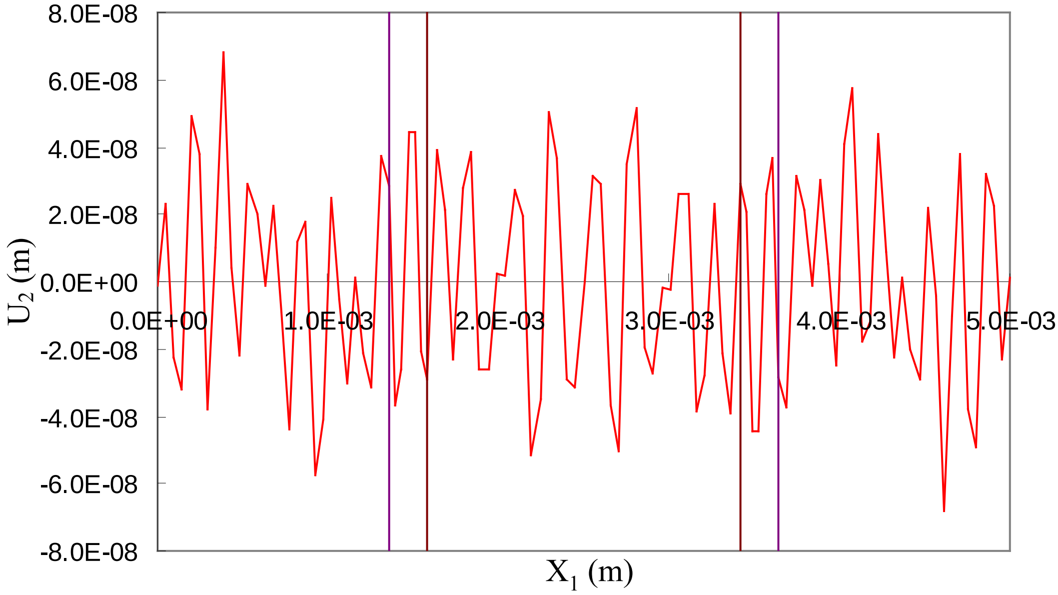

(b)

Figure 3.5 (a) The simulated vibration displacements U_1 at the fundamental thickness-shear mode resonance at the top surface of the AT-cut quartz plate (along the scanned line) with and without sub-electrodes. (b) The simulated vibration displacement U_2 at the fundamental thickness-shear mode resonance at the top surface of the AT-cut quartz plate (along the scanned line) with sub-electrodes. The two vertical brown lines at X_1 = 1.585 mm and X_1 = 3.415 mm indicate the position of the main electrode, while the two vertical purple lines at X_1 = 1.355 mm and X_1 = 3.645 mm indicate the position of the sub-electrodes.

It can be seen that the vibration for the resonator without the sub-electrodes is not very effectively trapped in the main-electroded region; the vibration "leaks" from the main-electroded region and becomes almost zero at the ends of the quartz plate. However, after the introduction of the sub-electrodes, the vibration spreads over almost the whole quartz plate and has quite a large amplitude in the sub-electroded region. It is also noticed that as the vibration spreads over the whole quartz plate, the flexural-mode vibration (where the dominant vibration displacement is in the X_2 direction) is initiated and becomes coupled into the thickness-shear mode vibration (where the dominant vibration displacement is in the X_1 direction), as shown in Figure 3.5a. Thus, the simulated vibration displacements at the fundamental thickness-shear mode resonance along the scanned line for the resonator with the sub-electrodes (Fig. 3.3) exist in both the X_1 (U_1 as shown in Fig. 3.5a) and X_2 direction (U_2 as shown in Fig. 3.5b), and ripples exhibit in the simulated vibration displacement U_1 as shown in Figure 3.5a. After the addition of the sub-electrodes with a thickness equal to that of the main electrode, the cutoff frequency of the sub-electroded region ω_{se} will decrease and become the same as that of the main- electroded region ω_e. That is, $\omega_{se} = \omega_e < \omega_s$, where ω_s is the cutoff frequency for the unelectroded region. Therefore, for the fundamental thickness-shear mode with resonance frequency ω_{TS} satisfying $\omega_{se} = \omega_e < \omega_{TS} < \omega_s$, the wave vector for the wave propagation along the X_1 direction will change from imaginary to real after the introduction of the sub-electrodes [*Hirama, 2000*]. That is, from an exponentially decaying wave to a propagating wave. In other words, the introduction of the sub-electrodes can amplify the "leaked" vibration from the main-electroded region. The effect of the sub-electrodes on the third-overtone vibration will be discussed later.

The length of the sub-electrodes l” is another important parameter in increasing the “leaked” fundamental thickness-shear vibration. The simulated vibration displacement U_1 (along the scanned line) for a resonator with sub-electrodes of length 0.29 mm (and applied at the ends of the quartz plate) is shown in Figure 3.6, in which the vibration for the resonators with sub-electrodes of length 0 mm (i.e. without sub-electrode) and 1.355 mm (refer to Fig. 3.5a) are also plotted for comparison.

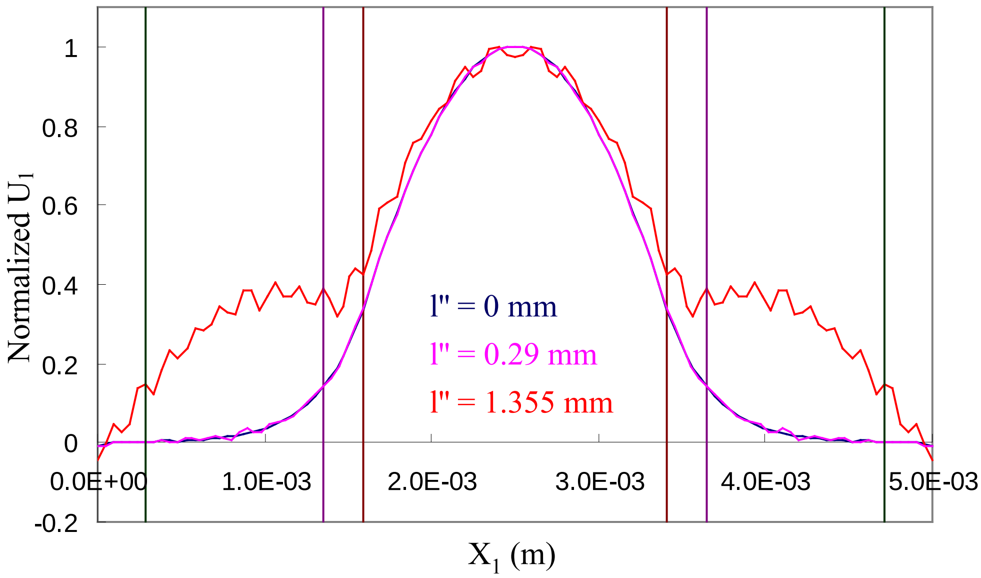

Figure 3.6 The simulated vibration displacements U_1 at the fundamental thickness-shear mode resonance at the top surface of the AT-cut quartz plate (along the scanned line) with sub-electrodes of different lengths. The two vertical brown lines at X_1 = 1.585 mm and X_1 = 3.415 mm indicate the position of the main electrode, while the two vertical green lines at X_1 = 0.29 mm and X_1 = 4.71 mm indicate the position of the sub-electrodes of length 0.29 mm and the two vertical purple lines at X_1 = 1.355 mm and X_1 = 3.645 mm indicate the position of the sub-electrodes of length 1.355 mm.

It can be seen that for the resonator with 0.29-mm sub-electrodes, the vibration distribution is almost the same as that for the resonator without the sub-electrodes. It is because the “leaked” vibration from the main-electroded region in the sub-electroded region is very small; there is almost no vibration to be amplified in the sub-electroded region. As a result, the vibration distribution remains almost the same as the one before the introduction of the sub-electrodes. Therefore, the sub-electrodes should be long enough to cover the "leaked" vibration with significant amplitude and thick enough to amplify the "leaked" vibration to considerable amplitude. In the mean time, the sub-electrodes should not amplify the vibration of the third-overtone resonance mode which should be effectively trapped in the main-electroded region. In the present work, we find that sub-electrodes of length 1.355 mm (and thickness 0.2 μm) can effectively amplify the "leaked" fundamental-mode vibration from the main-electroded region while there is almost no effect on the third-overtone vibration (which will be discussed below).

To effectively suppress the fundamental vibration mode, silver epoxy has to be applied at the ends of the resonator to absorb the corresponding vibration energy, as shown in Figure 3.7. The silver epoxy also serves as the electrical connection to the peripheral electronics in real applications. As silver epoxy is a lossy material, a damping factor should be determined in the FEM simulation. For the existing commercial resonators (4 MHz and 27 MHz), the lossy characteristics of the silver epoxy are modelled by damping factors of 1×10^{-8} and 1×10^{-7}, respectively. As silver epoxy are used to absorb the fundamental-mode vibration energy (i.e., to suppress the fundamental vibration mode) in the present work, the more lossy silver epoxy (used in the 27-MHz resonators) is used for the larger amount of the fundamental-mode vibration energy absorption, while keeping the third-overtone mode vibration energy absorption as small as possible. And thus, the damping factor of 1×10^{-7} is used in the FEM simulations. To simulate the actual situation (the resonator is fixed on a holder), the bottom of the silver epoxy is set to zero displacement. The simulated impedance spectrum near the fundamental thickness-shear resonance mode for the resonator (as shown in Figure 3.7) is shown in Figure 3.8. The simulated impedance spectrum for the resonator shown in Figure 3.3 (the resonator with the same dimensions and electrode configurations, but without silver epoxy) is also plotted in Figure 3.8 for comparison. The corresponding distributions of vibration displacement U_1 along the scanned line are shown in Figure 3.9.

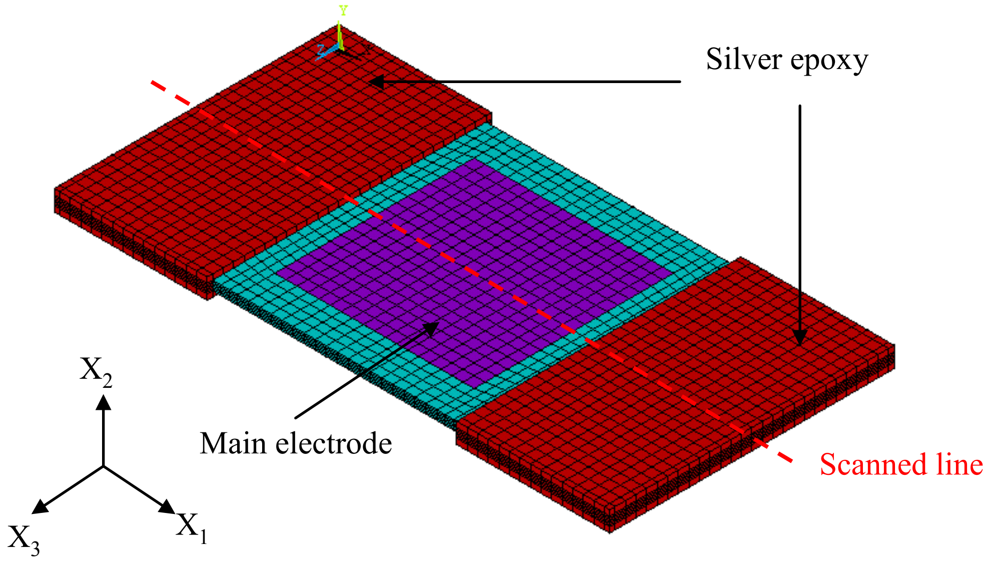

Figure 3.7 The third-overtone thickness-shear resonator with silver epoxy at the ends of the resonator.

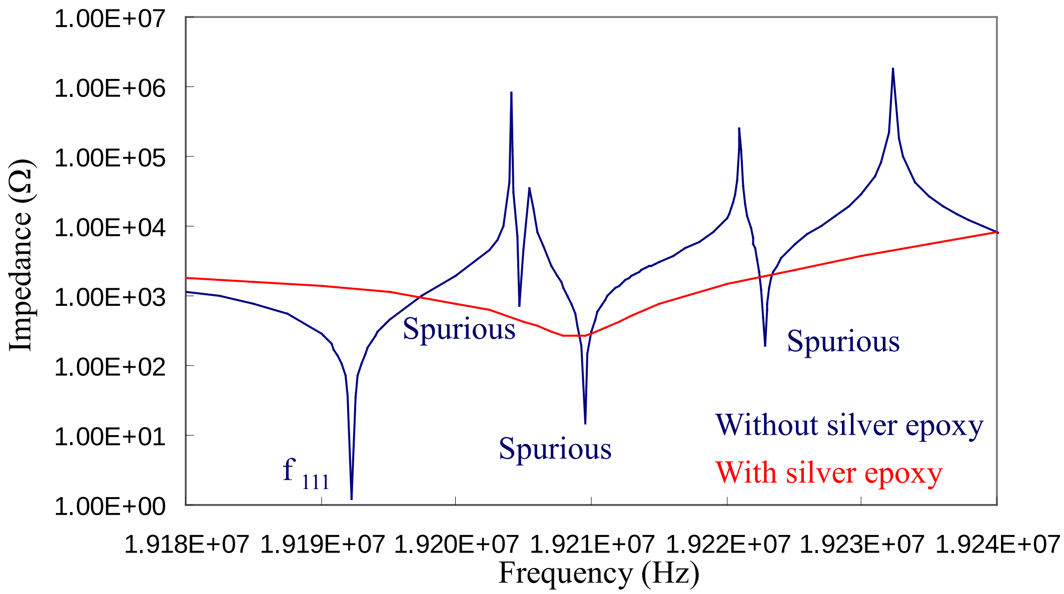

Figure 3.8 The simulated impedance spectrum around the fundamental thickness-shear resonances for the resonator with and without the silver epoxy.

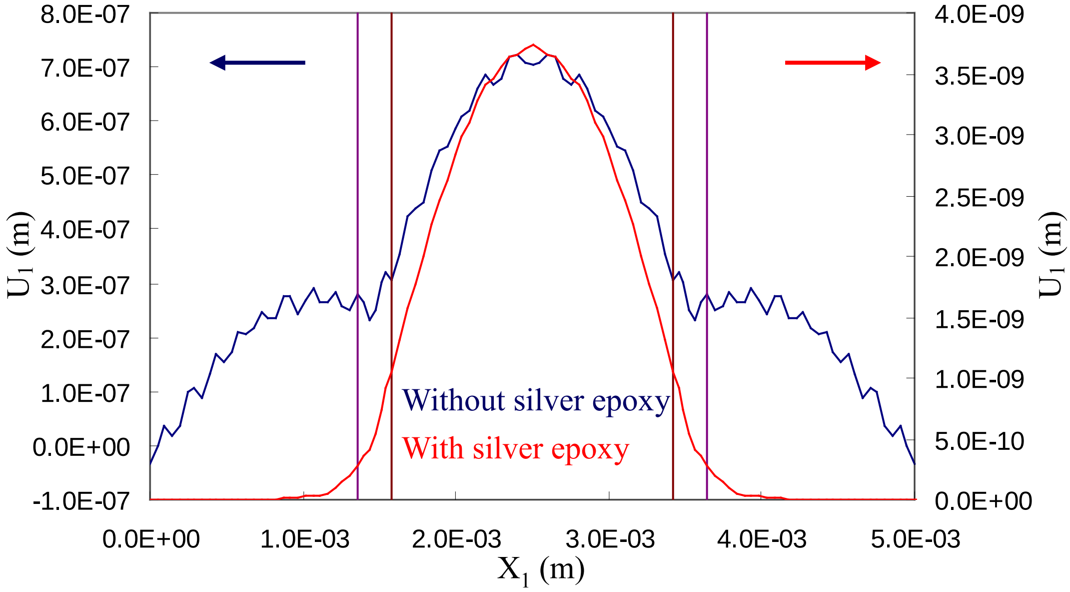

Figure 3.9 The simulated vibration displacements U_1 at the fundamental thickness-shear mode resonance at the top surface of the AT-cut quartz plate (along the scanned line) with and without the silver epoxy. The two vertical brown lines at X_1 = 1.585 mm and X_1 = 3.415 mm indicate the position of the main electrode, while the two vertical purple lines at X_1 = 1.355 mm and X_1 = 3.645 mm indicate the position of the sub-electrodes of length 1.355 mm.

As discussed in the previous section, after the introduction of the sub-electrodes, the thickness-shear mode vibration spreads over the whole quartz plate (Fig. 3.5a and Fig. 3.9); the flexural-mode vibration is thus initiated and becomes the spurious modes as shown in Figure 3.8. However, after the introduction of silver epoxy, the vibration energy for the thickness-shear mode resonance is greatly absorbed, leading to a high impedance value at the resonance frequency (~ 260 Ω). As shown in Figure 3.9, the vibration displacement is greatly decreased by about ten times. Besides, because of the decrease in the thickness-shear mode vibration, the flexural-mode vibration cannot be initiated, thus resulting in a "pure" thickness-shear resonance mode (Fig. 3.8). It is also noticed that the thickness-shear mode vibration becomes trapped under the main-electroded region.

Next, the effects of the sub-electrodes and the silver epoxy on the third-overtone thickness-shear mode vibration are discussed. Figure 3.10 compares the distributions of the vibration displacement U_1 at the third-overtone resonance mode (alone the scanned line) for the resonators with and without the sub-electrodes (i.e. the resonators shown in Figs. 3.3 and 3.1, respectively).

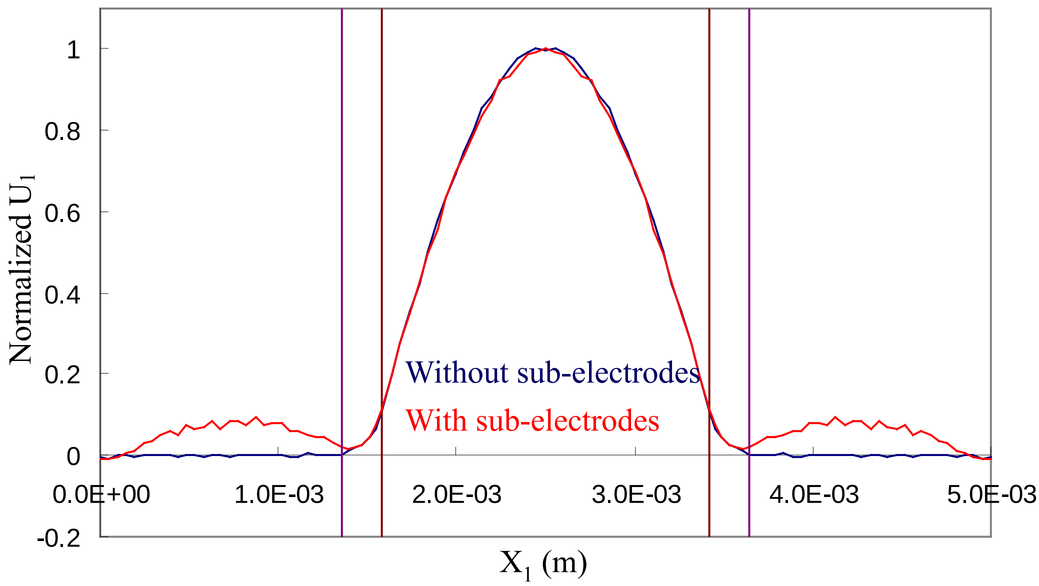

Figure 3.10 The simulated vibration displacements U_1 at the third-overtone thickness-shear mode resonance at the top surface of the AT-cut quartz plate (along the scanned line) with and without sub-electrodes. The two vertical brown lines at X_1 = 1.585 mm and X_1 = 3.415 mm indicate the position of the main electrode, while the two vertical purple lines at X_1 = 1.355 mm and X_1 = 3.645 mm indicate the position of the sub-electrodes of length 1.355 mm.

It can be seen that the vibration for the resonator without the sub-electrodes is effectively trapped in the main-electroded region. There is almost no "leaked" vibration from the main-electroded region. Hence, it is expected that there should be no significant change in the vibration distribution after the introduction of the sub-electrodes. However, it is interesting to note that vibration exists beyond the main-electroded regions for the resonator with the sub-electrodes, and the thickness-shear mode vibration is coupled by these vibrations. The simulated impedance spectrum for the resonator (with the sub-electrodes) is shown in Figure 3.11. It can be seen that a spurious mode occurs near the third-overtone resonance mode, which may be induced by the amplified vibration at low frequencies (Fig. 3.5a). The vibration displacement U_1 (along the scanned line) at that spurious mode is shown in Figure 3.12. It can be seen that the vibrations spread over the whole quartz plate. Hence it is suggested the third-overtone mode vibration is coupled by this spurious vibration, giving small vibration in the sub-electroded region.

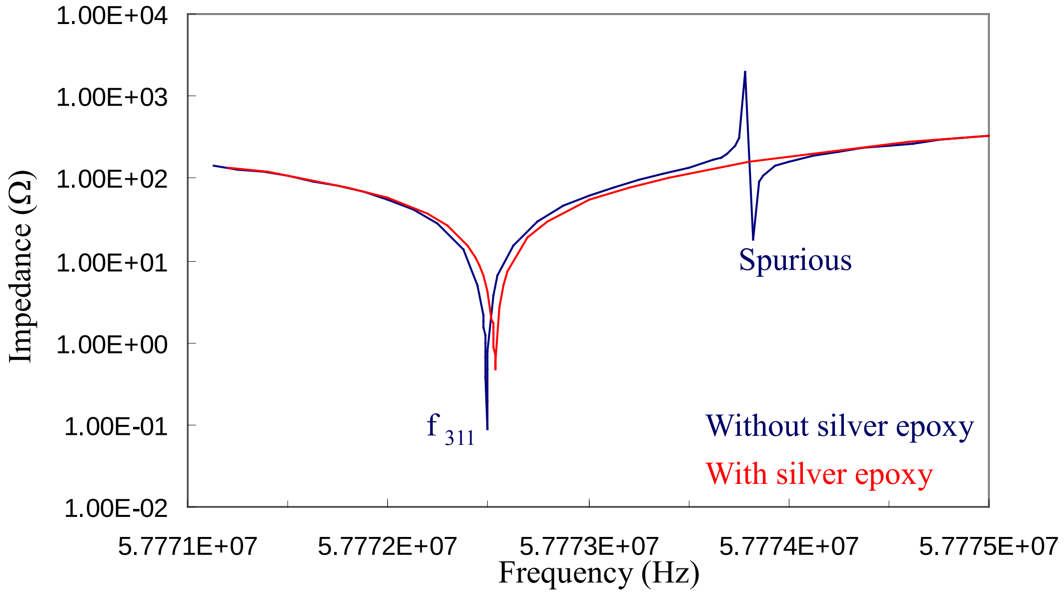

Figure 3.11 The simulated impedance spectrum around the third-overtone thickness-shear resonances for the resonator with and without the silver epoxy.

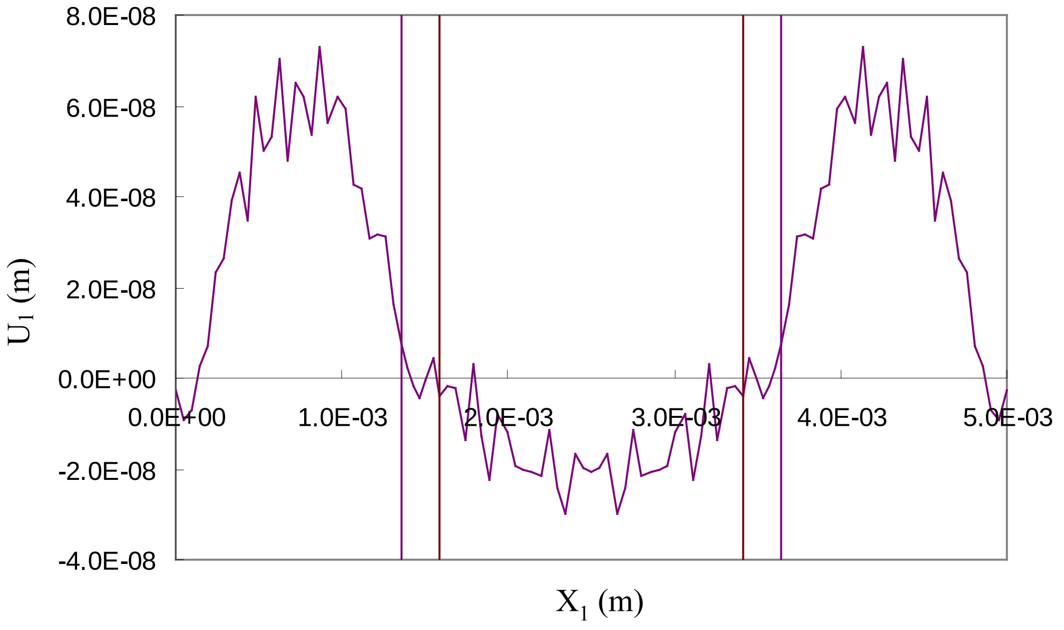

Figure 3.12 The simulated vibration displacements U_1 (along the scanned line) at the spurious mode resonance at the top surface of the AT-cut quartz plate (with sub-electrodes) without the silver epoxy. The two vertical brown lines at X_1 = 1.585 mm and X_1 = 3.415 mm indicate the position of the main electrode, while the two vertical purple lines at X_1 = 1.355 mm and X_1 = 3.645 mm indicate the position of the sub-electrodes of length 1.355 mm.

The effects of the silver epoxy on the third-overtone resonators (i.e. the resonator with the sub-electrodes as shown in Fig. 3.3) are also shown in Figures 3.11 and 3.13. After the introduction of silver epoxy on the sub-electrodes, the spurious mode vibrations are greatly damped (similar effects also shown in Fig. 3.9), leading to a "pure" third-overtone resonance mode (Fig. 3.11). Without the coupling of the spurious mode, the vibration displacement U_1 at the third-overtone resonance mode becomes regular and mainly trapped under the main-electrode (Fig. 3.13). As a result, the vibration energy is not absorbed by the silver epoxy, and thus the impedance value at the third-overtone resonance frequency remains very small (0.5 Ω).

As there is a large difference in the impedance values at the fundamental thickness-shear resonance mode and third-overtone resonance mode (260 Ω vs 0.5 Ω), the resonator (shown in Fig. 3.7) will resonate at its third-overtone resonance frequency, instead of its fundamental resonance frequency, in operation. In other words, the fundamental resonance mode is successfully suppressed and a third-overtone resonator is developed.

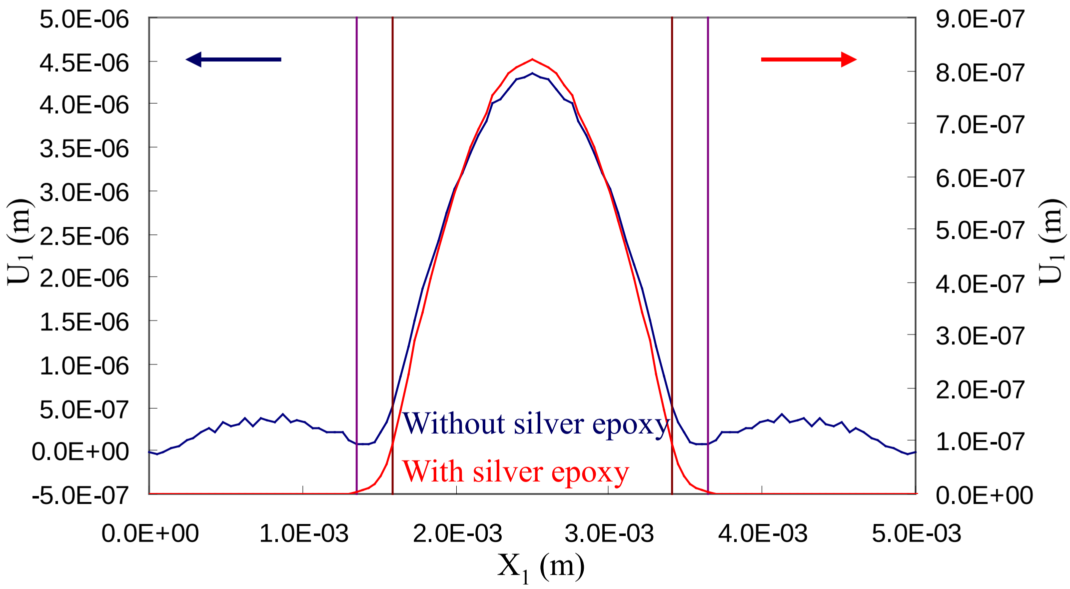

Figure 3.13 The simulated vibration displacements U_1 at the third-overtone thickness-shear mode resonance at the top surface of the AT-cut quartz plate (along the scanned line) with and without the silver epoxy. The two vertical brown lines at X_1 = 1.585 mm and X_1 = 3.415 mm indicate the position of the main electrode, while the two vertical purple lines at X_1 = 1.355 mm and X_1 = 3.645 mm indicate the position of the sub-electrodes of length 1.355 mm.

3.2 Effect of the size of Silver Epoxy

As shown in the previous section, the silver epoxy plays an important role in suppressing the fundamental resonance mode (through the absorption of the vibration energy). However, in the manufacturing process, the deposition process of the silver epoxy on the resonators is not very precisely controlled. As a result, the size of the silver epoxy may not be exactly the same as the one from the design. So, in this section, the effects of the size of the silver epoxy is discussed.

Figure 3.14 compares the distribution of the vibration displacement U_1 (along the scanned line) at the fundamental thickness-shear resonance mode for the resonators with silver epoxy of different l''' (dimensions along X_1): 0 mm (i.e. without silver epoxy), 1.065 mm and 1.355 mm. All the silver epoxies are applied to the ends of the quartz plate. As discussed in the previous section, the epoxy of l''' = 1.355 mm can effectively absorb the vibration energy for both the fundamental resonance mode and the spurious mode, and thus gives a clean fundamental resonance peak with a large impedance value (~ 260 Ω) at resonance frequency. It can be seen, from Figure 3.14, that the silver epoxy of length (l''' = 1.065 mm) can also effectively absorb the vibration energy for the fundamental resonance mode and the spurious mode, giving a clean resonance peak. However, as the energy absorption is not as high as the case with a larger silver epoxy, the impedance at the resonance frequency is lower, ~ 110 Ω. Nevertheless, the resulting difference between the impedance values at the fundamental and the third-overtone resonance modes is still large (~ 110 Ω vs 0.5 Ω), such that the resonator will resonate at its third-overtone resonance frequency, instead of the fundamental resonance frequency. The simulation results (Fig. 3.15) have shown that the use of a smaller silver epoxy (l''' = 1.065 mm) has no significant effect on the third-overtone resonance. On the basis of the above results, it can be concluded that in order to effectively suppress the fundamental resonance mode, the silver epoxy should cover at least two-third of the sub-electrodes.

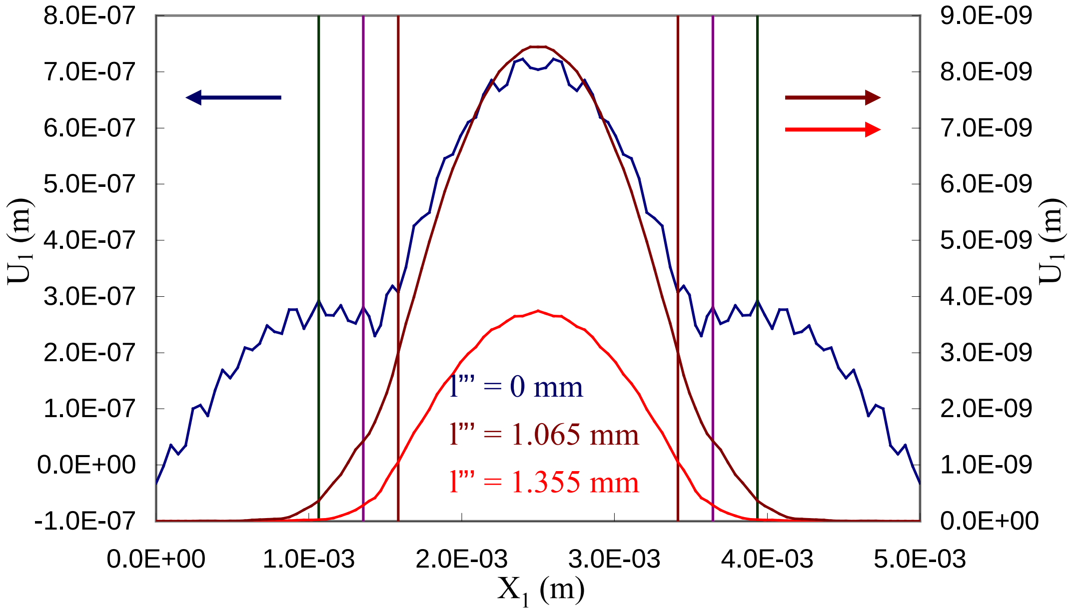

Figure 3.14 The simulated vibration displacements U_1 at the fundamental thickness-shear mode resonance at the top surface of the AT-cut quartz plate (along the scanned line) with silver epoxy of different dimensions along X_1. The two vertical brown lines at X_1 = 1.585 mm and X_1 = 3.415 mm indicate the position of the main electrode, while the two vertical purple lines at X_1 = 1.355 mm and X_1 = 3.645 mm indicate the position of the sub-electrodes of length 1.355 mm. The two vertical green lines at X_1 = 1.065 mm and X_1 = 3.935 mm indicate the position of the silver epoxy of length 1.065 mm.

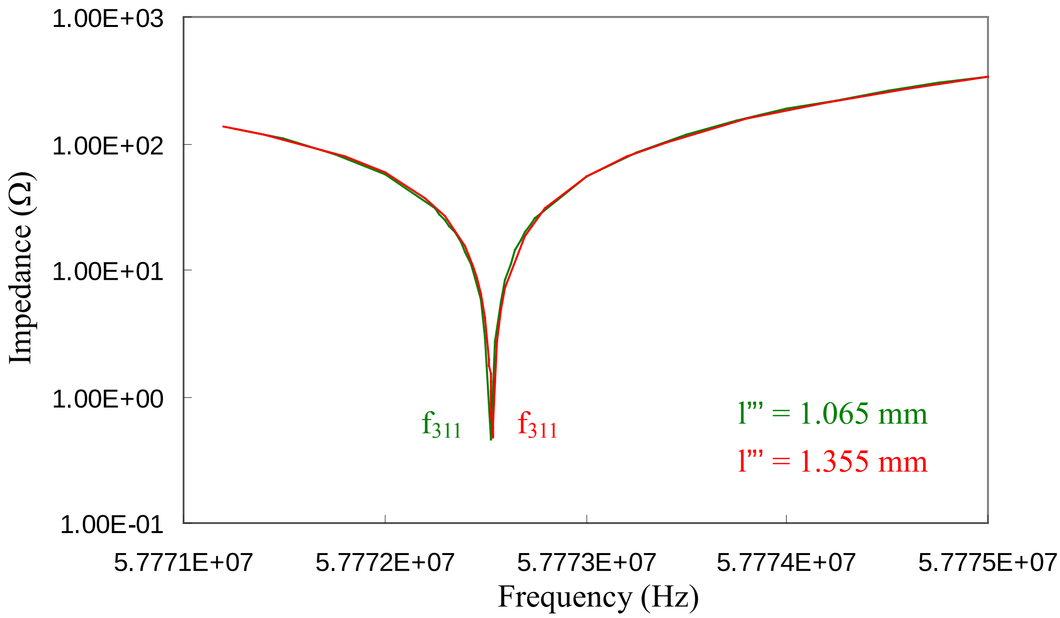

Figure 3.15 The simulated impedance spectrum around the third-overtone thickness-shear resonances for the resonator with silver epoxy of different dimensions along X_1.

In fact, the simulations (Fig. 3.16) have also shown that a thicker sub-electrode (i.e. 0.25 μm) can more effectively amplify the "leaked" fundamental-mode vibration in the sub-electroded region. If a silver epoxy of length equal to two-third of the sub-electrode is applied, the impedance at the fundamental mode resonance can be increased to about 230 Ω. This implies that it is better to prepare a third-overtone resonator with a sub-electrode thicker than the main electrode. However, as there exists technical difficulty in preparing sub-electrodes thicker than the main electrodes (by Hong Kong X'tals), third-overtone resonators with main electrode and sub-electrodes of the same thickness have been fabricated and evaluated in the following section.

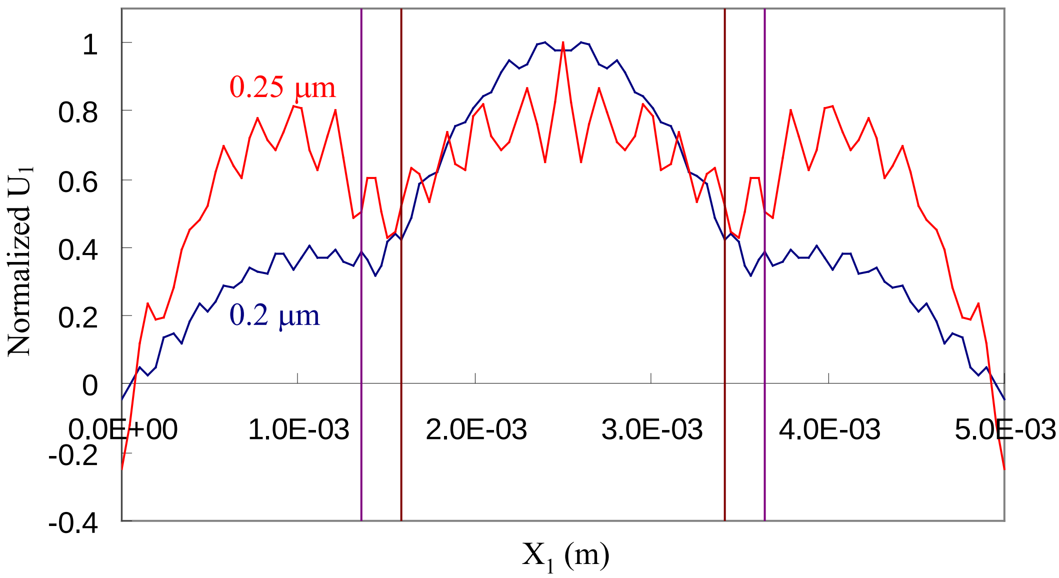

Figure 3.16 The simulated vibration displacements U_1 at the fundamental thickness-shear mode resonance at the top surface of the AT-cut quartz plate (along the scanned line) with sub-electrodes of different thickness. The two vertical brown lines at X_1 = 1.585 mm and X_1 = 3.415 mm indicate the position of the main electrode, while the two vertical purple lines at X_1 = 1.355 mm and X_1 = 3.645 mm indicate the position of the sub-electrodes of length 1.355 mm.

3.3 Fabrication and Characterization of Third-overtone Resonators

On the basis of the simulation results shown in 3.2, third-overtone resonators have been fabricated by Hong Kong X'tals Ltd. The configurations of the quartz plate, main electrode and sub-electrodes are the same as those used for the simulations (refer to Fig. 3.17), and their dimensions are summarized as follows:

	Length (mm)	Width (mm)	Thickness (mm)
Quartz plate	5	2.51	0.085
Main electrode	1.83	1.83	0.0002
Sub-electrode	1.355	2.51	0.0002

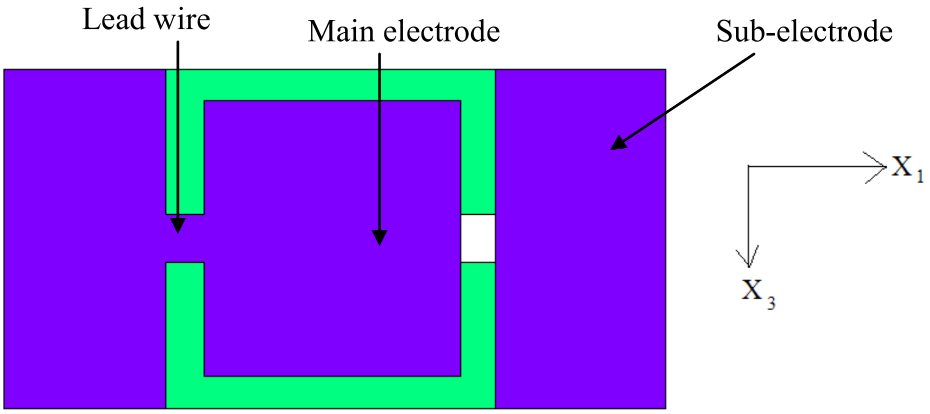

(a)

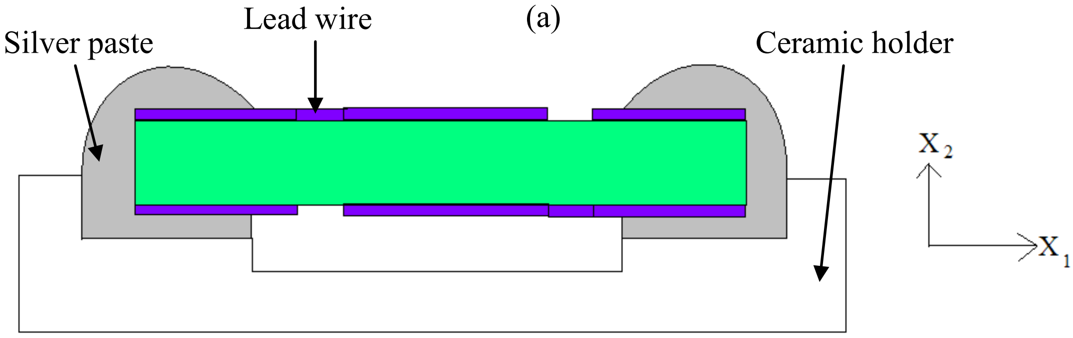

(b)

Figure 3.17 (a) A lead wire connects the main electrode and sub-electrode on each side. (b) The quartz plate placed on a ceramic holder and fixed with silver paste.

For the purpose of applying an electric field or potential to the main electrode through the sub-electrode from the peripheral electronics, a lead wire is introduced to connect the main electrode and sub-electrode on each side as shown in Figure 3.17a. The quartz plate is then placed on a ceramic holder and fixed with silver paste as shown in Figure 3.17b. To simulate the commercial resonator, the end of the quartz plate is embedded in silver paste. For the ease of positioning the quartz plate without disturbing the vibration in the main-electroded region, only about two-third of the sub-electroded region of the quartz plate is embedded by silver paste and supported by the ceramic holder as shown in Figure 3.17b. The impedance spectrum of the resonator is then measured through a pair of test pins applied on the silver paste using a network analyzer (HP E5100A). Figures 3.18a and 3.19a show the observed impedance spectrum of the resonator near the fundamental and third-overtone thickness-shear mode resonances, respectively. In the figures, the observed impedance spectrum for the resonator without silver paste is also plotted for comparison and showing the effects of the silver paste. For comparison, the corresponding simulated impedance spectrum of the resonator with and without silver epoxy near the fundamental and third-overtone thickness-shear mode resonances are shown in Figures 3.18b and 3.19b, respectively. It should be noted that a softer and lossy silver epoxy, instead of silver paste, will be used for the commercial resonators.

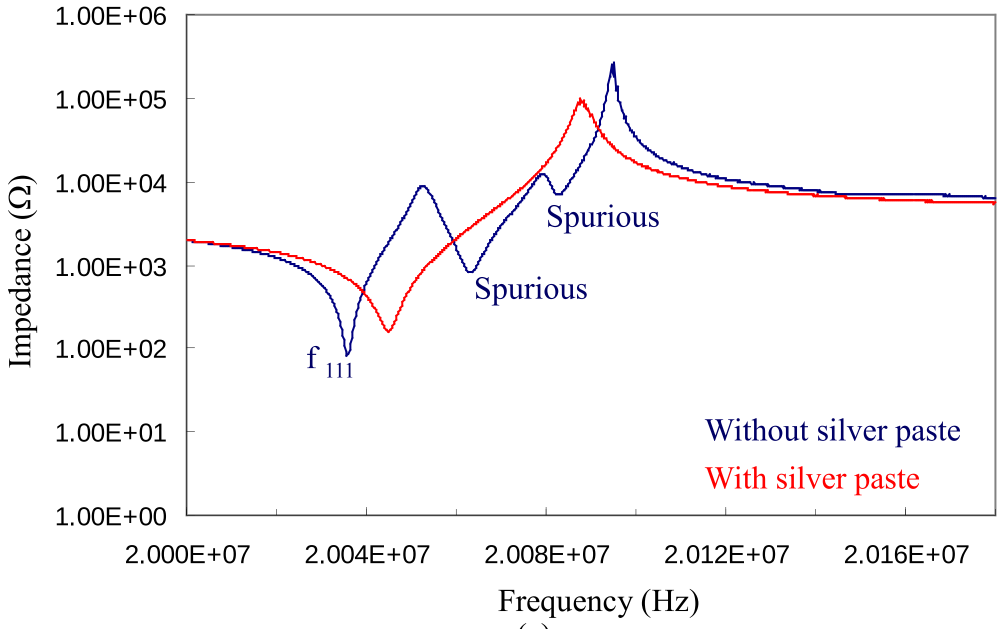

(a)

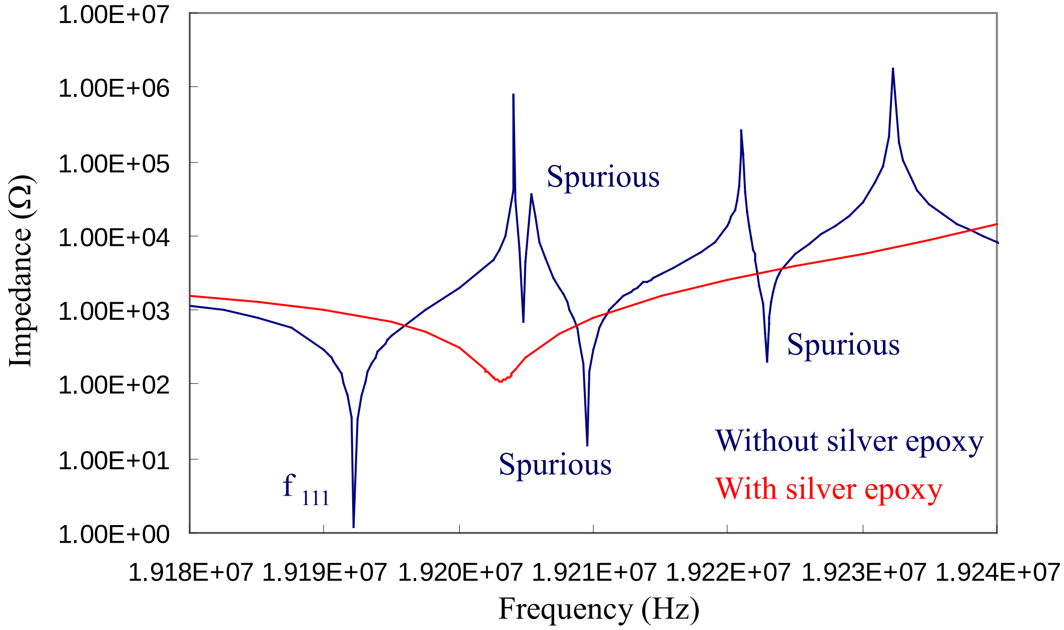

(b)

Figure 3.18 (a) The observed impedance spectrum near the fundamental thickness-shear mode resonances for the resonator with and without silver paste. (b) The simulated impedance spectrum near the fundamental thickness-shear mode resonances for the resonator with and without silver epoxy.

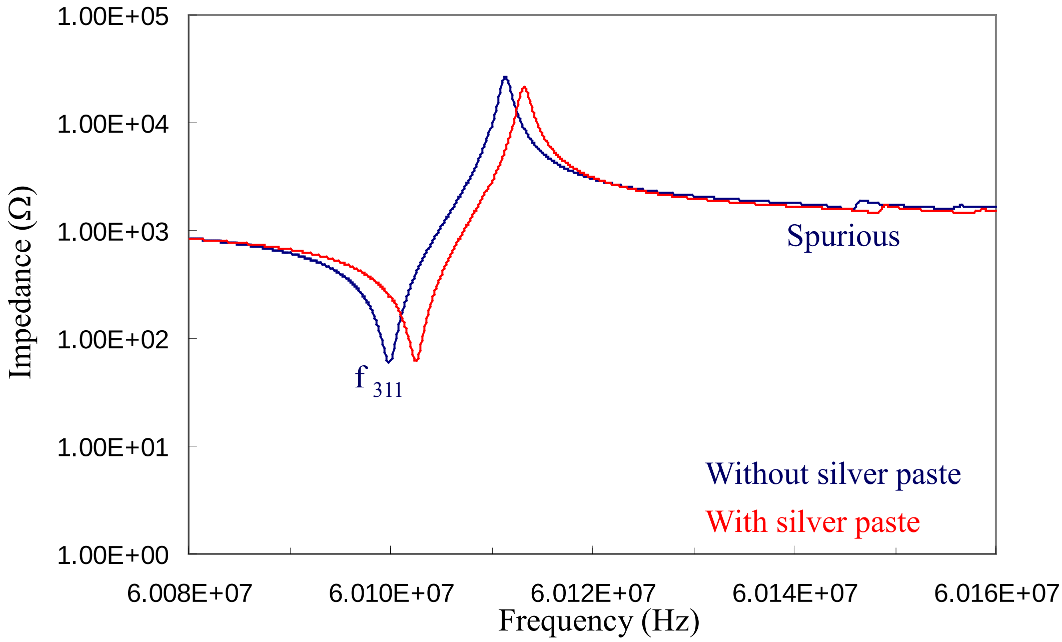

(a)

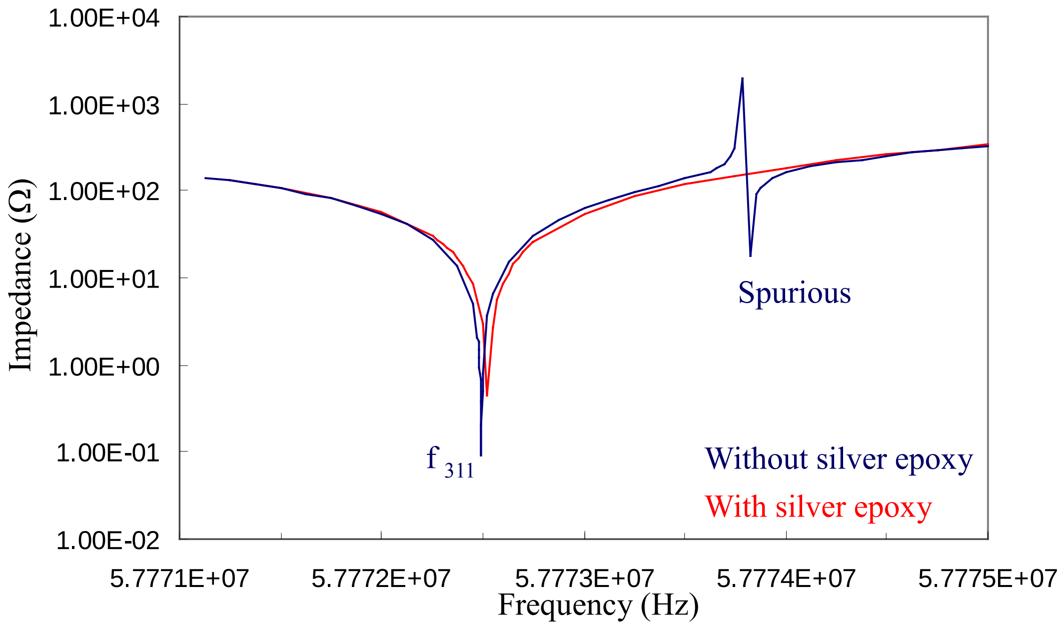

(b)

Figure 3.19 (a) The observed impedance spectrum near the third-overtone thickness-shear mode resonances for the resonator with and without silver paste. (b) The simulated impedance spectrum near the third-overtone thickness-shear mode resonances for the resonator with and without silver epoxy.

The observed fundamental and third-overtone thickness-shear mode resonance (around 20 and 60 MHz, respectively, as shown in Figs. 3.18a and 3.19a) are higher than that for the simulated one (around 19 and 58 MHz, respectively, as shown in Figs. 3.18b and 3.19b) since the quartz plate thickness (which determines the fundamental and third-overtone thickness-shear mode resonance) cannot be precisely controlled in manufacturing process. Apart from this, the general features of the observed impedance spectrum near both the fundamental and third-overtone thickness-shear mode resonance agree well with the simulations. For the resonator without silver paste, there exist spurious modes in the vicinity of the fundamental thickness-shear mode resonance. After the use of silver paste, the spurious mode are suppressed (or shifted to higher frequencies) and the impedance at the fundamental thickness-shear mode resonance frequency increases from about 80 Ω to about 160 Ω. As discussed in the simulations, this should be caused by the energy absorption of the "leaked" vibration in the sub-electroded region. On the other hand, it can be seen that there is almost no effect of the use of silver paste on the third-overtone resonance. The impedance at resonance frequency remains at a small value of about 60 Ω. This implies that the corresponding vibration is effectively trapped in the main-electroded region and hence its energy is not absorbed by the silver paste deposited on the sub-electrodes.

Although the impedance at the fundamental thickness-shear mode resonance frequency is higher than that at the third-overtone resonance frequency (160 Ω vs 60 Ω), the difference may not be large enough to ensure the resonator to resonate at its third-overtone resonance frequency, i.e. the suppression of the fundamental mode resonance is not enough. This may be due to the insufficient energy absorption by the silver paste. For the commercial resonators, a softer and lossy silver epoxy is usually used to fix the quartz plate; hence the energy absorption for the fundamental thickness-shear mode vibration will increase, leading to a better suppression of the fundamental mode resonance. On the other hand, as predicted by the simulations, the fundamental-mode vibration can be amplified more by a thicker sub-electrode and hence effectively suppressed by the silver paste or silver epoxy deposited in the sub-electroded regions.

Chapter Four

Conclusions

The main objectives of the present work are to study the energy trapping phenomenon, and to design and fabricate the third-overtone thickness-shear resonators using the energy trapping technique. The resonance responses of two types of AT-cut quartz resonators, 4-MHz and 27-MHz (provided by Hong Kong X'tals Ltd.), have been carried out by performing simulation studies using the commercial finite element (FEM) code ANSYS. For the 4-MHz resonator with full electrode, there exist spurious modes (thickness-twist mode, flexural mode, and inharmonic thickness-shear mode) in the vicinity (± 0.2 MHz, the frequency range practically used to examine spurious modes in the industry) of the fundamental thickness-shear mode resonance. After the use of an electrode of size smaller than the quartz plate (which is the typical technique for energy trapping), the spurious modes are not suppressed or shift to higher frequencies, and still affect significantly the vibration at the resonance frequency of the fundamental thickness-shear mode (f_{111}).

The simulations also show that the vibration at f_{111} is not effectively trapped in the electroded region and it is spread over the whole quartz plate, leading to a weak dependence of the resonance frequency on the electrode length. It is suggested that the poor energy trapping efficiency for the 4-MHz resonators should be due to the small difference between the cutoff frequencies in the electroded and unelectroded regions as well as the low frequency of the vibration (i.e. the long wavelength as compared to the dimension of the unelectroded region). Due to the mass loading effect, a thicker electrode (e.g. 2 μm) can decrease the cutoff frequency in the electroded region (i.e. f_{111}) and hence improve the energy trapping efficiency. However, a thick electrode is not desirable for the manufacturing process owing to the technical difficulty as well as the high product cost.

If silver epoxy is introduced at the ends of the quartz plate, the simulations show that the energy of the vibration which is not effectively trapped in the electroded region will be absorbed significantly, and thus leading to an increase in impedance at the fundamental thickness-shear mode resonance. In the commercial resonators, silver epoxy is usually deposited on the quartz plate to fix it on the holder and provide electrical connection to the peripheral electronics.

Similar to the 4-MHz resonators, there exist spurious modes (the flexural mode and the inharmonic thickness-shear mode) in vicinity of the fundamental thickness-shear mode resonance for the 27-MHz resonator with full electrodes. However, all the spurious modes are suppressed or shift to higher frequencies after the use of an electrode of size smaller than the quartz plate. The simulations show that the vibration at f_{111} is pure thickness-shear mode and effectively trapped in the electroded region. As a result, the resonance frequency f_{111} is dependent relatively stronger on the electrode length, and the impedance at f_{111} does not increase significantly after the introduction of the silver epoxy. The better energy trapping efficiency should be due to the high frequency of the vibration.

An experimental method has newly been developed to investigate the vibration distribution of the resonators. The method is based on the fact that an external load can disturb the vibration and hence change the resonance frequency as well as the impedance at resonance of a quartz plate. Good agreements between the observed and simulated vibration distributions are obtained for both the 4-MHz and 27-MHz resonators. Besides confirming the simulation results on the different trapping efficiency, this also illustrates that the finite element analysis is a helpful tool in predicting and understanding the resonance responses of a resonator. The simulation results on the dependence of the resonance frequency on the electrode length have also been confirmed by experiments on the "commercial" resonators with different electrode lengths. Again, good agreements between the experimental and simulation results are obtained for both the 4-MHz and 27-MHz resonators.

Based on the understanding of the resonance responses and the energy trapping phenomenon, a third-overtone thickness-shear resonator with resonance frequency around 58 MHz has been designed and successfully fabricated. In the new design, two sub-electrodes are added right next to each end of the main electrode of the resonator. As the vibration at the resonance frequency of the fundamental thickness-shear mode is relatively loosely trapped in the main-electroded region, the “leaked” vibration is amplified by the sub-electrode and subsequently damped by the silver epoxy at the ends of the resonator. On the other hand, the vibration at the third-overtone thickness-shear mode resonance is mainly trapped in the main-electroded region and hence is not affected significantly by the sub-electrode and the silver epoxy. As a result, the impedance at the resonance frequency of the fundamental thickness-shear mode becomes much larger than that at the resonance frequency of the third-overtone thickness-shear mode. In the other words, the fundamental thickness-shear mode is effectively suppressed and the resonator will resonate at its third-over thickness-shear mode.

Appendix A
Analysis and Simulation Considerations using ANSYS

A.1 Organization of ANSYS program

There are two basic levels in the ANSYS program as shown in Figure A.1: Begin level and Processor level. The Begin level is a gateway into and out of ANSYS and platform to utilize some global controls such as changing the name of the files. From the Begin level, one of the ANSYS processors (preprocessor, solution, postprocessor, etc.) is readily accessible in the Processor level. The processor is a collection of functions and routines used to conduct the finite element analysis.

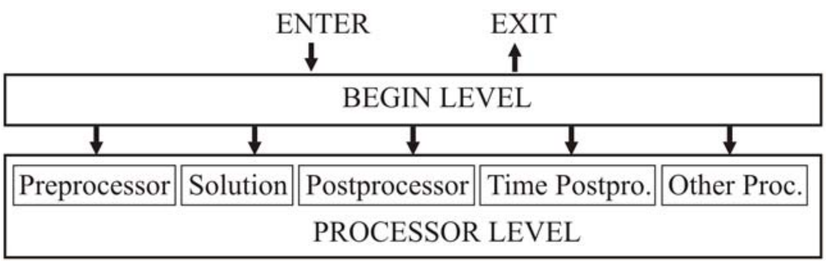

Figure A.1 Schematic of ANSYS levels [*Madenci, 2006*].

There are three main steps in ANSYS analysis: model generation, solution, and reviewing results. Each of these steps corresponds to a specific processor or processors within the Processor level in ANSYS. In particular, the model generation is done in the preprocessor and application of loads and the solution is performed in the solution processor. Finally, the results are viewed in the general postprocessor and the time-history postprocessor.

The most commonly used processors are the preprocessor, the solution processor, the general postprocessor, and the time-history postprocessor.

The preprocessor PREP7 is used for the model generation, which involves material definition, creation of a solid model, and finally, meshing. Important tasks within this processor are specification of the element type, defining the real constants (such as constant electrode thickness), defining the material properties, creation of the model geometry, and generation of the mesh. Although the boundary conditions can be defined in this processor, it is usually done in the solution processor.

The solution processor is used for obtaining the solution for the finite element model that is generated within the preprocessor. It allows you to apply the boundary conditions and loads. For example, for structural problems, displacement boundary conditions and forces can be defined, or for piezoelectric problems, electric potential can be applied. Important tasks within this processor are defining analysis type and analysis options, specification of the boundary conditions, and obtaining solution.

The general postprocessor POST1 is used for reviewing the results at a specific time (or frequency in harmonic analysis) over the entire or a portion of the model. The results can be presented as contour plots, vector displays, deformed shapes, and listings of the results in tabular format.

The results can be reviewed in another way in the time-history postprocessor POST26. This processor is used to review results at specific points in time (or, frequency in the harmonic analysis). Similar to the general postprocessor, it provides graphical variations and tabular listings of results data as function of time (or frequency). It is important to remember that the two postprocessors are just tools for reviewing the results, it is the responsibility of the users to judge the results.

There are several other processors within ANSYS, these mostly concern optimization- and probabilistic-type problems. But these processors are not as commonly used as those described previously.

A.2 Steps of Analysis

To carry out the FEA using ANSYS, the solution domain, the material properties, the physical model, and the loading conditions have to be defined. In the previous section, it is known that there are three main steps in the typical ANSYS analysis: model generation, solution, and reviewing results. Actually, there are six steps in the typical ANSYS analysis. They are:

(1) Defining the Element Type

(2) Defining the Material Properties

(3) Geometry Creation

(4) Mesh Generation

(5) Applying Loads and Obtaining Solution

(6) Reviewing the Results

Each of these steps corresponds to the specific processor. Steps 1 to 4 are performed in the preprocessor. Step 5 is performed in the solution processor. Finally, step 6 is done in the postprocessor. The details of the ANSYS analysis are described below.

(1) Defining the Element Type

The element type must be defined at the beginning of the FEA using ANSYS since it determines two things. First, the element type determines the degree-of-freedom set (which in turn implies the discipline - structural, thermal, magnetic, electric, piezoelectric, quadrilateral, brick, solid, etc.). Second, it determines whether the element lies in 2-D or 3-D space.

In the present work, the 3D coupled-field 20-nodes brick SOLID-226 is used. With the options in the SOLID-226, there are only structural, electrical, and piezoelectric capabilities. The element has twenty nodes with up to four degrees of freedom (displacements in the X-, Y-, Z- directions and electric potential) per node. The geometry of the SOLID-226 is shown in Figure A.2.

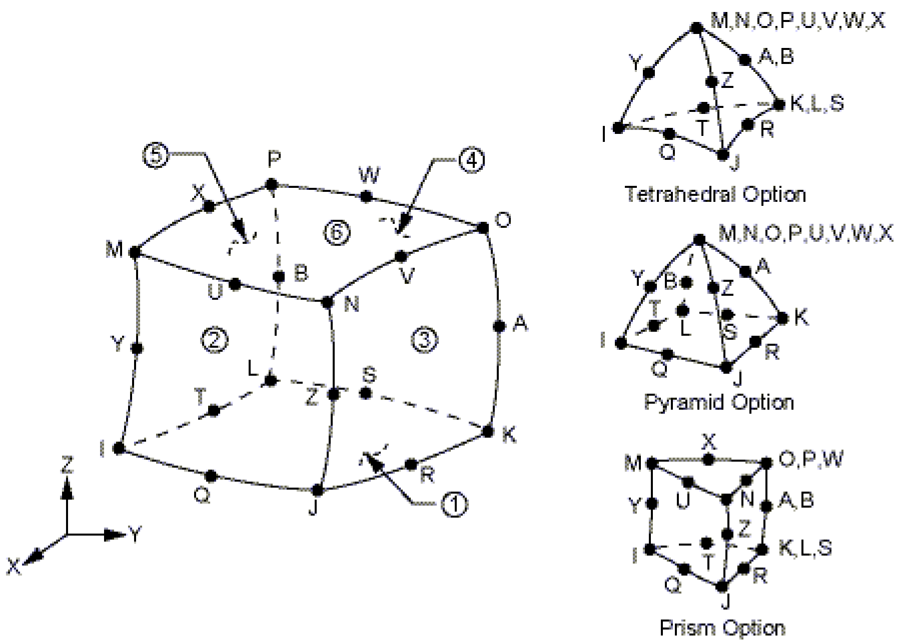

Figure A.2 SOLID-226 geometry. The nodes are represented by the black dots [*ANSYS*].

(2) Defining the Material Properties

After defining the element type, material properties of various parts of the model should be defined in ANSYS. The necessary material properties include electrical, mechanical, and piezoelectric properties.

The material properties for the AT-cut quartz crystal are mass density, elastic stiffness matrix at constant electric field, piezoelectric stress matrix, and relative permittivity matrix at constant strain. The material properties for the silver electrode are mass density, Young's modulus, and Poisson's ratio. The material properties for the silver epoxy are mass density, Young's modulus, Poisson's ratio, and damping factor (no unit).

SI units are used for the material properties and dimensions of the models throughout the simulations.

(3) Geometry Creation

The geometrical representation of the physical system is referred to as the solid model. In the model generation with ANSYS, the ultimate goal is to create a finite element mesh of the physical system. There are two approaches for creating a finite element model: solid modelling and direct generation.

The solid modelling involves the creation of geometrical entities, such as lines, areas, or volumes, that represent the actual geometry of the problem. Once completed, they can be meshed by ANSYS automatically (user still has control over the meshing through user-defined preferences for mesh density, etc.). The solid modelling is the most commonly used approach because it is much more versatile and powerful. However, the user must have a strong understanding of the concepts of meshing in order to utilize the solid modelling approach successfully and efficiently.

In the direct generation, every single node is generated by entering their coordinates followed by generation of the elements through the connectivity information. It requires the user to keep track of the node and element numbering, which may become tedious - sometimes practically impossible - for complex problems requiring thousands of nodes and elements. It is, however, extremely useful for simple problems as one has full control over the model.

In the solid modelling, the solid model can be created by using either entities or primitives. The entities refer to the keypoints, lines, areas, and volumes. The primitives are predefined geometrical shapes.

There is an ascending hierarchy among the entities from the keypoints to the volumes. Each entity (except keypoints, which are the vertices of the solid models and are the lowest-order entity) can be created by using the lower ones. When defined, each entity is automatically associated with its lower entities. If these entities are created by starting with the keypoints and moving up, the approach is referred to as "bottom-up" solid modelling.

When primitives are used, lower-order entities (keypoints, lines, and areas) are automatically generated by ANSYS. As the use of primitives involves the generation of entities without having to create lower entities, it is referred to as the "top-down" approach. Boolean or similar operations can be applied to the primitives to generate the complex geometries.

The bottom-up and top-down approaches can be easily combined since one may be more convenient at a certain stage and the other at another stage. It is not necessary to declare a preference between the two approaches throughout the analysis.

In this project, the "top-down" solid modelling is used for the generation of the solid models. Several different blocks are generated, then they are added or glued together using the Boolean operations. The Boolean operations utilize a set of logical operators such as add, glue, etc. to generate the complex solid models using simple entities.

In the adding operation, the areas (or volumes) must have either a common boundary or an overlapping region. The original areas or volumes that are added will be deleted unless otherwise enforced by the user. The addition of areas or volumes results in a single (possibly complex geometry) entity, as shown in Figure A.3. The adding operation is used in this work to add several blocks to form a single solid model representing a piece of quartz.

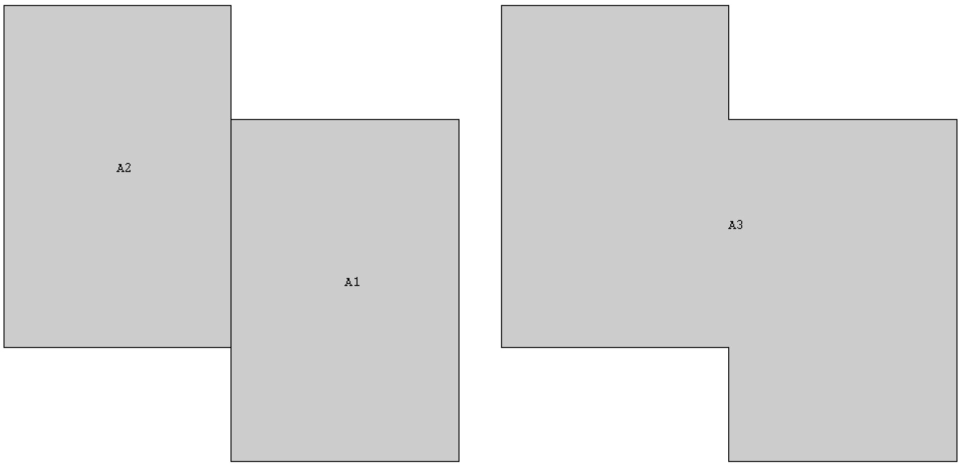

(a) (b)

Figure A.3 (a) Two areas with a common boundary. (b) Two areas added to produce one area. [*Madenci, 2006*]

Another Boolean operation employed is the gluing operation. The gluing operation is used for connecting entities that are "touching" but not sharing any entities. If the entities are apart from or overlapping each other, the gluing operation cannot be used. The gluing operation does not produce additional entities of the same dimensionality but does create new entities that have one lower dimensionality. The entities maintain their individuality, but they become connected at their intersection, as shown in Figure A.4. The gluing operation is used in this work to glue the silver electrode to the quartz plate.

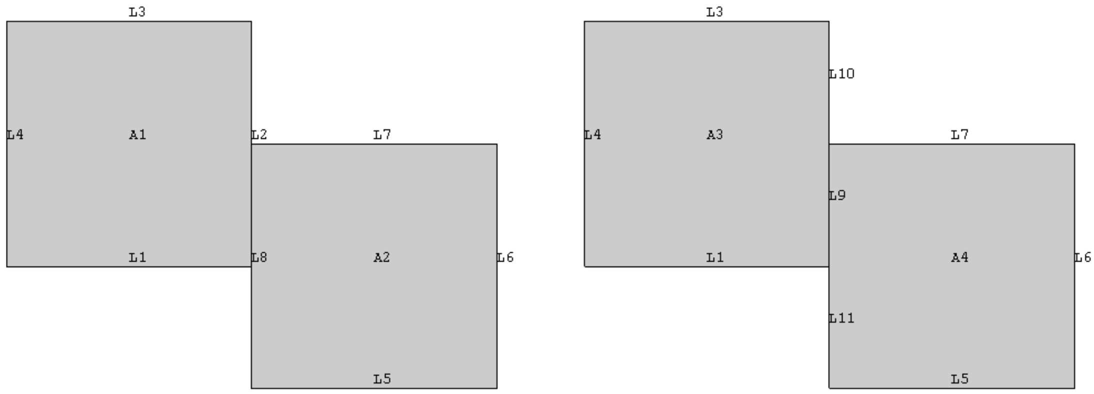

Figure A.4 Two areas with a common boundary plotted with line numbers (left); they do not share any lines as area 1 (A1) is defined by lines 1 through 4 and area 2 (A2) is defined by lines 5 through 8. After gluing (right), the areas share line 9. [*Madenci, 2006*]

(4) Mesh Generation

The ultimate objective in building the solid model is to mesh the model with nodes and elements. Once the solid model is completed, element attributes (the element types and the material properties) are set, and meshing controls are established, then the finite element mesh can be generated automatically in ANSYS. In ANSYS, several options are available in the type of meshing, they are Free Meshing, Mapped Meshing, and Volume Sweeping. The Volume Sweeping is used in this project to generate the finite element mesh. A brief introduction is given for the Free Meshing and the Mapped Meshing first.

In the Free Meshing, no restrictions have been given in terms of element shapes and pattern. Thus, any model geometry, even if it is irregular, can be meshed. The element shapes used will depend on whether you are meshing areas or volumes. For the area meshing, the free mesh can consist of only quadrilateral elements, only triangular elements, or a mixture of the two. For the volume meshing, the free mesh is usually restricted to tetrahedral elements. Pyramid-shaped elements may also be introduced into the tetrahedral mesh for transitioning purposes.

Compared to the Free Meshing, the Mapped Meshing is restricted in terms of the element shape it contains and the pattern of the mesh. The mapped area must be bounded by three or four lines and the mapped area mesh contains either only quadrilateral or only triangular elements, while the mapped volume must be bounded by six areas and the mapped volume mesh contains only hexahedral (brick) elements. In addition, the mapped mesh typically has a regular pattern, with obvious rows of elements. To be able to use this type of mesh, the geometry must be built as a series of fairly regular volumes and/or areas that can accept the mapped mesh. The Free and Mapped meshes are shown in Figure A.5.

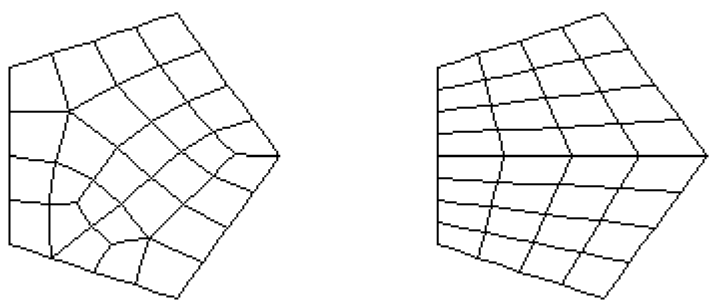

Figure A.5 Free (left) and Mapped (right) meshes [*ANSYS*].

In the case of Volume Sweeping, an existing unmeshed volume can be filled with elements by sweeping the mesh from a bounding area (called the "source area") throughout the volume as shown in Figure A.6.

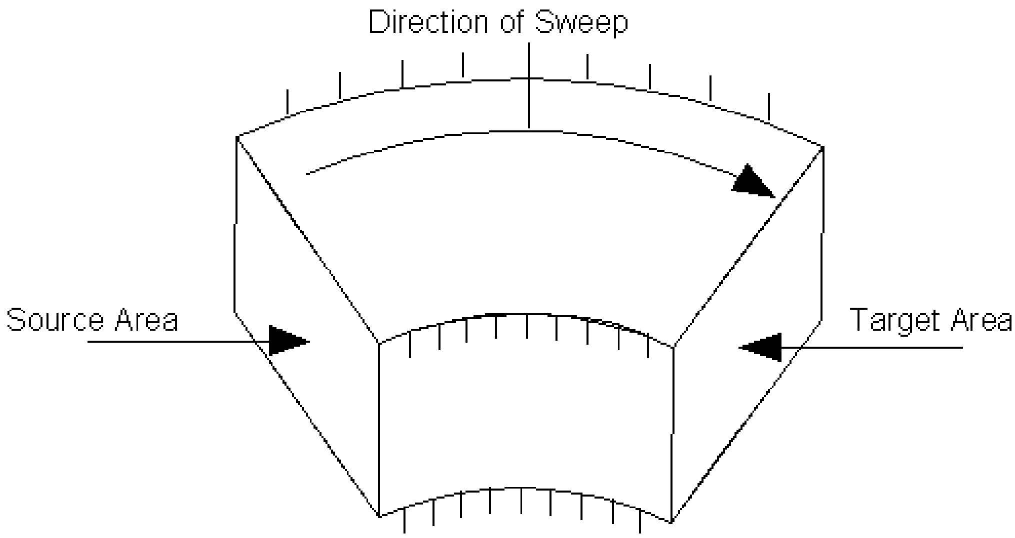

Figure A.6 The Volume Sweeping [*ANSYS*].

If the source area mesh consists of quadrilateral elements, the volume is filled with hexahedral elements. If the area consists of triangles, the volume is filled with wedges. If the area consists of a combination of quadrilateral and triangular elements, the volume is filled with a combination of hexahedral and wedge elements. The swept mesh is fully associated with the volume.

Only this Volume Sweeping and the Free Meshing is applicable to mesh the solid models in this project, and only the Volume Sweeping is applicable to obtain the hexahedral meshes. It is because the quartz plates of the solid models (the quartz plate with a pair of electrodes on the top and bottom of the quartz plate) are bounded by eight areas, one of the solid models is shown in Figure A.7. However, the Mapped Meshing requires the models to be bounded by six areas, thus, making it unsuitable for filling the solid models with the mapped hexahedral meshes. To create the hexahedral meshes for the solid models, the models only have to be broken up into a series of discrete sweepable regions. Thus, the quartz plate is formed by adding several sweepable blocks using the Boolean adding operation. Then, the pair of electrodes is glued to the top and bottom of the quartz plate using the Boolean gluing operation. Then, the solid models can be filled with the hexahedral meshes using the Volume Sweeping.

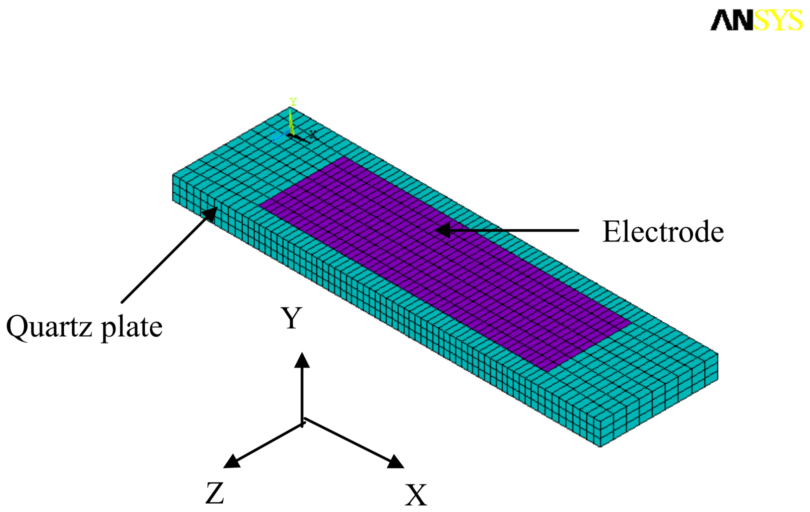

Figure A.7 One of the quartz resonators in this project.

(5) Applying Loads and Obtaining Solution

After preprocessing, the model generation, including the meshing, is complete. The next step is to begin the solution phase of the ANSYS session. In the solution processor, the analysis type and analysis options are defined, loads are applied, load step options are specified, and the finite element solution are initiated.

The word "loads" as used in ANSYS documentation includes boundary conditions (constraints, supports, or boundary field specifications) as well as other externally and internally applied loads. The loads can be applied either to the solid model (keypoints, lines, and areas) or the finite element model (nodes and elements). In this project, the applied loads are electric potential which applied to the nodes of the electrodes as shown in Figure A.7.

The analysis type is chosen based on the loading conditions and the response calculated. In the present work, the electrical impedance and the vibration mode shapes of the quartz resonators are to be calculated with the sinusoidally (harmonically) varying electric potentials as the applied loads, and thus, a harmonic analysis is chosen. Not all analysis types are valid for all disciplines. For the piezoelectric analysis, only static, modal, harmonic and transient analysis can be used.

To specify the harmonic electric potential, three pieces of information are usually required: the amplitude, the phase angle, and the forcing frequency range. The amplitude is the maximum value of the electric potential, which is 0.5 V in the present work. The phase angle is a measure of the time by which the electric potential lags (or leads) a frame of reference. On the complex plane, it is the angle measured from the real axis. The phase angle is required only if multiple electric potentials that are out of phase with each other are applied. In the present work, only a single electric potential is applied, and thus, the phase angle is not required. The forcing frequency range is the frequency range of the harmonic electric potential (in Hz). Moreover, substep is required to be specified since it is used to obtain solutions at several frequencies within the forcing frequency range which is evenly spaced. After specifying the loading condition and defining the analysis type, the finite element solution can be initiated.

(6) Reviewing the Results

Once the solution has been calculated, the results can be reviewed using the ANSYS postprocessors: POST1, the general postprocessor, and POST26, the time-history postprocessor.

The POST1 is used to review the results over the entire model at specific frequencies. Available options for the review include the plotting of contours, vector displays, deformed shapes, and listings of the results in tabular format. The contour plot of the vibration displacement at resonance is shown in Figure A.8.

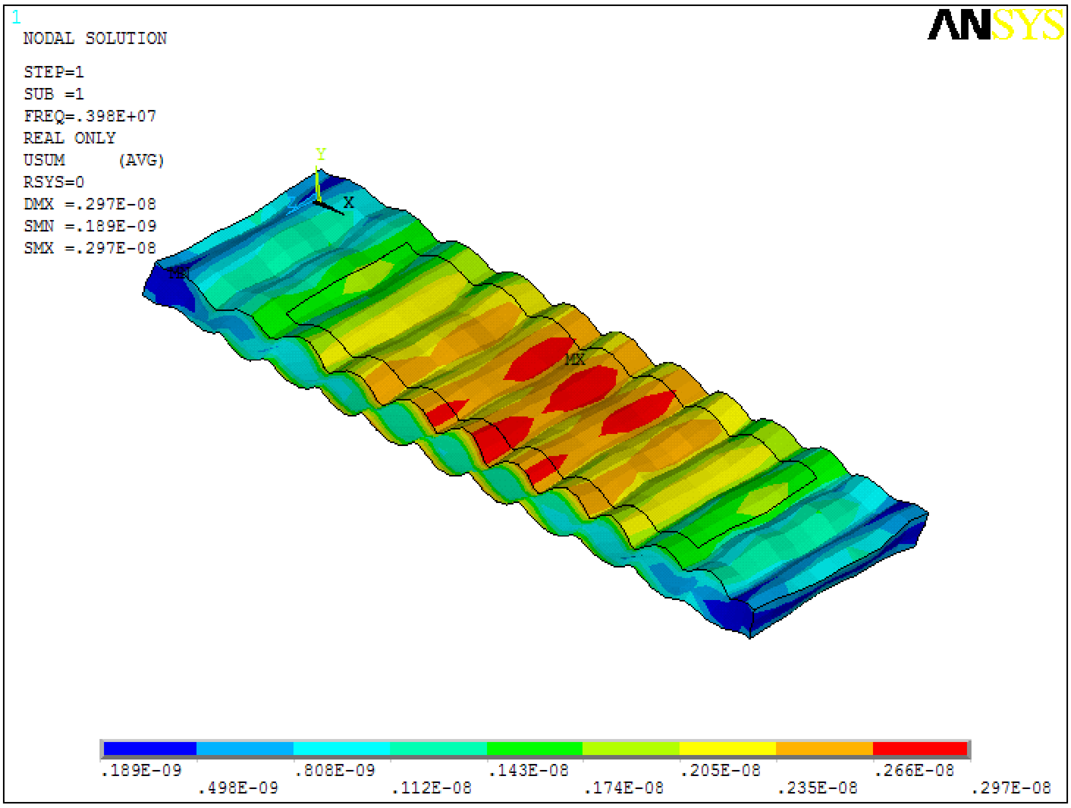

Figure A.8 Contour plot of the vibration displacement at resonance.

The results can be reviewed in another way in the POST26. The POST26 is used to review the results at specific points in the model with respect to frequency. Similar to the POST1, it provides graphical variations and tabular listings of results data as function of frequency. The impedance spectrum as shown in Figure A.9 is obtained using the POST26.

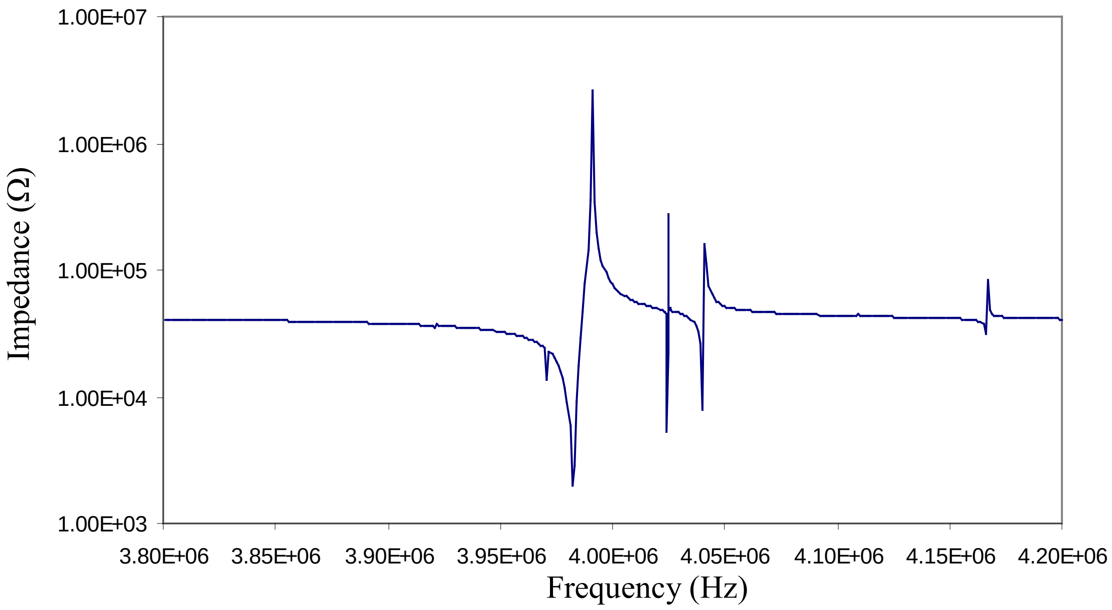

Figure A.9 Impedance spectrum obtained using POST26.

A.3 Simulation Considerations

A.3.1 Mesh density

In the mesh generation, the complex model is divided into a number of finite elements that become solvable in an otherwise too complex situation. This is one of the most crucial steps in determining the solution accuracy of the problem. Generally, a large number of elements provide a better approximation of the solution. However, in some cases, an excessive number of elements may increase the round-off error. Therefore, it is important that the mesh is adequately fine or coarse in the appropriate regions. The fineness or coarseness of the mesh in such regions varies from cases to cases. However, there is a technique that might be helpful in answering these questions.

The technique is mesh refinement test within ANSYS. An analysis with an initial mesh is performed first and then reanalyzed by using twice as many elements. The two solutions are compared. If the results are close to each other, the initial mesh configuration is considered to be adequate. If there are substantial differences between the two, the analysis should continue with a more-refined mesh and a subsequent comparison until the results are close to each other.

A.3.2 Number of elements along the thickness

The number of elements along the thickness of the quartz plate is dependent on the order of the harmonic of the modes concerned. For instance, when the mode is the fundamental thickness-shear mode, there is one half wavelength along the thickness of the model. At least five points are required to represent the one half wavelength as shown in Figure A.10. As a result, at least two elements of five nodes along the thickness direction for the SOLID-226 element are needed. Here, three elements of seven nodes are used for the better representation of the half wavelength.

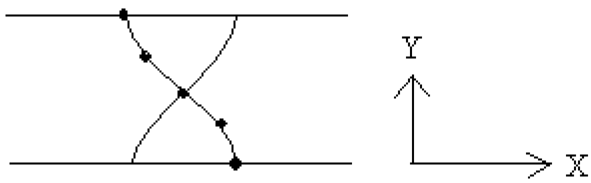

Figure A.10 Five points are required to represent the one half wavelength.

References

Adams, V., *Building better products with finite element analysis*, OnWord Press, Santa Fe, N.M., (1999)

Allik, H., Hughes, J. R., *Finite element for piezoelectric vibration*, International Journal for Numerical Methods in Engineering, Vol. 2, No. 2, pp. 151-157 (1970)

ANSYS, *ANSYS 9.0 documentation*

ANSI/IEEE Std 100-1984, IEEE standard dictionary of electrical and electronics terms, (1984)

Bahadur, H., Parshad, R., *Acoustic vibrational modes in quartz crystals: their frequency, amplitude, and shape determination*, Physical Acoustics, Vol. 16, pp. 37-171, Academic Press (1982)

Ballato, A., *Doubly rotated thickness mode plate vibrators*, Physical Acoustics, Vol. 13, pp. 115-181, Academic Press (1977)

Bechmann, R., *Piezoelectric plate*, United States Patent 2249933 (1941)

Bottom, V. E., *Introduction to quartz crystal unit design*, Van Nostrand Reinhold, New York, (1982)

Chandrupatla, T. R., *Introduction to finite elements in engineering*, Prentice Hall, Upper Saddle River, N.J., (1997)

Cook, R. D., *Finite element modeling for stress analysis*, John Wiley and Sons, Inc., New York, (1994)

Cumpson, P. J., Seah, M. P., *Quartz crystal microbalance; radial/polar dependence of mass sensitivity both on and off the electrodes*, Measurement Science and Technology, Vol. 1, No. 7, pp. 544-555 (1990)

Curran, D .R., Koneval, D .J., *Factors in the design of VHF filter crystals*, Proceedings of 19th Annual Frequency Control Symposium, pp. 213-268 (1965)

Felippa, C., *Introduction to finite element methods websites (http://www.colorado.edu/engineering/CAS/courses.d/IFEM.d/Home.html)*, Department of Aerospace Engineering Sciences, University of Colorado at Boulder, (2006)

Frondel, C., *The system of mineralogy*, Vol. 3, “Silica Minerals”, John Wiley and Sons, Inc., New York, (1962) Guttwein, G. K., *Status of quartz crystal research and development*, Proceedings of 17th Annual Frequency Control Symposium, pp. 190-214 (1963)

Heising, R. A., *Quartz crystals for electrical cicuits - their design and manufacture*, Van Nostrand Reinhold, New York, (1946)

Hirama, K., Aoyama, Y., *Energy trapping behavior of AT-cut quartz crystal resonators with a groove ring on main electrodes*, Electronic Communications in Japan, Part 3, Vol. 82, No. 4, pp. 48-55 (1999)

Hirama, K., Shoji, T., Tanaka, Y., *Suppression of lower harmonic responses on overtone AT-cut quartz crystal resonators*, Electronics and Communications in Japan, Part 3, Vol. 83, No. 4, pp. 92-102 (2000)

Ikeda, T., *Fundamentals of piezoelectricity*, Oxford University Press, New York, (1990)

Iwata, H., Hirama, K., *Suppression of inharmonic modes using elliptical periphery electrodes in very high frequency fundamental AT-cut resonators*, Japanese Journal of Applied Physics, Vol. 40, pp. 3668-3671 (2001)

Madenci, E., The finite element method and applications in engineering using ANSYS, Springer, New York, N.Y., (2006) Mindlin, R. D., Gazis, D. C., *Strong resonances of rectangular AT-cut quartz plates*, Proceedings of 4th US National Congress of Applied Mechanics, pp. 305-310 (1962)

Mortley, W. S., *A waveguide theory of piezoelectric resonance,* Marconic Review, Vol. RD756 (1946)

Mortley, W. S., *Frequency-modulated quartz oscillators for broadcasting equipment*, Proceedings of the IEEE, Vol. 104B, No. 12, pp. 239-249 (1956)

Nakamura, K., Yasuike, R., Hirama, K., Shimizu, H., *Trapped-energy piezoelectric resonators with elliptical ring electrodes*, Proceedings of 44th Annual Frequency Control Symposium, pp. 372-377 (1990)

Onoe, M., Jumonji, H., *Analysis of piezoelectric resonators vibrating in trapped energy modes*, Electronics and Communications in Japan, Vol. 48, No. 9, pp. 84-93 (1965)

Onoe, M., *Effect of energy trapping on performance of QCM*, Proceedings of the 2005 Frequency Control Symposium and Exposition, pp. 433-441 (2005)

Salt, D., *Hy-Q handbook of quartz crystal devices*, Van Nostrand Reinhold, Wokingham, (1987) Shockley, W., Curran, D. R., Koneval, D. J., *Energy-trapping and related studies of multiple electrode filter crystals*, Proceedings of 17th Annual Frequency Control Symposium, pp. 88-126 (1963)

Shockley, W., Curran, D. R., Koneval, D. J., *Trapped-energy modes in quartz filter crystals*, The Journal of the Acoustical Society of America, Vol. 41, No. 4, Part 2, pp. 981-993 (1967)

Spyrakos, C. C., *Finite element modeling in engineering practice : includes examples with ALGOR*, Algor Publishing Division, Pittsburgh, PA, (1996)

Tiersten, H. F., *Linear piezoelectric plate vibrations; elements of the linear theory of piezoelectricity and the vibrations of piezoelectric plates*, Plenum Press, New York, (1969)

Vig, J. R., *Military applications of high accuracy frequency standards and clocks*, IEEE Transactions on Ultrasonics, Ferroelectrics, and Frequency Control, Vol. 40, pp. 522-527 (1993)

Vig. J. R., *Quartz crystal resonators and oscillators for frequency control and timing applications. A tutorial*, (2003)

List of Publications

H.T. Wong, K.W. Kwok and H.L.W. Chan, "Study of PMN-PT Single Crystals for Resonator Applications", *International Frequency Control Symposium*, pp. 559 – 562 (2006).